Detection of Building Damages in High Resolution SAR Images based on SAR Simulation

Zur Erlangung des akademischen Grades eines

DOKTOR-INGENIEURS

von der Fakultät für

Bauingenieur-, Geo- und Umweltwissenschaften

des Karlsruher Instituts für Technologie (KIT)

genehmigte

DISSERTATION

von

Dipl.-Ing. Silvia Kuny

aus Freiburg im Br.

Tag der mündlichen Prüfung: 04.06.2020
Referent: Prof. Dr.-Ing. Stefan Hinz
Korreferent: Prof. Dr.-Ing. Peter Reinartz

Karlsruhe (2021)

Abstract

In the event of natural disasters such as earthquakes striking urban areas a fast emergency response is crucial, procuring a strong demand for fast and reliable methods to detect structural damages. In this regard, remote sensing imagery is a vital source of information able to provide high resolution large-scale data at short notice and practically world-wide. Oftentimes spaceborne synthetic aperture radar imagery is the first available data following such an event, as a result of its independence of weather and illumination conditions. Missions such as TerraSAR-X, COSMO-SkyMed and PAZ can provide high resolution imagery of below 1 m resolution, maintaining good qualifications for the emergency context. With regard to high resolution data, pre-event imagery is generally rare, since only areas specifically at risk are monitored, thus ruling out the possibility to use change detection methods. As a consequence, there is the challenging but likely case of having only a post-event image to work with.

In this thesis a novel method for building damage detection on solely a post-event high resolution SAR image is presented. A main aspect hereby is the generation and use of synthetic SAR signatures as a means to provide for an apt training data set. On these grounds, initial focus is put on a signature analysis of damaged buildings, differentiating between a set of commonly occurring damage types. It is concluded that the textures of heaps of debris pose the most prominent indication for severely damaged buildings. Since suitable training data is sparse, due to the limited number of damaged buildings in existing SAR images, the use of synthetic SAR signatures is investigated. A routine is demonstrated how to obtain a capable synthetic training data set, accounting for factors such as 3d modelling of a heap of debris and the imitation of backscattering properties typically found in debris. By simulating a large variation of different debris characteristics a realistic texture variation is established.

The algorithm for damage detection introduces a sequence of processing steps. The pre-processing involves a radiometric scaling in order to attain transferability to other imagery and a dynamic scaling to account for the SAR specific grey level distribution. A set of texture features, consisting of Haralick features and statistics of the first order, prove to be suitable for differentiating between debris and similar texture. The core processing involves two steps: firstly a screening step that localises areas of debris-like texture based on feature intervals that are learned from the texture variety of artificial debris signatures; and secondly a random forest based classification aiming at separating debris from the identified sources of similar texture, high vegetation and gravel. A series of post-processing steps transfers the pixel-wise results to a component-wise detection map.

After verifying the viability of using simulated texture, the performance of the new approach is demonstrated on a high resolution Spotlight TerraSAR-X image of post-earthquake Christchurch, New Zealand. The debris detection results are evaluated by means of an aerial optical image and a manually extracted reference debris map.

Kurzfassung

Wenn es in urbanen Gebieten zu einer Naturkatastrophe wie zum Beispiel einem Erdbeben kommt, ist eine schnelle Krisenreaktion (Notfallmaßnahmen) von äußerster Wichtigkeit. Hieraus entsteht ein hoher Bedarf an schnellen und zuverlässigen Methoden zur Detektion struktureller Schäden. In diesem Zusammenhang stellen Fernerkundungsdaten eine entscheidene Informationsquelle dar, da es durch sie ermöglicht wird, zeitnah und praktisch weltweit großflächig hochaufgelöste Daten bereitzustellen. Oftmals sind raumgestützte SAR (Radar mit synthetischer Apertur) Bilder aufgrund ihrer Wetter- und Beleuchtungsunabhängigkeit die ersten erhältlichen Daten nach solch einem Ereignis. Missionen wie zum Beispiel TerraSAR-X, COSMO-SkyMed und PAZ können hochaufgelöste Bilder unter 1 m Auflösung liefern und stellen damit eine gute Voraussetzung für den Notfall dar. Da eine Überwachung überlicherweise nur für Risikogebiete durchgeführt wird, gibt es generell selten hochaufgelöste pre-event Bilder, wodurch der Einsatz von Methoden zur Änderungsanalyse hinfällig wird. Dementsprechend tritt der schwierige aber wahrscheinliche Fall auf, dass lediglich ein postevent Bild zur Verfügung steht.

In dieser Dissertation wird eine neue Methode zur Detektion von Gebäudeschäden auf Basis nur eines hochaufgelösten post-event SAR-Bildes vorgestellt. Ein wesentlicher Aspekt hierbei ist die Generierung und Nutzung synthetischer SAR-Signaturen als ein Mittel um einen geeigneten Trainingsdatensatz zu erhalten. Aus diesem Grund wird zunächst Fokus auf eine Signaturanalyse von Gebäudeschäden gelegt, wobei zwischen einer Reihe häufig auftretender Schadenstypen unterschieden wird. Die Textur von Schutthaufen stellt sich dabei als das markanteste Indiz für schwere Gebäudeschäden heraus. Da es, aufgrund der begrenzten Anzahl beschädigter Gebäude in bestehenden SAR Bildern, nur wenige geeignete Trainingsdaten gibt, wird die Nutzung synthetischer SAR-Signaturen untersucht. Eine Routine zur Erstellung eines geeigneten synthetischen Trainingsdatensatz wird dargelegt, wobei Faktoren wie die 3D-Modellierung von Schutthaufen und die Modellierung schutttypischer Rückstreueigenschaften berücksichtigt werden. Indem eine große Variation an verschiedenen Schuttcharakteristika simuliert wird, ist eine realistische Texturvariation gegeben.

Der Algorithmus zur Schadensdetektion führt eine Abfolge von Prozessierungsschritten ein. Die Präprozessierung beinhaltet eine radiometrische Skalierung, um ein Übertragbarkeit auf andere Bilddaten zu gewährleisten, und eine Skalierung des Dynamikbereichs, um der SAR-spezifischen Grauwertverteilung Rechnung zu tragen. Eine Reihe von Texturmerkmalen erweist sich als geeignet zur Unterscheidung von Schutt und ähnlicher Textur. Diese besteht aus Haralick Merkmalen und Statistiken der ersten Ordnung. Der Kern des Verfahrens umfasst zwei Prozessierungsschritte: erstens ein *Screening*, mit Hilfe dessen Gebiete einer schuttähnlichen Textur lokalisiert werden. Dieser Schritt basiert auf Merkmalsintervallen, die aus der Texturvariation der künstlichen Schuttsignaturen abgeleitet werden. Darauf folgt zweitens eine Random Forest basierte Klassifikation, die darauf abzielt Schutt von den ermittelten Quellen ähnlicher Textur, hohe Vegetation und Schotter, zu trennen. Eine Reihe von Postprozessierungsschritten transformiert die pixelweise vorliegenden Resultate in eine komponentenweise Detektionskarte.

Nach Untersuchungen zur Nutzbarkeit simulierter Texturen, wird die Detektionsleistung des neuen Ansatzes anhand eines hochaufgelösten Spotlight TerraSAR-X Bildes, des von einem Erdbeben schwer getroffen Christchurch, Neuseeland, getestet. Abschließend werden die Schuttdetektionsresultate anhand eines optischen Luftbildes und einer manuell extrahierten Referenzschuttkarte evaluiert.

Contents

Chapter 1.

Introduction

1.1. Motivation

When natural disasters such as earthquakes occur in urban areas and heavy structural damages are entailed, a dire need for fast emergency response arises. The main drive in the course of the first phase of emergency response usually is the coordination of rescue operations with the primary aim to help people still trapped under debris. A fast information gain is most crucial for this. Satellite remote sensing imagery is a vital source of information in this regard, as it provides worldwide high resolution large-scale data. Hence, there already exist many damage detection approaches in this domain, whereas typically and regardless of the sensor that is employed a pre- and a post-event image is used to conduct change detection.

The time essence of emergency response, however, raises the question of image availability at that early stage. Optical imagery, as effective as it can be for the damage detection task, can only be recorded under favourable circumstances, that is to say in day light and with a lack of cloud cover. In view of that, the weather and lighting independence of synthetic aperture radar (SAR) imagery proves to be very useful. Nowadays several active satellite missions can ensure image availability, and that with a resolution down to less than a meter, thus making SAR imagery, in particular high resolution (HR) SAR imagery, well suited for the emergency case and rather likely the first available post-event data in the case of natural disasters.

The possibility of change detection, using both a pre- and a post-event image, is inviting and widely researched since it can be a very efficient tool for damage detection. However, this requires a pre-event image that matches the post-event image in parameters such as frequency, resolution and orientation. A matching pre-event HR SAR image rarely exists in cases of fatal disasters, though, thus disqualifying the prospect of change detection in many cases. This leads to the likely and challenging case of having merely a HR post-event SAR image to work with.

The interpretation of a single SAR image is problematic, since damaged buildings can take many forms. In X-band SAR imagery a very prominent indication for structural damages is the signature caused by heaps of debris surrounding the buildings, their texture differing considerably from that of intact buildings. Focussing on this characteristic allows for a texture based damage detection with neither pre-event image nor any ancillary data. A major issue, though, is the sparse availability of suitable training areas, due to the limited number of damaged buildings in existing SAR images. Further complicating matters, the signatures of damaged buildings are often impaired by neighbouring buildings or objects, due to SAR specific imaging effects (layover). As a consequence, the extraction of debris signatures from real SAR imagery is difficult. For an adequate training data set, however, a large amount of samples is vital. Also, to be able to encompass the full signature range of possible characteristics of damaged buildings or debris, a large spectrum of different kinds of occurrences is of essence. Since this is not achievable in terms of real signatures, using simulated samples as training data is an advantageous perspective. Synthetically generated samples are unaffected by random factors, indefinitely expandable, and independent from the actual SAR image that is to be investigated.

In this thesis, first a signature analysis on building damages is conducted in order to provide information on potential characteristics. Based on these findings, the focus is set on debris as the most prominent textural factor of a damaged building. With the aim of generating a capable training data set, debris signatures are

simulated that firstly need to be accurate enough to be comparable to real signatures and secondly must be diverse enough to encompass the spectrum of potential characteristics. Since the SAR signature of debris is radiometrically complex, the task of simulation poses high demands on the SAR simulator, the 3d modelling and the specification of radiometric backscattering properties. An algorithm is presented that performs damage detection in urban areas on a post-event HR SAR image only, based on the simulated training data set. The performance of the algorithm is demonstrated on a HR Spotlight TerraSAR-X image taken over a post-earthquake urban area. Further, the viability of using simulated texture is investigated.

1.2. State of the Art

In this section an overview is provided regarding recent research developments in the fields of building damage detection and SAR simulation.

1.2.1. Building damage detection using remote sensing data

Remote sensing data, spaceborne and airborne, contribute greatly to the task of building damage assessment, with different sensors providing different advantages. The research effort on damage assessment using optical imagery has been dominant for years, whereas SAR and LiDAR are comparatively new. However, since the motives to use SAR imagery have been declared already, the following summary of research developments deliberately puts focus on approaches using SAR data. Depending on the image availability, damage detection methods can be divided into those detecting changes between pre- and post-event data and those relying solely on post-event data.

Optical and LiDAR data

Typically, optical change detection methods either combine pre- and post-event images using mathematical operations such as subtraction of bands, ratioing, and image regression, or they conduct independent classifications on the two images [20]. Rathje et al. [68] propose a change detection algorithm for damage detection based on pre- and post-event coregistered QuickBird data, using Haralick features [32] to compute a correlation coefficient. Tomowski et al. [77] compare several texture measures [32] for the use of four known change detection methods (image-differencing, image-ratioing, regression analysis and principal component analysis). It is shown that a principal component analysis with the texture feature Energy yields the best results. Gamba et al. [23] use the Normalized Difference Vegetation Index and linear segments to extract buildings for both pre- and post-event image, thus allowing for the detection of building changes. Gerke and Kerle [24] present a classification framework for damage mapping using oblique, multi-perspective aerial data, combining various lines of damage evidence into a classification distinguishing between three levels of damage. Methods such as proposed by Yamazaki et al. [86] use various characteristics such as edges, shapes, or texture to detect damages based on a post-event image only.

Since in a post-earthquake scenario it is not common to have laser scanning data available, there are only few approaches to damage detection using LiDAR data. Rehor [69] proposes a method for the detection and classification of building damages based on post-event laser scanning data. Planar surfaces are extracted and geometrically overlaid with roof planes from pre-event building models, thus providing information about changes in features, such as volume, height, inclination and size. The classification step regarding the assignment of different damage types is realised by a segment-based fuzzy logic approach. Based on a pair of LiDAR data sets (pre- and post-event) and with the help of building footprints, Moya et al. [61] assess three parameters (the average height difference between the two digital surface models (DSMs), the standard deviation, and the correlation coefficient) regarding their efficiency to identify collapsed buildings. It was found that using a threshold on the average height difference obtains the best classification results.

SAR data - Pre- and post-event data

For SAR change detection, both amplitude and phase information can be exploited. On that account, methods can be divided into two main groups: coherent and incoherent approaches. Incoherent change detection uses the backscattering intensity/ amplitude of a scene to quantify changes whereas coherent change detection uses the coherence to identify changes in both amplitude and phase information. Coherent approaches have the potential to detect very subtle changes but, in return, require coherent processing, a capable repeat pass image pair, and most notably, potential changes need to be surrounded by coherent areas.

Incoherent change detection methods, since only utilising amplitude information, usually rely on some sort of ratio image between pre- and post-event image or on some information theoretic measure such as Kullback-Leibler distance or mutual information. Matsuoka and Yamazaki [55] conducted a study on backscattering characteristics in pre- and post-earthquake ERS images, finding that backscattering coefficient and intensity correlation between the two images are measurably lower in damaged areas. Uprety et al. [81] use a similar method to detect building damages at an individual level. Chini et al. [15] detect areas of uplift and subsidence solely by means of SAR backscattering. Guida and Brett [28, 9] propose an approach using the amplitude change of dihedral building corner lines. By means of a ridge detection filter and the ratio image of pre- and post-event image, locations of damaged buildings are identified. Also focussing on the double-bounce return from buildings, Chini et al. [14] use four change detection indicators (intensity ratio, interferometric coherence, intensity correlation and Kullback Leibler divergence) to identify damaged areas. Saha et al. [70] use a CNN (Convolutional Neural Network) based unsupervised method for the detection of destroyed buildings, exploiting sub-optimal deep features extracted from an optically pre-trained CNN. Based on two HR SAR images (pre- and post-event), the deep features are compared pixel-wise to identify changes. Marin et al. [54] introduce a method that extracts information on changes regarding backscattering increase and decrease of destroyed buildings with the aim to grade changes into either new or fully destroyed buildings. Miura et al. [60] seek to detect collapsed buildings in TerraSAR-X Stripmap imagery using prior knowledge of building footprints. They employ a linear discriminant score based on the difference in backscattering coefficient and the intensity correlation between the two SAR images. Tao and Auer [75] propose two change detection methods employing two SAR images (pre- and a post-event) and a DSM. Based on geometric prior knowledge such as layover area, shadow area and wall segments that is derived from the DSM, change detection is conducted on either building or facade level using change ratios.

For coherent change detection the research effort is comparatively small, presumably due to the rather long revisit times of satellite SAR sensors. Yonezawa et al. [87] use a coherent change detection approach to investigate the decrease in interferometric correlation due to building damages. Hoffman [36] presents an approach based on the change of interferometric coherences in pre- and post-event SAR images. A coherence change index is thresholded to classify different damage levels. Arciniegas et al. [4] propose a coherence- and amplitude-based analysis for earthquake damage assessment, finding that the combination of both change maps leads to better results than coherence- or amplitude-based detection individually. Similarly, Milisavljevic et al. [59] present an approach that combines findings about amplitude changes and coherence changes of pre- and post-event SAR imagery. Demonstrated on simulated SAR data, Welte et al. [85] propose an approach to extract main elements of building signatures such as layover, roof, and shadow area from interferometric phase values, thus providing the means for an impending change detection effort.

SAR data -Post-event data only

Since a single SAR image is difficult to interpret, most research approaches for damage detection either rely on sub-meter imagery or on ancillary data. Balz et al. [6] conduct a simulation supported analysis on the appearance of collapsed buildings in high-resolution SAR imagery and propose a workflow for image interpretation. Brunner et al. [12] run an analysis on decimetre resolution SAR data from an experimental airborne

SAR system. Based on the signature of an artificial village with different types of destroyed buildings it is found that the increased resolution allows for a classification of destroyed buildings into several basic damage classes. Based on post-earthquake COSMO-SkyMed data and building block GIS (Geographic Information System) polygons, Polli et al. [66] attempt to estimate the damage grade at city block-level using a set of texture measures. A correlation was established between several measures (i.e. entropy and homogeneity) and the damage grades. In [19] this approach is pursued and quantitative results are presented for a block-level damage classification into three damage grades.

Tao et al. [76] introduce a change detection method regarding an artificial SAR image, generated by simulating a DSM, and a real SAR image. By means of pixel-based methods, changes in areas such as layover and shadow are analysed. Gong et al. [25] employ post-event sub-meter very high resolution SAR imagery (TerraSAR-X staring spotlight) and a prior knowledge building footprint map to determine if buildings are destroyed. A classification is performed using statistics of the first and second order whereas three classifiers are tested for performance (random forest, support vector machine, K-nearest neighbour). Koyama et al. [42] introduce a radargrammetric-based method for the estimation of disaster debris pile heights and volumes by means of post-event airborne polarimetric stereo-SAR data.

Multi sensor

Brunner et al. [11] propose a method operating at the level of individual buildings in a post-event high-resolution SAR image. By means of high-resolution optical pre-event imagery, 3d parameters of a building are estimated and used to predict the expected undamaged SAR signature. A similarity measure between the predicted and the actual SAR signature is drawn on to classify the building. A similar approach is presented by Wang and Jin [84] classifying multi-mutual information regarding pre-event optical and post-event SAR imagery in order to assess post-earthquake building damage. Dell'Acqua et al. [19] fuse SAR and optical data to classify buildings into three damage grades using averaged texture values computed at block-level.

1.2.2. SAR Simulators

The demands on a SAR simulator regarding radiometry and geometrical correctness differs with the application. A ray tracing based system, for instance, is required to enable the imitation of SAR specific effects. Table 1.1 provides a list of some commercial and experimental SAR simulators that are based on ray tracing. The individual simulators differ in their simulation principle and their capabilities and hence their ideal field of application. SAR raw data simulators (e.g. SARSIM, GRECOSAR) produce raw data that need to be processed to receive simulated SAR images, whereas SAR image simulators (e.g. CohRaS) directly generate the already processed amplitude/phase image. With the aim to give insight as to the scope of SAR simulation, subsequently a subset of the SAR simulators is presented in more detail:

Commercially available simulators

Xpatch is a high frequency radar signature prediction toolkit based on a combination of physical optics (PO) and the shooting and bouncing rays (SBR) technique, which enables fast solutions with reasonable accuracy. Xpatch was developed at Demaco/SAIC under leadership of the Air Force Research Laboratory and has evolved and matured through extensive validation efforts. The scattering data that Xpatch can produce and analyse include four kinds of radar signatures: Radar cross section (RCS), high resolution range profiles, SAR imagery and 3d scattering centers. Xpatch computes first bounce PO plus physical theory of diffraction (PTD) contributions and calculates multi-bounce ray contributions using geometrical optics (GO) and PO for complex vehicles with materials.

Table 1.1.: SAR simulators.

Name	Company/ Institution	
Xpatch	SAIC	commercial
RadBase	Surface Optics Corp.	commercial
VRSG Radar	MetaVR	commercial
SE-Workbench	OKTAL-SE	commercial
SARSIM	SDT	commercial
DIONISOS	OPEN (former Team-log)	commercial
RaySAR	Technical University of Munich	experimental
SAREF	DLR, Oberpfaffenhofen	experimental
PIRDIS	EADS, Ulm	experimental
SarViz	Stuttgart University	experimental
Mocem	Alyotech (founded by CELAR)	experimental
ITU SAR simulator	Istanbul Technical University	experimental
GRECOSAR	University Politecnica de Catalunya, Barcelona	experimental
CohRaS	Fraunhofer IOSB	experimental

SE-Workbench is a very large and powerful simulation software including visual, infrared and radar simulation. It contains the 3d modeling software SE-Physical-Modeler, the tool SE-Scenario for scene generation including moving objects, and a scene generator for large scenes using textured CAD models. All of the simulations are based on a ray tracing tool using SBR. The imaging radar simulator, SE-RAY-EM, uses both asymptotic field calculations (GO, PO, PTD, Equivalent Current Method) and the SBR forward ray tracing technique to generate a SAR image of the scene. It supports clutter materials (speckle) and multilayer materials.

Experimental simulators

RaySAR [5] is a ray tracing based SAR simulator that has been created within the Ph.D. Thesis of S. Auer at TU Munich. It uses a modified version of the open source software POV-Ray as core for the ray tracing. The main focus is set on geometrical correctness of the simulation. The simulator is capable of creating separate images for different levels of multi-bouncing, which can be used for the identification of double bounce lines and triple bouncing (e.g. at trihedral corner reflectors).

SAREF (SAR EFfects, [3]) was developed at the German Aerospace Center (DLR), Oberpfaffenhofen, and is based on efficient scattered field calculations that are performed on the GPU and are used for all direct scattering mechanisms. In addition, there is a fast ray tracing component for multi-bounce propagation. The additional information about the 3d location of the scattering centres that is present for the simulated scene is then used in combination with fast image reconstruction algorithms to simulate a reflectivity map, i.e. an ideal SAR image recorded by a (theoretical) SAR system with infinite bandwidth.

PIRDIS [57] has been developed at EADS, Ulm, Germany. It uses a clutter model derived from [80], height models of landscape to simulate clutter and RCS calculations for man-made objects that can be included in the scene as CAD models. The calculated RCS values are reported to be very close to real measurements. The RCS calculations are then used to generate the simulated SAR image.

SARViz [7] is a hybrid rasterisation and ray tracing SAR simulator created as part of the Ph.D. Thesis of T. Balz at Stuttgart University. In its basic version the image generation is achieved by rasterisation, which is a technique used widely for real-time rendering. All of the calculations are performed on the GPU and are in near real-time (i.e. more than 20 frames per second). Since rasterisation is not able to show multi-bounce effects, this was later augmented by a real-time ray tracing step that is able to simulate double bounce effects.

CohRaS®[1] [30] (Coherent Raytracing SAR Simulator) is a ray-tracing-based suite of SAR simulation tools developed at Fraunhofer IOSB. The suite contains a simulator for small scenes able to simulate these scenes at a very high level of detail, and a simulator for large scenes at high resolutions designed to be very memory efficient and to minimise calculation time. Main features are coherent simulation of images, i.e. both amplitude and phase of the received signal are simulated, an image generation process that is as close to the creation of a real SAR image as possible, and the use of ray tracing technologies to simulate a processed SAR image using the Narrow Beam Approach, i.e. no raw data are created.

1.3. Novel contributions of the thesis

In the scope of this thesis a novel method to perform damage detection on solely a post-event HR SAR image is presented [48, 46]. The individual processing steps are described and discussed in detail and based on a test data set [43] the methodology is evaluated. The functionality of this method relies on several contributing novel aspects:

Focus is set on the potential of using simulated SAR signatures as means to obtain an apt training data set. A simulation-based signature analysis of damaged buildings is presented, differentiating between a set of commonly occurring damage types [49]. Based on the findings conclusions are drawn regarding the prospects of a damage type specific detection of buildings and the most prominent aspect of damaged buildings in post-event SAR damage detection, namely debris.

A data set of realistic artificial SAR signatures of heaps of debris is simulated, with the aim of generating a capable training data set. The course of action to meet the involved demands on the 3d model design and the modelling of radiometric backscattering characteristics is described. In this context the texture variability of debris is determined regarding the influence of the geometric surface of heaps of debris and the backscattering properties of different materials [50]. The actual viability of the simulated signature is verified [45].

Sources of a similar textures are identified and a set of texture features is determined that shows susceptibility to the texture difference between debris and these similar textures [44, 45]. This is verified by means of a multidimensional scaling.

1.4. Structure of the thesis

In order to comprehend the course of action and the underlying methods, in Chapter 2 fundamentals are described. This involves the principle of imaging radar to understand the SAR image product, specifics on the SAR simulation suite in use, and basics on the applied image analysis techniques to be able to follow the proposed damage detection algorithm. Since the prospect of detecting damaged buildings that are based on debris occurrences relies on an understanding about building damage types in general, Chapter 3 provides an insight into common damage types and their signatures in SAR imagery. Following this, Chapter 4 focuses on the factor debris, including the general properties of debris occurrences and the concept of generating accurate synthetic SAR signatures of debris. The process is described, how suitable 3d models are generated and a radiometrically accurate backscattering is imitated, all with the aim of creating a data base suitable for the training of a supervised learning algorithm. In Chapter 5 a step-wise algorithm is introduced that provides the means to conduct damage detection based on the generated training samples. This involves the description of the individual processing steps as well as explanatory statements and investigations concerning the choice of action. Finally, in Chapter 6 a test data set is introduced and the debris detection results are shown and discussed. A conclusion for the thesis and an outlook are provided in Chapter 7.

---

[1]CohRaS is a registered name owned by IOSB, Fraunhofer-Gesellschaft. For reasons of simplicity the trade mark sign is omitted henceforth.

Chapter 2.

Fundamentals

This chapter provides the fundamentals that are required for the approach proposed in the following chapters, and is organised as follows: In Section 2.1, the theoretical basics on imaging radar are described, including image generation and image characteristics; Section 2.2 discusses specific image analysis techniques relating to feature extraction and a classification task; and in Section 2.3 the SAR simulator is described that is used to generate synthetic SAR signatures. Note that techniques that are employed in the following chapters are described in detail, whereas those that are mentioned for reasons of comparison are specified but shortly.

2.1. Basics on Imaging Radar

Imaging radar is a device in remote sensing creating two-dimensional images of the surface of the earth, where the two dimensions are called range and azimuth. These systems are active sensors, which means they have there own energy source and thus are independent of sunlight. Further, the radar wavelengths commonly used in remote sensing are not susceptible to absorption in the atmosphere of the earth. As a result, radar systems are weather independent to a large extent.

This section gives an overview on SAR imaging and is organised as follows: At first, a basic insight into radar waves is given; then, the SAR principles are explained and afterwards the characteristics of SAR images are covered, followed by a presentation of essential SAR specific processing techniques.

2.1.1. Radar

Radio frequency detection and ranging (Radar) stands for a detection system using electromagnetic (EM) waves in the microwave region. Regarding the EM spectrum, microwaves are a frequency band located in between the far infrared (IR) and the radio waves and cover frequencies from about 0.3 GHz to 300 GHz, as visualised in Figure 2.1. Depending on the application there are several (sub-)frequency bands mainly used for remote sensing, which are listed (according to IEEE standards) in Table 2.1. The wavelengths of these frequency bands are considerably larger than those of visible light, which has a great effect on the interaction with the atmosphere and the ground. Waves with wavelengths of more than 1 cm have the benefit of being largely unaffected by the weather, whereas bands of higher frequency are more prone to absorption in the atmosphere of the earth. EM waves are transverse waves, meaning they oscillate perpendicular to the direction of the wave propagation. A linear polarised wave is usually polarised either horizontally or vertically, according to the orientation of its electric field component [34]. Correspondingly, the receiving
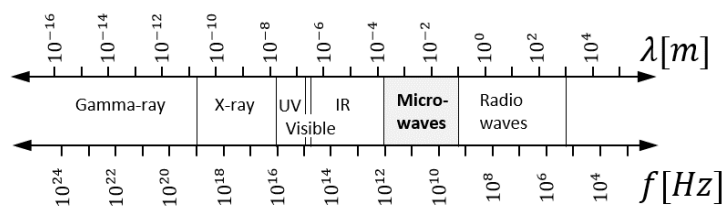

Figure 2.1.: Electromagnetic spectrum.

Table 2.1.: Radar bands commonly used for remote sensing.

Band	Frequency	Wavelength	Application examples
P-band	1-0.3 GHz	30-100 cm	geology, archaeology
L-band	2-1 GHz	15-30 cm	forestry, sea ice
S-band	4-2 GHz	7.5-15 cm	land use classification
C-band	8-4 GHz	3.75-7.5 cm	sea ice, agriculture, soil moisture
X-band	12.5-8 GHz	2.4-3.75 cm	high resolution mapping and surveillance tasks
Ku-band	18-12.5 GHz	1.67-2.4 cm	
K-band	27-18 GHz	1.11-1.67 cm	short range applications
Ka-band	40-27 GHz	0.75-1.11 cm	
W-band	100-40 GHz	0.27-0.4 cm	

antenna can also be configured to receive both, horizontally and vertically polarised waves. This allows for the horizontally and vertically co-polarised channels (HH and VV) showing the same transmit and receive orientation, and the cross-polarised channels (HV and VH), where transmit and receive orientation are switched. Due to the interaction with the surface of the earth, parts of the wave may change their orientation to some extent. This is called depolarisation and depends strongly on the terrain. Besides linear polarisation, there is also circular polarisation, which is mainly used for weather radar.

Scattering mechanisms

The interaction of radar waves with the ground (called scattering) varies greatly, causing the return signal intensities to range from very low to very high. How much intensity a target scatters back to the sensor is mainly influenced by its physical shape (including the roughness of its surface), the dielectric constant, and the local angle of incidence. Furthermore, the polarisation of the radar wave has an effect on the interaction with the target. Scattering can be divided into surface scattering, where the beam meets a homogeneous medium, and volume scattering, where the beam interacts with an inhomogeneous medium.

Surface scattering   The roughness of a surface with respect to the wavelength λ has a strong influence on how much of the radar wave is scattered back to the sensor. Essentially, a rough surface causes the radar wave to scatter in all directions, including the direction back to the sensor. As a result, such areas yield rather high intensities. This type of scattering can be described by the Bragg model [80]. In contrast, smooth surfaces function as a mirror and reflect the radar wave specularly away from the sensor, with an emergent angle equal to the angle of incidence. As a consequence, there is no return signal from these areas, except when the radar wave meets the surface perpendicularly, in which case an extremely strong return signal occurs. Figure 2.2(a) shows the bidirectional reflectance distribution functions for multiple types of surface scattering. Since the rating of roughness is directly dependent on the wavelength, in radar images different surfaces are considered rough than in optical images.

(a) Surface scattering for different levels of roughness
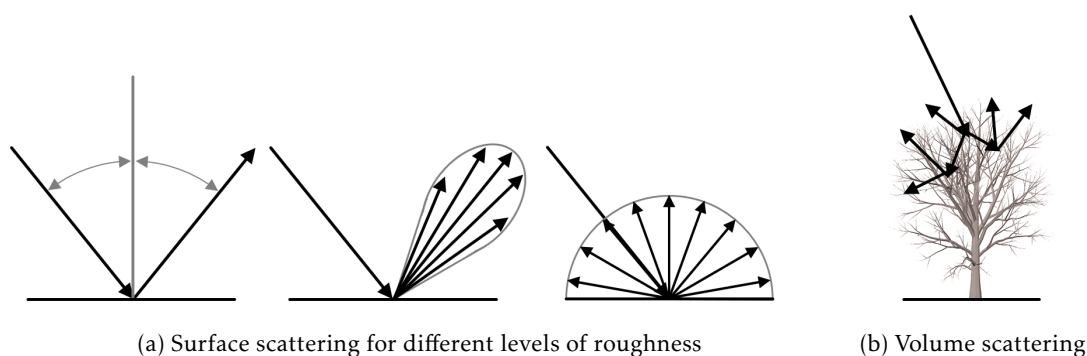
(b) Volume scattering
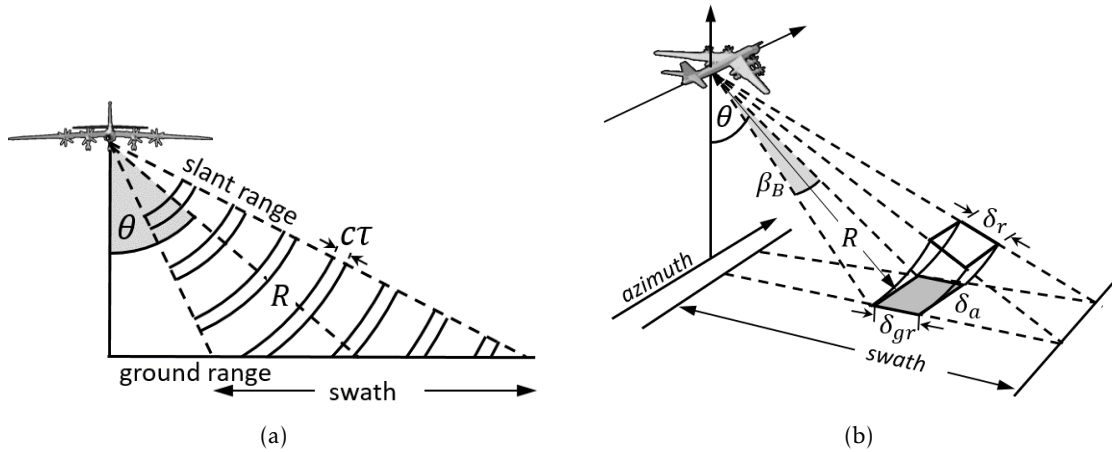
Figure 2.2.: Scattering Mechanisms.

Figure 2.3.: a) Acquisition geometry and b) resolution cell of a side-looking radar.

Penetration and volume scattering   Penetrating a medium the electromagnetic wave can experience absorption, thus gradually loosing intensity. The penetration depth regarding a medium is strongly dependent on the dielectric constant and thus on wavelength and moisture content, which can be observed well e.g. in sea ice or sand. A small wavelength (e.g. X-band) yields but little penetration in comparison to larger wavelengths (e.g. P-band). A similar effect can be seen in the canopies of vegetation, where small wavelengths are reflected from the canopy and large wavelengths penetrate as far as the stem and the ground beneath. In the case that an object does not consist of a homogeneous medium, the penetration of the radar beam causes a more or less random interaction with different kinds of media. The result is volume scattering [79] (depicted in Figure 2.2(b)), which occurs mostly in natural objects such as vegetation or dry snow and usually yields a medium backscattering intensity.

2.1.2. SAR principle

SAR systems can produce high-resolution images independent of sunlight and weather conditions. For these reasons they have become widely employed for numerous remote sensing application areas, such as environmental monitoring, military surveillance or agricultural classification. Before the SAR principle was established, conventional imaging radar systems were used, the so-called real aperture radar or also side-looking airborne radar.

The conventional systems consist of a long antenna mounted on a platform which moves in a forward motion and transmits a signal perpendicular to the flight path. The flight direction is referred to as azimuth, the line of sight as slant range and the illuminated ground range extent is called swath. Figure 2.3(a) illustrates the typical side-looking geometry with θ denoting the incidence angle. Electromagnetic waves are emitted in short pulses with durations τ and the speed of light c.

The side-looking geometry is rooted in the fact that radar is a distance measuring device and a dissolution of the incidence angle as with optical sensors is not possible. When two objects are too close to each other in range direction, the echo signals interfere and the objects cannot be dissolved. The range resolution describes the minimal distance for which a separation is possible and the two radar pulses of length $c \cdot \tau$ do not overlap. Since the offset between two returning pulses results from covering the range difference of the two objects twice, once towards the object and once returning, the range resolution amounts to

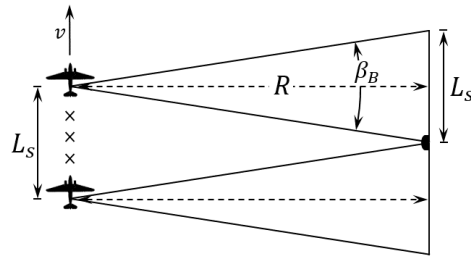$$\delta_r = \frac{c \cdot \tau}{2} \tag{2.1}$$

Figure 2.4.: Principle of a synthetic aperture radar.

Regarding the projection to ground range, the resolution is calculated as:

$$\delta_{gr} = \frac{c \cdot \tau}{2 \cdot \sin(\theta)} \tag{2.2}$$

where θ is the incidence angle of the beam at the centre point of the swath.

The range resolution is limited by the pulse duration, or since $BW \cdot \tau = 1$, inversely by the bandwidth BW of the emitted signal. The shorter the pulse, however, the smaller the amount of energy that can be transmitted, thus leading to a low signal to noise ratio (SNR). To elude this problem, pulse compression is used (in combination with matched filter processing). The bandwidth is increased, using linear frequency modulated (FM) long transmitter pulses, so-called chirp signals. Consequently, high average power can be transmitted whilst sustaining a good range resolution.

Figure 2.3(b) illustrates the resolution cell of the real aperture radar system. The crucial drawback of the conventional system is a rather bad resolution in azimuth direction. It is a function of the azimuth beamwidth β_B of the antenna and the slant range distance R between the sensor and the centre point of the swath.

$$\delta_a = \beta_B \cdot R, \quad \text{with} \quad \beta_B = \frac{\lambda}{L} \tag{2.3}$$

A decrease of the beamwidth results in a higher azimuth resolution, whereas the beamwidth in turn is limited by the azimuth length L of the antenna. So, the large slant range distances of satellite acquisitions and the hardware limitations regarding antenna lengths result in an unsatisfactory azimuth resolution.

The SAR system, meanwhile, attains a higher resolution in azimuth by synthetically enlarging the antenna. This is done by exploiting the motion induced different positions of the radar, thus creating the aperture sequentially. Figure 2.4 shows the SAR principle, where an object is illuminated from multiple positions (marked with an x) on the flight path.

For target points on the ground, the different sensor positions result in characteristic phase changes, which as a function of time are referred to as phase history. The derivative of the phase history equals the Doppler frequency that would theoretically be measured by a system that moves with a constant velocity between two sensor positions perpendicular to the line of sight. On this account and for reasons of simplicity, the Doppler terminology is used in the following.

The movement of the sensor causes the distance towards the objects first to decrease and then, after passing the shortest distance (in the zero-Doppler plane), to increase again. The relative movement between sensor and object results in a Doppler shift that changes for the various positions on the flight path. Since objects with a distance between them yield different relative speeds, their echo signal frequencies are shifted differently. By keeping track of the history of the Doppler frequency, the position of the object can be determined and the azimuth resolution is greatly increased. For this the radar system has to be coherent, meaning a high phase stability is required, which is implemented with a local oscillator that keeps timing with high accuracy.

The length of the synthetic antenna L_s is the distance travelled by the sensor during the transmission of the pulses, which is a function of the beamwidth β_B of the real aperture and the distance R. It is calculated as:

$$L_s = \beta_B \cdot R = \frac{\lambda}{L} \cdot R \tag{2.4}$$

With the increased antenna length, the beamwidth of the synthetic aperture in azimuth amounts to:

$$\beta_s = \frac{\lambda}{2 \cdot L_s} = \frac{L}{2 \cdot R} \tag{2.5}$$

where the factor 2 is due to the two-way path and the consequential doubling of the phase shifts. For the azimuth resolution of the SAR system follows:

$$\delta_a = R \cdot \beta_s = \frac{L}{2} \tag{2.6}$$

Remarkable is the independence of range distance and the fact that a smaller antenna yields a higher resolution in azimuth. For a more detailed description see [40].

SAR image formation

The returned signal is stored in a two-dimensional matrix of complex values, where amplitude and phase are represented by real and imaginary part. The two dimensions stand for the range direction (fast time) and the azimuth direction (slow time). However, the returned signal from a single point/object is dispersed both in range and azimuth direction. Thus, the raw data is hard to interpret but has to be focused first to gain a usable image. The main processing of the image formation (or also focusing) consists of two steps, range compression and azimuth compression. Since a multiplication in frequency domain is the equivalent to a convolution in time domain, but with a much lower computational cost, the two operation steps are usually preformed in the frequency domain. Unfocussed processing (Quick look processing) is an exception since it can be achieved by a moving average operation.

Range compression   In short, range compression is a matched filter operation in range direction. The signal is dispersed in range direction corresponding to the duration of the transmitted frequency modulated pulse. In order for the energy to be collected in one range pixel, for each range line a convolution is performed with the range reference function, which is the complex conjugate of the replica of the transmitted modulated pulse.

Azimuth compression   The signal is dispersed in azimuth direction corresponding to the duration it was in the beamwidth of the antenna. The changing distance between sensor and point target during that time shows as a hyperbola in the plane spanned by azimuth and slant range, the shape depending on the slant range distance. This hyperbola is known as the range cell migration (RCM) and usually is corrected before azimuth compression, meaning it is straightened to a range line. The RCM correction is complicated by the curvature of the earth, its rotation and possibly the antenna squint angle, causing further distortions of the hyperbola. It requires an estimation of the Doppler centroid and the Doppler rate.

The subsequent azimuth compression also is a matched filter operation / a convolution with a reference function. However, the reference function is the complex conjugate of the expected response of a point target and thus changes from near to far range. This turns out to also be a linear FM pulse (chirp), a long chirp in far range and a short chirp in near range. To reduce the sidelobes that accompany the matched filter operation due to the limited bandwidth of the system, amplitude weighting is performed. The weighting however also

Table 2.2.: Airborne sensors.

Sensor	Band	Resolution [cm]	Company	Country
PAMIR	X	<10	Fraunhofer FHR	Germany
MEMPHIS	W	30	Fraunhofer FHR	Germany
SETHI	X,L,P	<45	Onera	France
F-SAR	X,C,S,L,P	25	DLR	Germany
Lynx	Ku	<10	Sandia National Laboratories	USA
SMART Radar	X	<30	Hensoldt Sensors GmbH	Germany
STAR-Series	X	50	Intermap	USA

increases the width of the main lobe and thus results in a certain loss of resolution. Examples for common linear amplitude weighting functions are Hamming, Hanning, Taylor, and Kaiser [18], all dealing with a tradeoff between lowering the sidelobes and a degrading of the resolution. The reduced resolution is tolerable for most applications, however, for those it is not, non-linear weighting techniques (e.g. Spatially Variant Apodisation) are performed.

SAR imaging modes

There are various applications for SAR remote sensing that have very different demands regarding the acquisition properties. Primarily, these requirements include the resolution and the coverage. To fulfil these requirements, several acquisition modes are provided, which mainly exploit the trade-off between resolution and coverage:

Stripmap The Stripmap mode is the most commonly used imaging mode and was described in detail for the SAR principle at the beginning of this chapter. With a side-looking geometry a fixed swath is illuminated, whereas a changeable incidence angle yields a flexibility regarding the range position of the swath. The swath length is arbitrary and corresponds to the overflight distance. The swath width is limited by the pulse repetition frequency, since pulses can not be emitted and received at the same time.

ScanSAR In ScanSAR mode the limited swath width is widened, by enabling the steering of the antenna beam in elevation during the acquisition. Several sub-swaths are illuminated stepwise. As a result, the illumination time of the sub-swaths is reduced and a worsening of the azimuth resolution is the consequence.

Spotlight In Spotlight mode the antenna beam is steered, so that an area is illuminated for a longer time. This directly results in a larger synthetic aperture and a higher azimuth resolution. The drawback is a reduction of land coverage (that can possibly be recorded), since the next possible illumination area depends on the duration of illumination and the flight velocity.

2.1.3. SAR sensors

The number of operational SAR systems worldwide has grown over the last decades. In the following, a brief overview of recent operational SAR systems, both airborne and spaceborne, is given.

Airborne sensors Airborne SAR systems are predominantly experimental sensors used for technology development or deployed for military reconnaissance. As of today, the technical progress enables a spatial resolution of less than 15 cm. Depending on the platform (aircraft, unmanned aerial vehicles (UAV), cruise missiles), the aspect of motion compensation poses an essential challenge regarding SAR processing. Further emphasis is on real-time capabilities, making high demands on the computing capacity. Table 2.2 provides a list of some recent airborne sensors. In the end, the limited coverage as well as the weather requirements regarding aircraft operation render the use of airborne sensors inapt for a large branch of applications.

Table 2.3.: Recent civilian spaceborne SAR sensors.

Sensor	Band	Resolution [m]	Repeat Cycle [days]	Country	Life span
RADARSAT-1	C	10	24	Canada (CSA)	1995-2013
ENVISAT ASAR	C	30	35	Europe (ESA)	2002-2012
ALOS PALSAR	L	10	46	Japan (JAXA)	2006-2011
COSMO-SkyMed (4 Sat.)	X	1	16 (const: 4)	Italy (ASI)	2007
TerraSAR-X / Tandem-X	X	1	11 (const: 4-7)	Germany (DLR)	2007/2010
PAZ	X	1	11 (const: 4-7)	Spain	2018
RADARSAT-2	C	3	24	Canada (CSA)	2007
Sentinel-1 (2 Sat.)	C	5	12 (const: 6)	Europe (ESA)	2014/2016
ALOS-2	L	3	14	Japan (JAXA)	2014
COSMO-SkyMed-SG* (2 Sat.)	X	0.4	16 (const: 8)	Italy	2019/2020
TerraSAR-X-NG*	X	0.25	11	Germany	$\geq$ 2020

*Future mission

Spaceborne sensors The number of satellite missions using SAR sensors has grown over the years, both in the military and the civil branch. SAR reconnaissance satellites deployed by the military are required to provide high-resolution world wide mapping, an example being SAR-Lupe (Germany), which was launched in 2006 and operates with a spatial resolution of less than 1 m. The present-day civil branch provides a number of satellite missions covering the demand for a large diversity of applications. Table 2.3 supplies a list of some civilian spaceborne systems that are currently operating, have ended their life span recently, or are scheduled for the near future.

High resolution X-band SAR missions, such as TerraSAR-X can provide a spatial resolution of about 1 m with a repeat cycle of only a few days. Operated by DLR (and Airbus Defence and Space), TerraSAR-X was launched in 2007, carrying a phased array SAR antenna using X-band with a 31 mm wavelength and a 9.6 GHz centre frequency [22]. Available imaging modes as well as more detailed sensor specifications are listed in Table 2.4. TerraSAR-X and its twin satellite, TanDEM-X, fly in close formation on a helix orbit, with the primary aim of TanDEM-X being the generation of a high precision worldwide digital elevation model.

Comparable SAR missions include COSMO-SkyMed, which is conducted by the Italian Space Agency (ASI), and the Spanish satellite PAZ. Of nearly identical design to TerraSAR-X / TanDEM-X and launched into the same orbit, PAZ reduces the repeat cycle for the constellation to 4-7 days. For both missions, TerraSAR-X and COSMO-SkyMed, a new generation of satellites is planned for the near future (TerraSAR-X-NG and COSMO-SkyMed-SG).

ENVISAT ASAR, an environmental satellite operated by the European Space Agency (ESA), was carrying a C-band sensor and was formally announced inactive in 2012. The successor mission is called Sentinel 1 and consists of a set of four C-band satellites of which two have yet to be launched. RADARSAT-2 is a program of the Canadian Space Agency (CSA) launched in 2007 as a successor to RADARSAT-1, which stopped collecting data in 2013. The Japan Aerospace Exploration Agency (JAXA) operates ALOS-2, which carries an L-band sensor (PALSAR) and was launched as a replacement to the no longer operational ALOS.

2.1.4. Characteristics of SAR imagery

Radiometric properties

Depending on characteristics regarding radar and the target, the signal power that is received by the antenna is but a fraction of the signal that is transmitted. The radar equation describes the received signal as a function of these characteristics. A detailed summary is provided by Klausing and Holpp [40]. For a power P_t of the transmitted signal and an antenna gain G, the incoming power at a scatterer amounts to

$$P_{rs} = \frac{P_t G}{4\pi R^2} A_{rs} \tag{2.7}$$

13

Table 2.4.: Technical facts on the SAR sensor TerraSAR-X.

Orbit	Sun-synchronous repeat orbit
Repeat period	11 days
Inclination	97.44°
Altitude at the equator	514 km
Antenna type	Active Phases Array Antenna
Antenna size	4.78 m x 0.7 m
Centre Frequency	9.65 GHz (X-band)
Chirp bandwidth	150 MHz / 300 MHz
Nominal acquisition direction	Right side
Polarisation	Single and dual (depending on mode)
Imaging modes	Staring SpotLight, High Resolution Spotlight 300MHz, High Resolution SpotLight, SpotLight, StripMap, ScanSAR, Wide ScanSAR
Incidence Angle Range	15°- 60° (product availability: 20°- 55°)
Pass Direction	Ascending or descending

where A_{rs} is the effective receiving area of the scatterer at a distance R from the sensor. A fraction f_a of the incoming power is then absorbed by the scatterer and the rest is scattered in various directions. Accounting for the gain G_{ts} of the scatterer in sensor direction and assuming the same antenna and distances regarding transmitting and receiving, the power received by the antenna is

$$P_r = P_{rs}(1 - f_a)G_{ts}\frac{1}{4\pi R^2}A \tag{2.8}$$

where A is the effective aperture of the antenna. The contributions regarding the scatterer can be summarised in the radar scattering cross section as follows

$$\sigma = A_{rs}(1 - f_a)G_{ts} \tag{2.9}$$

Consequently, the received power can be described as

$$P_r = \frac{P_t G A}{(4\pi)^2 R^4}\sigma = \frac{P_t A^2 \sigma}{4\pi \lambda^2 R^4} \tag{2.10}$$

accounting for the relation between effective aperture and gain of the antenna: $A = \frac{\lambda^2 G}{4\pi}$.

The radiometry of the SAR image features some notable peculiarities, that do not occur in optical imagery.

Noise The received SAR signal is subject to two kinds of noise: multiplicative and additive. Signal dependent noises are referred to as multiplicative noise and are dependent on the strength of the signal. As such they can develop a level that is proportional to that of the signal [34]. The most prominent of multiplicative noises is known as speckle and develops as a result of the coherent nature of the system. Each resolution cell contains multiple scatterers that the transmitted wave interacts with. The thus forming echo signals can interfere with each other either constructively or destructively. Correspondingly, the coherent sum of phase and amplitude of the echo signals fluctuates strongly. To reduce speckle, a technique called multilooking, an incoherent averaging of the intensity image, is commonly performed, which however is accompanied by a loss of resolution. Another method is to apply adaptive filters (Frost, Lee, Kuan, Gamma Map etc.), which adapt the weighting throughout the image, or non-adaptive filters (Median filter, Fast Fourier Transform filters), which use a uniform weighting. Additive noise is mostly the result of receiver noises, most prominently thermal noise, which generally can be modelled as a Gaussian process. The additive noise contributions are described by the SNR.

Data statistics The nature of surfaces is decisive for the probability distribution of the received amplitudes A. Areas that are packed with multiple scatterers, which have similar backscattering characteristics and are

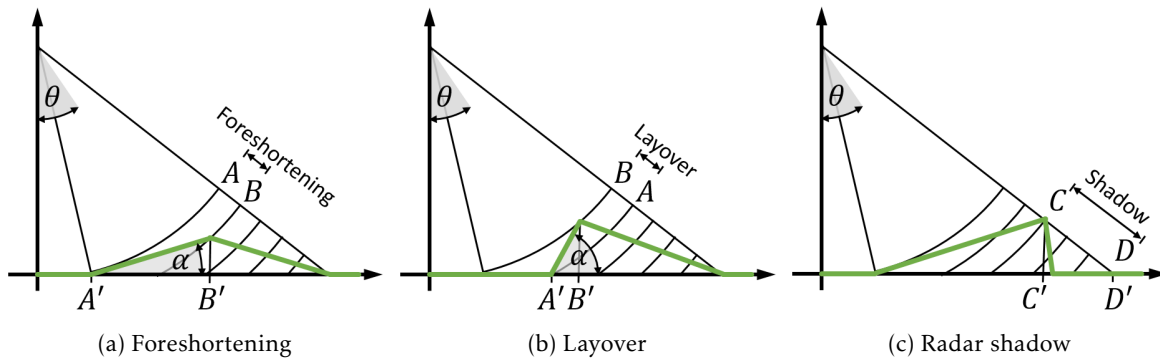(a) Foreshortening (b) Layover (c) Radar shadow

Figure 2.5.: Geometric distortions.

randomly distributed in the resolution cell, follow a Rayleigh distribution and exhibit a uniformly distributed phase over the range $-\pi$ to $+\pi$. This is not the case for areas that are dominated by single scatterers or an ordered pattern of scatterers, such as urbanised or otherwise structured land [40]. For the Intensity $I = A^2$ an exponential distribution can be assumed.

Geometric properties

Since the targets are positioned in the SAR image depending on their distance from the antenna, geometric effects develop, which depend on the incidence angle θ and the inclination of the target. Consequently, they are mostly observed in high terrain or other strong relief areas including building structures. These geometric effects are called foreshortening, layover and shadow. Furthermore, there are SAR specific image artefacts worth mentioning.

Forshortening   The Foreshortening effect occurs for areas that are sloped with respect to the planar area. Figure 2.5(a) illustrates how slopes that are inclined towards the sensor are compressed, whereas those that are inclined away from the sensor are dilated. As a result, sloped areas show higher or lower magnitudes depending on their inclination angle α. The maximal foreshortening is reached for $\alpha = \theta$, where the radar beam meets the ground in a right angle and thus the slope is compressed to a single resolution cell. This often occurs for the sidewards illumination of pitched roofs, where one side of the roof is projected to a foreshortening line.

Layover   In case the inclination angle α of a slope is larger than the incidence angle θ, the image geometry in inverted. This is due to the fact that points at the base of the slope have a larger distance to the sensor than those at the top of the slope, even though on the ground plane they are closer to the sensor. Figure 2.5(b) shows the development of this distortion called Layover effect. This effect is observed mostly in vertically built high structures or in very steep mountain slopes.

Shadow   Areas that are blocked from the view of the radar do not generate a backscattering signal and thus show as dark areas in the SAR image. Figure 2.5(c) shows that Radar shadow occurs for objects or terrains with a far range slope that is steep with respect to θ.

Double bounce and triple bounce   In the case that smooth surfaces are perpendicular to each other (so-called corner reflectors), radar waves bounce off two or three times and then head directly back to the sensor with but little intensity loss. Due to the wave components covering the same distance, being coherent regarding each other, their combination causes high intensities in one pixel (for a trihedral corner) or a line (for a dihedral corner). This occurs in particular at man made structures such as buildings.

Moving objects Since the SAR processor assumes a stationary scene, an interesting effect is caused by moving objects [34]. A stationary object causes a linear phase change (Doppler shift) while the sensor is passing by. If the object moves in a radial direction towards or away from the sensor, the Doppler history is changed. Consequently, in the final image the object is displaced in azimuth direction. Also, a movement in azimuth direction results in a blurring regarding azimuth direction. The detection of moving objects in SAR images is a field of its own and various methods can be applied, e.g. using sub-apertures.

Image products

The typically acquired image product is referred to as Single Look Complex (SLC), which is the basic format of the focused radar signal and a standard slant range product. It is generated by using the full synthetic aperture to achieve the highest possible resolution, which also entails a high amount of speckle. The signal is represented by a complex number with real (In-phase) and imaginary (Quadrature-phase) part for each image pixel. Due to its traits, this product is used for quality assessment and for applications requiring minimally processed data. Further SAR specific product formats include Ground Range Detected, which implies the projection to ground range maintaining the flight direction, Multi-Look Intensity, Multi-look Ground-range Detected and also products in map geometry.

2.1.5. SAR specific processing techniques

Depending on the intended application, the final SAR image requires further processing to be of use. The radiometry is influenced heavily both by sensor characteristics and by the acquisition geometry, moreover, the large dynamic range of SAR imagery can be challenging.

Radiometric calibration

To minimise radiometric differences between images of different sensors and in differing acquisition geometries, an absolute radiometric calibration is necessary. The calibration, however, is handled differently for every sensor. Since the focus of this work is on TerraSAR-X imagery, the specific calibration procedure of this sensor is explained in more detail. See also [1] for more information.

Even though factors regarding the targets themselves cannot be included, other contributions to the final image radiometry, regarding acquisition geometry, sensor characteristics and image processing, can be taken into account. This is done by computing the radar brightness (Beta Naught) and subsequently the backscatter coefficient (Sigma Naught):

Given the calibration factor k_s and the amplitudes $DN = \sqrt{I^2 + Q^2}$ calculated from real component I and imaginary component Q of the complex signal, the radar brightness amounts to

$$\beta^0 = k_s \cdot |DN|^2 \tag{2.11}$$

To further take into account the local incidence angle θ_{loc}, regarding an assumed flat plane, and the additive noise contributions to the signal (see Section 2.1.4), the calibrated intensities are calculated as

$$\sigma^0 = \beta^0 \cdot \sin \theta_{loc} - NESZ, \tag{2.12}$$

where $NESZ$ denotes the Noise Equivalent Sigma Zero (NESZ), which is the system noise specified regarding unit area in ground range. It is described as a polynomial of degree 3, taking into account the main additive noise contributions. As per [22] the NESZ is specified to be between -19 dB and -26 dB.
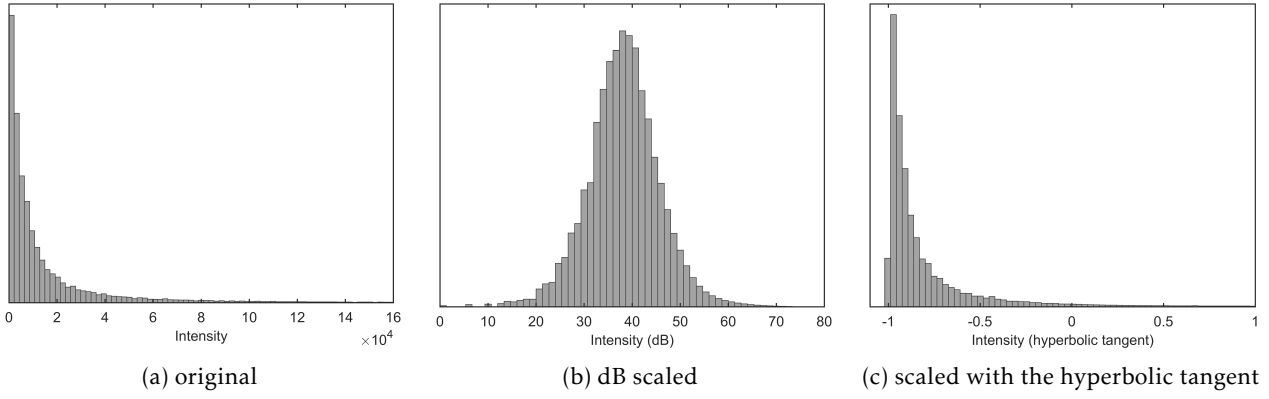
(a) original   (b) dB scaled   (c) scaled with the hyperbolic tangent

Figure 2.6.: Typical intensity distribution of a SAR image.

Dynamic Scaling

The real and imaginary components of the backscattered complex signal feature a Gaussian distribution. Consequently, the amplitude image is Rayleigh distributed and the intensity image has an exponential distribution. Figure 2.6(a) shows a typical distribution of a SAR intensity image. The dynamic range is very large while most of the information resides in the lower values, hence, a dynamic scaling is advisable.

Logarithmic scaling   Most common is a logarithmic scaling of the intensities I, since its result roughly follows a Gaussian distribution and thus allows for the use of standard methods of optical remote sensing. It is calculated as

$$\beta_{dB} = 10 \cdot \log_{10} I \tag{2.13}$$

In Figure 2.6(b) the corresponding distribution is plotted. The logarithmic scaling, however, has the disadvantage that its dynamic range has no fixed limits. As a consequence, it is not suitable for a lossless processing that assumes fixed dynamic ranges.

Hyperbolic tangent scaling   A scaling of the dynamic range with the hyperbolic tangent was introduced by Schmitt [72]. Due to the nature of the hyperbolic tangent, this has the benefit of a fixed dynamic scale in the range of $[-1, +1]$. The scaling is performed on the natural logarithm of the amplitudes, but with $\ln A = \frac{1}{2} \ln I$ can be expressed in intensities:

$$\tanh(lnA) = \frac{e^{2\ln A} - 1}{e^{2\ln A} + 1} = \frac{I - 1}{I + 1} \tag{2.14}$$

Figure 2.6(c) shows the distribution of the thus scaled intensities. This scaling method also has the benefit of stretching the dynamic range containing most of the information and compressing the high intensity range.

2.2. Image analysis techniques

Two main aspects of image analysis are the extraction of the textural content of an image and machine learning techniques that concern the subsequent processing. In the following, these two fields are examined more closely.

2.2.1. Texture analysis

Texture analysis involves the extraction of features that are able to numerically describe a texture with the aim of using these features for either texture discrimination, texture classification or shape analysis. Textural features are derived from both tonal/intensity and structural properties of a texture.

Many texture analysis techniques have been introduced in the previous decades. They can be grouped into four main categories: Structural approaches, which use texture elements (e.g. shapes, etc.) and placement rules to describe the texture, and consequently rely upon the presence of very regular elements in the texture; transform based approaches, which place the feature extraction in another domain using e.g. 2-D Fast Fourier, Gabor or Wavelet transform, thus benefiting from the selectivity of spatial filters; model based approaches, which use probability models (e.g. Markov-Gibbs random fields) or fractal models to describe texture; and lastly statistical approaches (see [74] for a more detailed account). In particular for textures of a seemingly random nature, which lack shapes and regular patterns, statistical approaches are well suited.

In statistical approaches, grey level statistics derived from the spatial domain are used as feature descriptors, whereas statistics of the first and second order are employed most often. First-order statistics (such as mean, standard deviation and higher order moments) describe the intensity distribution in the image, while second-order statistics consider the spatial inter-dependency of two pixels regarding a defined relative position. Local binary patterns [62] and run length matrices are to be named among established second-order statistics. Also, Laws texture energy masks [52], generated by a convolution of several simple vectors representing centre-weighted local average, edges, spots, are quite popular. Stated amongst the most popular and efficient features are a list of features introduced by Haralick et al.[32] computed on the Grey Level Co-occurrence Matrix (GLCM). For these and essential statistics of the first order a more detailed description is given in the following.

Main first order statistics

The statistics are specified on the probability density function (PDF) or its discrete estimate, the normalised histogram $p(l)$ of the image, where $l = 0, ..., L - 1$ denotes the grey levels regarding an (quantised) integer image.

- The *mean* grey level of the image is defined as

$$\mu := \sum_{l=0}^{L-1} l \, p(l). \tag{2.15}$$

- The grey level *variance* is calculated as

$$\sigma^2 := \sum_{l=0}^{L-1} (l - \mu)^2 \, p(l) \tag{2.16}$$

  with the *standard deviation* $\sigma = \sqrt{\sigma^2}$.

- The statistical feature *skewness* is defined as

$$\gamma := \frac{\sum_{l=0}^{L-1} (l - \mu)^3 \, p(l)}{\sqrt{(\sigma^2)^3}}. \tag{2.17}$$

  It is a measure based on the third central moment and as such describes the asymmetry of the PDF, with distributions skewed to the left yielding negative values and those skewed to the right yielding positive values.

- *Kurtosis*, also a feature that specifies the shape of the distribution, is calculated as

$$\kappa := \frac{\sum_{l=0}^{L-1} (l - \mu)^4 \, p(l)}{(\sigma^2)^2}. \tag{2.18}$$

As a measure based on the fourth central moment it describes the peakedness or flatness of the PDF. Any univariate normal distribution yields a value of 3, with higher values signifying a more peaked distribution and smaller values representing a flatter distribution.

- Lastly, *entropy* is estimated as

$$H := -\sum_{i=0}^{L-1}(p(l)\log p(l)), \qquad \text{with } p(l) > 0, \tag{2.19}$$

and can be interpreted as a measure of chaos, where the entropy increases with the level of disorder.

Grey Level Co-occurrence Matrices

The GLCM is formed by logging the joint occurrences (or probabilities) $P(l_1, l_2)$ of two grey levels (l_1, l_2) regarding a specified spatial pixel relation in the image.

Spatial pixel relation This relative position is defined by a distance d measured in pixels and by an orientation θ. Using a pixel distance $d = 1$ reveals the relation regarding the neighbouring pixels, whereas a distance $d = 2$ or more measures the relation regarding larger pixel offsets. Regarding the orientation θ of the pixel pair, usually the four angles 0°, 45°, 90°, and 135° are involved. Figure 2.7(a) illustrates these orientations for a pixel distance $d = 1$. The ideal spatial pixel relation is heavily dependent on the texture in question as well as the information that is sought. For rotation-invariant textures as well as to achieve robustness regarding sample rotation it is suggested to compute the GLCM over all of the directions. In Figure 2.7(b) the schematic process of a non-symmetric GLCM formation is visualised for $d = 1$ and $\theta = 0°$.

GLCM symmetry The result of this formation process is an asymmetric GLCM. However, since in most cases the order of appearance regarding a grey-level pair is non-essential, the GLCM usually is converted to a symmetric matrix, by summing the matrix with its transpose.

Quantisation The matrix dimension of the GLCM is determined by the number N_g of grey levels used in the pairing process and amounts to N_g x N_g. As a result, using full pixel depth can lead to computational problems due to enormous matrix dimensions as well as to a very sparse matrix when using small sample windows. To keep the computational load at a manageable level and to obtain a reasonably large average occupancy level, the pixel depth is usually quantised to a number as low as $N_g = 64$, or even $N_g = 16$.

Also, depending on the image type a non-linear quantisation may be necessary to achieve a reasonable occupancy level in the GLCM. There are three major types of quantisation: uniform quantisation, in which grey

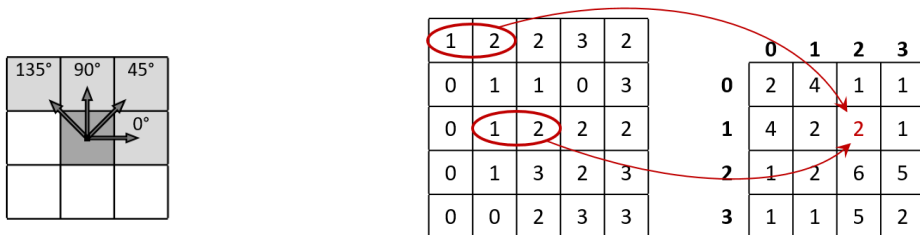(a) Orientation θ of pixel relation (b) Exemplary GLCM formation for $d = 1$ and $\theta = 0$

Figure 2.7.: Schema of GLCM formation.

levels are linearly divided into bins, not considering that information may be unequally distributed; Gaussian quantisation, which assumes normally distributed grey levels; and equal probability quantisation, which divides grey levels into bins of equal probability.

Haralick features

Haralick et al. [32] introduced a set of texture measures based upon the normalised GLCM

$$p(l_1, l_2) = \frac{P(l_1, l_2)}{\sum_{l_1=0}^{N_g-1} \sum_{l_2=0}^{N_g-1} P(l_1, l_2)}. \tag{2.20}$$

The 14 quantities are listed in the following:

- *Angular second moment* (ASM), also referred to as *Energy* or *Uniformity*:

$$f_1 := \sum_{l_1=0}^{N_g-1} \sum_{l_2=0}^{N_g-1} p(l_1, l_2)^2 \tag{2.21}$$

  This measure is defined as the sum of squared GLCM elements and as such is sensitive to high values $p(l_1, l_2)$. High ASM values predominantly occur for homogeneous images containing few grey levels which then cause few but high GLCM entries ($f_1 \in [0, 1]$, where 1 represents a constant image).

- *Contrast*:

$$f_2 := \sum_{l_1=0}^{N_g-1} \sum_{l_2=0}^{N_g-1} (l_1 - l_2)^2 p(l_1, l_2), \tag{2.22}$$

  The feature is sensitive to occupancies away from the GLCM diagonal and thus is a measure of local grey level contrast in the image ($f_2 \in [0, (N_g - 1)^2]$, where 0 represents a constant image).

- *Correlation*:

$$f_3 := \frac{1}{\sigma_x \sigma_y} \left(\sum_{l_1=0}^{N_g-1} \sum_{l_2=0}^{N_g-1} l_1 l_2 \, p(l_1, l_2) - \mu_x \mu_y \right) \tag{2.23}$$

  where μ_x and μ_y denote the means and σ_x and σ_y denote the standard deviations of the marginal row and column probabilities p_x and p_y

$$p_x(l_1) := \sum_{l_2=0}^{N_g-1} p(l_1, l_2), \qquad p_y(l_2) := \sum_{l_1=0}^{N_g-1} p(l_1, l_2). \tag{2.24}$$

  It measures the linear dependency between the grey levels of specified relation ($f_3 \in [-1, 1]$, where 1 and -1 represent perfectly positively and negatively correlated images).

- *Variance*

$$f_4 := \sum_{l_1=0}^{N_g-1} \sum_{l_2=0}^{N_g-1} (l_1 - \mu)^2 \, p(l_1, l_2) \tag{2.25}$$

  where μ is the mean grey level of the image. This feature is a measure of heterogeneity since it is sensitive to the variability of the pixel pair grey-levels, showing high values for divergence from the mean.

- *Inverse difference moment* (IDM) also referred to as *Homogeneity*

$$f_5 := \sum_{l_1=0}^{N_g-1} \sum_{l_2=0}^{N_g-1} \frac{1}{1 + (l_1 - l_2)^2} \, p(l_1, l_2) \tag{2.26}$$

This measure is sensitive to occupancies close to the GLCM diagonal, which represent the occurrences of small grey level differences, and as such is a quantity of homogeneity ($f_5 \in (0, 1]$, with 1 representing a diagonal GLCM).

- *Sum average*

$$f_6 := \sum_{k=0}^{2(N_g-1)} k \, p_{x+y}(k) \qquad (2.27)$$

with p_{x+y} denoting the cross-diagonal probabilities

$$p_{x+y}(k) := \underbrace{\sum_{l_1=0}^{N_g-1} \sum_{l_2=0}^{N_g-1}}_{l_1+l_2=k} p(l_1, l_2) \qquad (2.28)$$

where $k = 0, 1, ..., 2(N_g - 1)$.

- *Sum variance*

$$f_7 := \sum_{k=0}^{2(N_g-1)} (k - f_8)^2 \, p_{x+y}(k) \qquad (2.29)$$

- *Sum entropy*

$$f_8 := - \sum_{k=0}^{2(N_g-1)} p_{x+y}(k) \, \log[p_{x+y}(k)] \qquad (2.30)$$

- *Entropy*

$$f_9 := - \sum_{l_1=0}^{N_g-1} \sum_{l_2=0}^{N_g-1} p(l_1, l_2) \, \log[p(l_1, l_2)] \qquad (2.31)$$

- *Difference variance*

$$f_{10} := \text{variance of } p_{x-y} \qquad (2.32)$$

with p_{x-y} denoting the diagonal probabilities

$$p_{x-y}(k) := \underbrace{\sum_{l_1=0}^{N_g-1} \sum_{l_2=0}^{N_g-1}}_{|l_1-l_2|=k} p(l_1, l_2) \qquad (2.33)$$

where $k = 0, 1, ..., N_g - 1$

- *Difference entropy*

$$f_{11} := - \sum_{k=0}^{N_g-1} p_{x-y}(k) \, \log[p_{x-y}(k)] \qquad (2.34)$$

- *First information measure*

$$f_{12} := \frac{f_9 - H_{xy1}}{\max\{H_x, H_y\}} \qquad (2.35)$$

with H_x and H_y denoting the entropies of p_x and p_y, whereas H_{xy1} and H_{xy2} are defined as

$$H_{xy1} := - \sum_{l_1=0}^{N_g-1} \sum_{l_2=0}^{N_g-1} p(l_1, l_2) \, \log[p_x(l_1) \, p_y(l_2)] \qquad (2.36)$$

$$H_{xy2} := - \sum_{l_1=0}^{N_g-1} \sum_{l_2=0}^{N_g-1} p_x(l_1)\, p_y(l_2)\, \log[p_x(l_1)\, p_y(l_2)] \tag{2.37}$$

- *Second information measure*

$$f_{13} := \{1 - \exp[-2(H_{xy2} - f_9)]\}^{\frac{1}{2}} \tag{2.38}$$

Note that an implementation of the quantities necessitates that any zero-inputs to the log functions are replaced by the minimum distance that the arithmetic program can recognise.

2.2.2. Machine learning

There is a wide range of machine learning algorithms, which commonly are grouped by their learning style into supervised, unsupervised, and semi-supervised learning algorithms. Unsupervised learning describes the approach of extracting an underlying distribution (inherent similarity) using training data that is not labelled into categories. Common applications include clustering, anomaly detection, latent variable models, and association mining problems (with popular algorithms, such as k-means). In contrast, supervised learning, which in practice is used by the majority of algorithms, exploits labelled training data to learn to predict an outcome. It is further grouped into algorithms that deal with regression problems (predicting continuous real-valued output) and those that handle classification problems (predicting categories). Since this work deals with a classification task, the challenges of regression problems are not reviewed further.

In the following, a more detailed insight is given into three popular classification algorithms, namely Random Forest, Support Vector Machines (SVMs), and Convolutional Neural Networks (CNNs). Afterwards, commonly used performance measures are discussed briefly.

Random Forests

First introduced by Ho [35] and Breimann [8], and based on the concept of decision trees, the random forest algorithm still belongs to the most successful methods regarding classification and regression tasks. Decision trees are a widely used tool in machine learning to specify the decision making process, with nodes referring to features, branches to decisions and leafs to an outcome, which in the case of a classification problem is a class. Trees are usually grown starting with the upmost node (root node) and recursively creating nodes/decisions based on the best splitting performance regarding labeled training samples. This is called top-down induction of decision trees and falls in the category of greedy methods due to the locally optimised node/decision. The splitting is repeated recursively either up to the point that all samples have the same label or a specified stopping criterion (such as the requirement of a minimum number of samples per leaf or a maximal tree depth) is invoked. The growing of a node/decision requires for one, a decision on the feature to be used and secondly the respective splitting condition. For this, a measure of impurity is introduced (such as e.g. entropy impurity, variance impurity, Gini impurity, and misclassification impurity), representing the performance of splitting the labeled data cleanly into the categories. Based on labeled training data, the optimal splitting condition for each node is found by maximising the decrease of impurity for all possible splitting conditions. For further information on decision trees see [21].

The concept of the random forest algorithm is to use an ensemble of random decision trees, thus using many weak learners to build a strong learner. By means of bootstrap aggregation (also called bagging), which is a process of random uniform sampling with replacement, the training data are subdivided. On these subsets decision trees are fitted, using a random selection of the p input features (feature bagging), which is done in order to lower the correlation between decision trees. There are several hyperparameters that are essential for the classification performance: m, the maximum number of features considered in the process of building a tree, which is suggested to be set to $m = \sqrt{p}$, but depends on the problem at hand; B, the number of trees

created for the random forest, which is usually set as high as the computational cost allows for; and n_{min}, the minimum number of leaf samples that is required to split a node, and is decisive for a balance between under- and overfitting. By default, labels are predicted using a majority vote over the trees, however a weighted voting can be applied. The posterior probability $\hat{P}_t(c|x)$ regarding a sample x is computed for each class c and each tree t. The class that scores the largest weighted average $\hat{P}_{bag}(c|x)$ over the tree selection S is then appointed the predicted class for that sample:

$$\hat{y}_{bag} = \arg\max \hat{P}_{bag}(c|x) \tag{2.39}$$

with

$$\hat{P}_{bag}(c|x) = \frac{1}{\sum_{t \in S} w_t} \sum_{t \in S} w_t \hat{P}_t(c|x) \tag{2.40}$$

where w_t denotes the weight of the tree t. A cost sensitive learning can be introduced e.g. by passing a classification cost matrix C that penalises certain classes, where rows denote the true classes and columns denote the predicted classes. The out-of-bag error is a popular method of assessing the prediction error and is often used for tuning the parameter values.

Compared to other classifiers, the random forest algorithm can perform quite well, while little tuning is required [33]. Since the hyperparameters are straightforward and easy to understand, the method is quite user-friendly. The process of feature bagging is an internal feature selection causing the random forest algorithm to be robust to correlated/redundant and noisy features. The run-time performance can be problematic for a large number of trees, hence the aim is to reach a good balance between run-time and prediction performance.

Support Vector Machines

An approach to classification using so-called support vectors was introduced in [82]. The concept of SVMs is to form a separating hyperplane in a high- or infinite-dimensional space, such that the distance to the nearest training vectors, which are referred to as support vectors, is maximised. This leads to a quadratic optimisation problem.

For linearly separable problems, this is solved by introducing Lagrangian theory. Employing soft-margin training allows for some patterns to remain within the margin and thus enables the separation of otherwise non-separable sets. However, often sets are not linearly separable. This is approached by taking advantage of the kernel trick, which implies the use of non-linear kernel functions in order to transform the data into high-dimensional feature space. Ideally, a linear discrimination hyperplane is found, that represents a non-linear hypersurface in the original feature space. Kernel functions are a special class of functions that induce a scalar product in the high-dimensional space. Since this is all that is needed for the calculation of hyperplanes and distances, the actual mapping from the original space to feature space does not need to be specified. This approach allows for the use of a linear classifier for a non-linearly separable set. In cases where there is not a 2-class classification problem but an N class problem, N 2-class classifiers are combined, by discriminating each class from the remaining training set. A more detailed description regarding SVMs is provided in [74]. It is to be noted that SVMs are prone to different value ranges in features, leading to an unbalanced feature influence. This can be overcome by a normalisation of the feature vectors before they are fed to the SVM.

Convolutional Neural Networks

The concept of neural networks rests on single neurons (processors), which produce a single output based on multiple weighted inputs. The output (of the neuron) is provided by a so-called activation function, such as a rectified linear unit (ReLU) function (defined as $f(x) = \max(0, x)$), a Maxout function or a sigmoid function.

Multiple interconnected neurons, which usually are structured into layers, form a neural network (input layer, multiple hidden layers and output layer). The learning process of a supervised neural network starts with randomly initialised weights and a forward-propagation. In order to rate the network output with respect to the actual labels of the training set, a loss function, such as Softmax, Mean Squared Error or Cross Entropy Loss is defined. By means of backpropagation, which implies the recursive use of the chain rule to compute gradients of the loss function (gradient descent), the weights are updated. Ideally, the iterative performance of these steps leads to a convergence of the gradient descent and to a (global) minimum of the loss function.

CNNs assume the input to be images and introduce the concept of convolutional layers into the network structure. These exploit the spatial local correlations in images (local connectivity) by spatially limiting the connections between neighbouring layers (receptive field), in contrast to fully-connected layers, which imply a full pairwise connectivity between neurons of neighbouring layers. This considerably reduces the free parameters of the network (weight sharing) and thus its computational complexity. The typical structure of a CNN involves the use of different types of layers (aside from input layer): *convolutional* layer; *ReLU layer*, which invokes the activation function; *pooling layer*, which performs a spatial downsampling (usually max pooling is used); *dropout layer*, which can reduce overfitting by randomly disregarding some neurons; *fully-connected layer*; and output layer, which in the form of a fully-connected layer computes the class scores.

Meanwhile, to enforce that convolutional layer outputs are of the same size as the convolutional layer inputs, so-called zero-padding is used. The performance of the CNN depends on several factors: Structure of the network, initialisation at the beginning, learning rate, optimisation method, and so on.

Performance measures

Since the aptitude of a classifier depends on the specific problem, there is no individual optimal algorithm for all problems. For evaluation, the classifier performance is usually quantified by a confusion matrix, visualising the correctly and incorrectly classified instances in relation to the target and the predicted classes (see Table 2.5). Based on these instances, in binary classification termed true positive (TP), false positive (FP), false negative (FN) and true negative (TN), several performance measures are defined. The *true positive rate* (TPR), also referred to as sensitivity or completeness, as well as the *accuracy* (ACC) and the *positive predictive value* (PPV), which is also referred to as precision or correctness, are such measures. They are specified as

$$TPR = \frac{TP}{TP + FN} \tag{2.41}$$

$$ACC = \frac{TP + TN}{TP + FP + FN + TN} \tag{2.42}$$

$$PPV = \frac{TP}{TP + FP} \tag{2.43}$$

Accuracy is considered problematic, since it assigns equal weighting to all errors (FP and FN). More suitable for uneven class distributions is the F_1 score, defined as

$$F1score = 2 \cdot \frac{PPV \cdot TPR}{PPV + TPR}. \tag{2.44}$$

Further established performance measures include: ROC curve, Log-Loss, Cohen's Kappa metric, etc. [67].

Table 2.5.: Confusion matrix for a binary classification.

		Predicted class	
		Positiv	Negativ
True class	Positiv	TP	FN
	Negativ	FP	TN

2.3. SAR simulation suite CohRaS

As summarised in Section 1.2.2 there are a number of SAR simulators available. The coherent ray-tracing SAR simulation suite CohRaS was developed at Fraunhofer IOSB and provides the required prospects to simulate geometrically and radiometrically correct SAR signatures. In the following, the main processing steps are described in detail, starting with the geometric aspect of generating accurate SAR signatures. After that, the solution used for the radiometric modelling is presented and lastly the individual steps of the image formation are focused on. For a more detailed description see [30] and [31].

2.3.1. Geometric aspect

The SAR acquisition process and the subsequent unravelling of the signal by means of a Range-Doppler processor is substantial and computationally very costly. Using a narrow-beam approximation rather than the wide beam in combination with the SAR acquisition principle, the simulator can bypass the generation of raw data. Instead, already processed amplitude and phase images are simulated using a ray tracer. Since diffuse scattering and specular reflections entail different requirements regarding the computational approach they are handled separately.

Diffuse scattering

For the computation of direct reflections, as is the case for diffuse scattering, using the narrow-beam approximation suffices to achieve a good approximation of the SAR image. For this the simulator makes use of raytracing techniques, more precisely the fast raytracing algorithm described in [2], and assumes a look angle perpendicular to the flight direction. Before the raytracing process, the 3d model of the scene to be simulated is divided up into voxels (3d pixels), where the edge length is represented by the computation parameter *Geometric Resolution*. Since raytracing is done for each of these voxels (containing at least part of a polygon) a small *Geometric Resolution* results in good representation of the scene, but also brings about a high computational load. A reasonable value is roughly half the wavelength λ, since electromagnetic waves are only affected by objects down to that size. For every voxel, more precisely, for the centroids of the intersections between voxel and model polygons, a ray is traced towards the sensor location and the distance is stored. The distance information is used in combination with the parameter *Wavelength* to compute the corresponding phase. For each pixel in the simulated image the components of the different voxels are added coherently. As described in Section 2.1.4, the development of speckle in real SAR imagery is caused by the coherent summation of the contributions corresponding to multiple scatterers in the resolution cell. The simulator generates speckle by imitating this course of events. Several scatterers are randomly yet reproducibly placed on the polygons of every voxel (the number is defined by the parameter *Number of Point Scatterers*) and their returns are added coherently. The result is a Rayleigh distribution for the simulated amplitudes.

Specular reflections

Specular reflections require another approach since the correct positioning of a multi-bounce reflection is not covered by the narrow-beam approximation. Raytracing is used as well for this, however, additional processing is necessary to determine the correct pixel position in the simulated image. Taking into account the normal vectors of the polygons and the acquisition parameters, rays are traced up to a given number of bounces, which is definable by the parameter *Number of Bounces*. Additionally, for each bounce a diffusely backscattered component is computed, that directly returns to the sensor position. The positioning is computed by modelling the processing of a real SAR image using a Range Doppler processor. For this the distance d (propagation time of the signal) is calculated, regarding the path from sensor to the bounce locations and back to the sensor. Also, the Doppler frequency shifts are computed, which develop as a result of the changed azimuth position

concerning transmitted and returning signal. Knowing the distance and doppler frequency, the specific point in the hypothetical model plane is then derived by locating the corresponding line of Equidistance (by means of a sphere of diameter $\frac{d}{2}$) and check for the correct doppler frequency. The shortest distance of this point to the flight path represents the range position of the corresponding pixel, whereas the azimuth position is given by the sensor azimuth location, for which the shortest distance has occurred.

2.3.2. Radiometric aspect

Section 2.1.4 provides the mathematical basis for the computation of the returning power, regarding the non-target related factors. The modelling of the backscattering coefficient σ, which combines all target related factors, is realised by separately calculating the contribution of diffuse scattering and specular reflections. For a reasonable radiometry in the simulated SAR image, various materials are imitated by assigning different backscattering properties to the polygons of the 3d scene.

Diffuse scattering Assuming a hypothetical maximal backscattering coefficient σ_0 which occurs in absence of any specular reflections for a local incidence angle $\alpha = 0°$, the radar backscattering coefficient for diffuse scattering is calculated according to Ulaby [79] as

$$\sigma_{diff} = \sigma_0 \cdot \cos^2(\alpha) \tag{2.45}$$

where α denotes the angle between the polygon normal and the incident ray.

Specular reflections The backscattering coefficient regarding specular reflections follows a modified model according to Phong [65], which assumes that specular reflections disperse somewhat around the fixed outgoing angle. Accounting for the angle β between the actual outgoing ray and the theoretical accurate outgoing direction and σ_{max}, which describes the maximum value that is reached for a specular reflection at an incident angle perpendicular to the polygon, it calculates as

$$\sigma_{spec} = \sigma_{max} \cdot (1 - d) \cdot \cos^x(\alpha) \cdot \cos^y(\beta) \tag{2.46}$$

where α once again denotes the local incidence angle, x and y are parameters to effectively model the form of the specular reflection lobe and d is a dampening factor.

The final backscattering is then defined as

$$\sigma = \max(\sigma_{diff}, \sigma_{spec}) \tag{2.47}$$

NESZ To imitate the (additive) system noise, a random complex number is added to each pixel, consisting of an element from the interval $[-\pi, +\pi]$ for the phase part and a Rayleigh distributed random variable for the amplitude part. To allow for an adjustment, the mean of the Rayleigh distribution is a settable parameter (*NESZ*).

2.3.3. Image formation

Input - CAD model The base input for the simulation is a 3d model of an arbitrary scene, which, depending on the scene, may require the insertion of a ground plane in order for accurate bounce effects to develop. The level of detail is directly related to how realistic the final simulated image can be. However, since the computational cost increases with the number of polygons in the 3d model, this is reasonable only up to the dimensions of the chosen wavelength. Further, for the simulation to be true to reality, it is particularly crucial

that right angles are accurate, otherwise typical multi-bounce reflections have no chance of occurring (e.g. this is a problem with triangulated LIDAR data as input model).

Input - Simulation parameters The simulation process requires a set of parameters, which include acquisition parameters (e.g. *Sensor Altitude*, *Ground Distance*, *Aspect Angle*), sensor parameters (e.g. *System Resolution*, *Pixel Spacing*, *Wavelength*), processing parameters (e.g. *Windowing*) and also several computation parameters, that are mainly necessary to optimise the computation process.

Input - Material properties By adjusting σ_0, σ_{max}, x, y and d the backscattering coefficient of different materials can be replicated. This is a crucial step, which requires recursive tuning. Every polygon is then assigned a material with defined backscattering properties.

Step I - Raytracing Using the acquisition parameters, raytracing is conducted for every voxel and by coherently summing up all the components that belong to the same resolution cell, a complex valued image called a reflectivity map is generated. This map has the pixel size defined in the parameter *Geometric Resolution* and is equivalent to a SAR image produced using a system with infinite bandwidth. Further processing is done in order for it to acquire the characteristics of a real SAR image.

Step II - Coherent Downsampling In order to imitate the limiting effect of range gating and the pulse repetition frequency, the reflectivity map is coherently downsampled to the resolution of the system, which is defined by the parameter *System Resolution*.

Step III - Convolution with Impulse Response The limited bandwidth of real SAR systems causes the presence of sidelobes in the SAR image. To mimic the limited bandwidth, the downsampled reflectivity map is convolved with the impulse response, which is implemented for two selectable windowing functions (Hamming and a rectangular window). The convolution causes the typical blurring of the image and the bright cross-like structures seen in strong scatterers.

Step IV - Oversampling The last step consists of an oversampling to a pixel spacing smaller than the resolution of the system and adjustable by means of the parameter *Pixel Spacing*. This is done using a sinc-interpolation on the image and imitates the oversampling of the real signal to prevent aliasing.

Output The final simulation result is the equivalent to a processed SAR image, consisting of amplitude and phase image.

Chapter 3.

Properties of damaged buildings

The detection of building damages in remote sensing data builds on a sound understanding regarding possible damage types and their signature characteristics. These types and their characteristics can differ considerably, depending on various aspects.

The type of building, as in high-rise, small residential building or industrial construction, is sure to produce an impact on what damage types can possibly develop. A substantial contribution for this is the differing construction materials used for different building types. Since construction techniques are heavily culture-bound, both, construction material and construction type, predominantly depend on the building location. As the following assessment focuses on damages in industrialised countries, the construction types of other regions of the world are not accounted for. According to the World Housing Encyclopedia [13], the prevailing construction types consist of concrete structures, masonry, steel buildings, and timber structures. Timber structures are most common in one and two story residential buildings, whereas masonry can be found both in residential and commercial areas as well as in old brickwork or stonework buildings (as e.g. churches). Meanwhile, concrete structures are more characteristic for multi-story buildings and commercial areas, with steel structures used mainly for industrial buildings.

The material in use is of great impact, not only on the nature of the potential damage types, but when regarding SAR image exploitation, also on the signature of the intact or damaged building. Materials with a surface that is rough relative to the sensor wavelength cause mainly diffuse scattering, whereas smooth surfaces reflect mostly specularly. For X-band SAR sensors, having a wavelength of 2.5 to 3.75 cm, this means that a wooden surface, or even a concrete surface will result in higher direct backscattering intensities than the smooth surface of a metal bar. Another aspect, regarding potential damage types, is the underlying cause of a building damage. These being, first and foremost, natural disasters such as earthquakes, but also bomb damage or controlled blasts. Especially for severe damages with at least a partial collapse of the building these show quite similar characteristics.

This chapter addresses potential building damage types and their characteristics in the SAR signature. In the following, SAR signature always refers to the signature of High Resolution Spotlight (HS) imagery of an X-band sensor. With the objective of damage assessment concerning earthquake damages in European/industrialised countries, the focus is mainly on concrete buildings, a construction type commonly used in Europe/industrialised countries. The chapter is organised as follows: Section 3.1 gives insight into the definition of established damage types; in Section 3.2, these damage types are analysed regarding their SAR amplitude signatures; and in Section 3.3 conclusions are drawn, as to how this can be used for a damage detection approach using post-event imagery only.

3.1. Schematic definition of damage types

Schematic damage types are always highly generalised and thus do not cover all shapes and range of materials of real life constructions. They do, however, describe characteristics that are applicable to most custom buildings. The prospect of working with SAR imagery of pixel sizes in the range of one metre reduces the scope of building damage types of interest. Only severely damaged buildings are capable of causing characteristic

Table 3.1.: Damage scale (EMS-98).

Damage grade	Description
Grade 0	No damage
Grade 1	Slight damage (Hair-line cracks in few walls)
Grade 2	Moderate damage (Fall of large pieces of plaster)
Grade 3	Heavy damage (Large and extensive cracks in walls)
Grade 4	Very heavy damage (Serious failure of walls)
Grade 5	Destruction (Total collapse)

signature changes. Also, due to focussing on concrete buildings, the scope of damage types is further narrowed down. The European Macroseismic Scale (EMS-98) [27] introduced a categorisation system concerning damages regarding concrete buildings. Table 3.1 lists these damage grades in full. The first four grades (0-3) describe building damages up to a state where building walls feature extensive cracks, but the building is still standing. Damage types falling under these categories are unlikely to show characteristic signatures. Focus is on the damage grades 4 and 5, describing profound damages involving the collapse of walls. Schweier et al. [73] defined 10 damage types for very heavy building damages, as an enhanced adaptation of the damage type list introduced by Okada et al. [63]. Table 3.2 shows a list of these damage types, including several feature sub-types. All listed damage types are severe enough to demand immediate attention in an emergency scenario. Following in the next section, the analysis of damage type specific characteristics in SAR signatures is based on this list of damage types.

Table 3.2.: Damage types (Schweier).

Damage type	Description
Type 1	Inclined plane
Type 2	Multi layer collapse
Type 3	Outspread multi layer collapse
Type 4	Pancake collapse (first, intermediate or upper story)
Type 5	Pancake collapse (multiple stories)
Type 6	Heap of debris on uncollapsed stories
Type 7	Heap of debris (also with planes, with vertical elements)
Type 8	Overturn collapse, separated
Type 9	Inclination or overturn collapse
Type 10	Overhanging elements

3.2. Damaged buildings in SAR amplitude imagery

Before describing the signature characteristics of specific building damage types, it is necessary to summarise the main features of an intact building. The signature of an intact flat-roofed building consists mainly of a dihedral corner, resulting from specular bounce involving the ground and the vertical wall, little direct reflection, shadow and trihedral corner points resulting from the window ledges in combination with the highly specular glass. Depending on the backscattering properties of each material, the intensities for each of the signature elements can vary distinctly. Figure 3.1(a) shows the signature of a basic high-rise building, located in St. Louis, in a HS TerraSAR-X image, with the range direction pointing from bottom towards top. In the following, this image orientation will be retained for all visualised SAR images. Small dihedral and trihedral corner reflectors formed by window ledges result in a high intensity pattern of points. The schematic formation of the main signature parts is depicted in Figure 3.1(b), for both a high-rise building and a gabled roof building. A characteristic trait for a sloped roof is the sometimes severe foreshortening of the roof area that is turned towards the sensor. This culminates in the case that the incoming wave is perpendicular to the roof area, projecting all roof backscatter to a line.

How this signature can change for different types of damages is the subject of this section. A thorough observation of building damage types in real SAR imagery, however, is not feasible. Disregarding set-up scenarios,

(a) SAR signature of high-rise building (HS TerraSAR-X image, St. Louis)
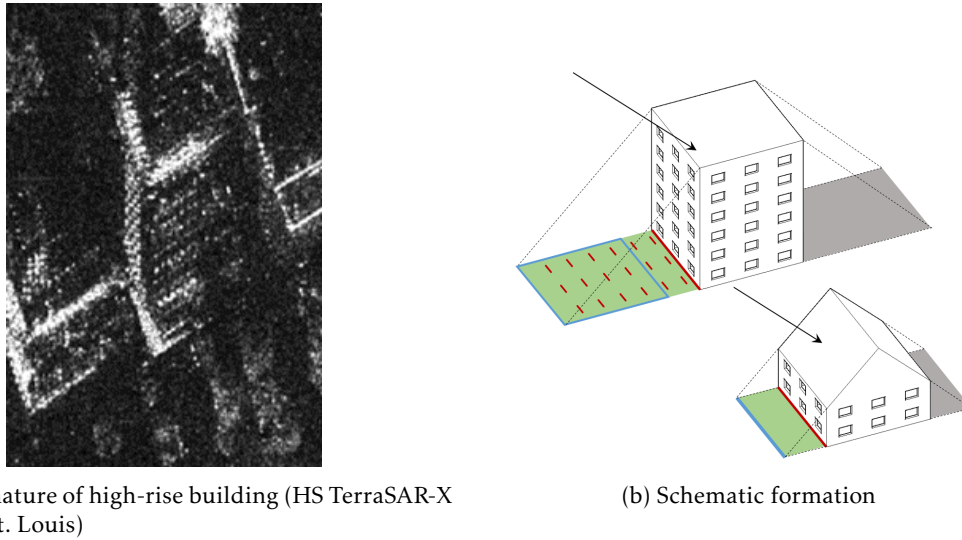
(b) Schematic formation

Figure 3.1.: Basic signature characteristics of building.

specific damage types occur only sporadically, and acquisitions are rarely recorded from more than one look angle. Since a signature analysis, though, depends on a large amount of acquisitions, the requirement most often cannot be met with real imagery. Furthermore, the signature oftentimes is not clearly distinguishable, since neighbouring objects, in most cases other buildings, interact/overlay with the signature in question and thus complicate interpretation. The use of a simulation environment offers significant advantages for this concept: absolute control about the building, its damage, and its surroundings; observability from arbitrary angles; and the capability to change sensor parameters at will.

Deciding for this approach, the first step is the generation of a sufficient number of simulations for the building damage types described in the previous section. For this step, the coherent ray-tracing SAR simulation suite CohRaS was used, which was introduced in Section 2.3. The input 3d models were created following the example of the descriptions of damages listed in Table 3.2, also including a model of the corresponding intact building. Regarding backscattering properties, it was differentiated between material for building, ground, glass and debris, where glass was provided with very specular properties, and building and ground were modelled to be less specular but with moderate direct reflectance. The backscattering properties were chosen such, that the amplitudes of real signatures showing a comparable intact building are imitated. In order to simulate signatures comparable to those of TerraSAR-X images in HS mode, corresponding sensor and imaging parameters were used. For a list of the relevant parameters used for the simulation, see Table 3.3, with the computing parameters introduced in Section 2.3. Each model was simulated for a full range of aspect angles from 0° to 359° in steps of 1°, so that the dependence of the signatures on this angle could be investigated.

In the following, each damage type is discussed individually regarding the change of signature in comparison to the intact building. When modelling these damage types it was of importance that the 3d models remained

Table 3.3.: Sensor and imaging parameters used for the simulation.

Sensor parameters[*]	Wavelength	3.1 cm
	Pixel spacing azimuth	87 cm
	Pixel spacing range	45 cm
Computing parameters	Maximum number of bounces	5
	Number of point scatterers	6
Acquisition parameters	Incidence angle	32°
	Aspect angle	360° in 1 degree steps

[*]TerraSAR-X HS mode

(a) 3d model of intact building

(b) Simulation with reflective glass

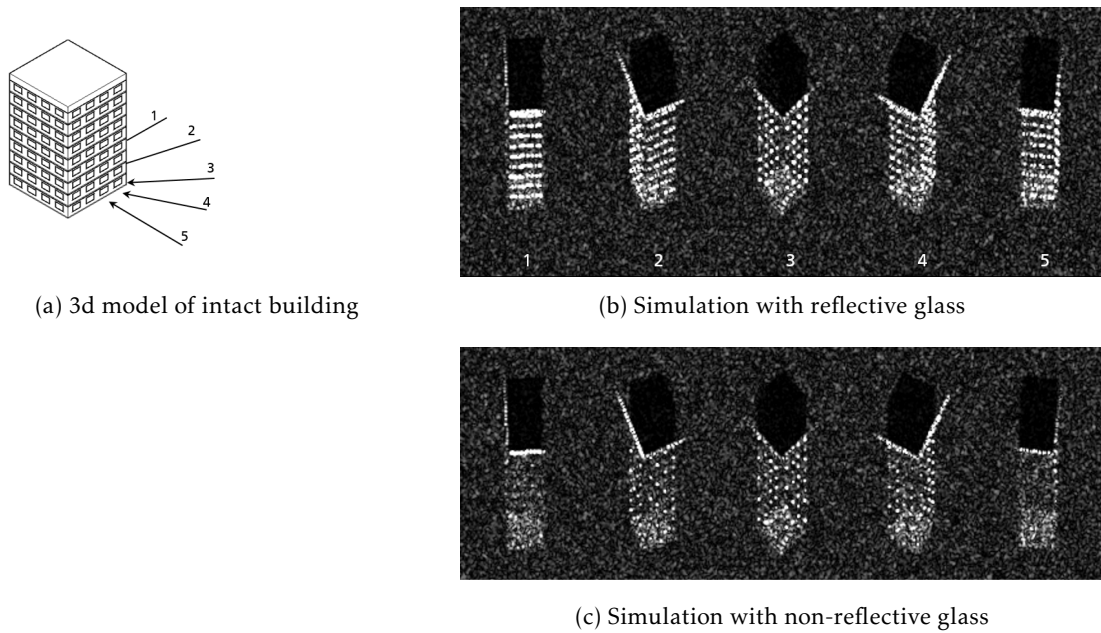(c) Simulation with non-reflective glass

Figure 3.2.: 3d model and simulated signature of intact building.

generic but at the same time were clearly distinguishable from one another. A differentiation of some of the types on the basis of their SAR signature is highly unlikely, which lead to the conclusion that some of the defined damage types are to be merged or disregarded altogether. Furthermore, characteristic signatures of still standing structures are in most cases at least partly covered by signatures of the heaps of debris surrounding the building. In order to record these characteristics and to also create a signature of the respective damage type which is as realistic as possible, some damage types are simulated with surrounding debris and without it.

Intact building

Figure 3.2(a) shows a 3d model of an intact high-rise building that is used as basis for the destruction types discussed in the following. Even though generalised, details such as the window ledges, which are important for a realistic simulation of the essential signatures, are included in the model. It consists of 9 stories, is flat-roofed and features a square footprint with a width of 16 m and a height of about 27 m. The five directions indicate aspect angles that were used for the simulation of the SAR amplitude images shown in Figure 3.2(b). The main building signatures, which were addressed both in appearance and formation in Figure 3.1, are visible in the simulated signatures. These signatures show a pattern of very strong backscattering from window ledges, as a result of the formation of dihedral and trihedral corner reflectors with the glass. It is presumed, that since glass is one of the weakest points of a building and thus the first to burst in a destructive event, any of the damage types in question are severe enough to warrant a destruction of all the glass. Because removing the glass yields a great deal of multi-bounces inside the unrealistically empty interior of the building, the glass was instead given a non-reflective material. The thus induced reduction of intensity is visible in Figure 3.2(c), where the simulations for non-reflective glass are depicted in comparison to the simulations for specularly reflective glass in Figure 3.2(b). A pattern of points prevails even for non-reflective (broken) glass with reduced intensities, due to the window recesses themselves forming dihedral corners. This is also comparable to installed window frames or similar fittings, where also small trihedral corners tend to occur.

For an entire 90° inspection of these intensity changes, some distinct variation can be observed. Figure 3.3 shows the course of maximal values throughout these 90° for the simulations with specular glass and the simulations with non-reflective glass. Any maximal or mean values are obtained from a fixed cut-out of the
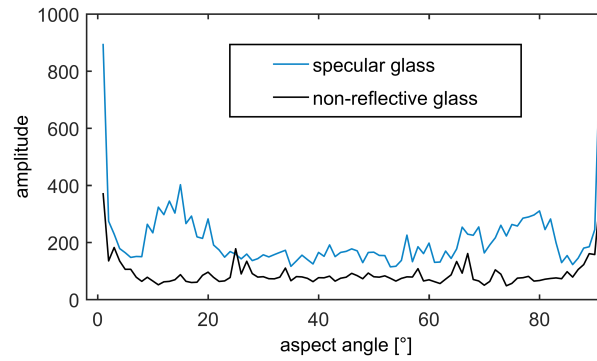
Figure 3.3.: Impact of glass reflectivity on building signature.

amplitude images that contains the entire building signature including shadow. The dihedral corner lines turn out to be of considerably lower intensity without the reflective glass. This best can be seen for frontal viewing angles (e.g. 0°, 90°). For aspect angles between 9° and 22° (68°-81°) the window ledges yield the strongest trihedral corner reflection in the case of specular glass, for non-reflective glass there are only much weaker dihedral corner signatures. Since the glass-induced strong reflectance is no damage type specific feature, the following comparisons to the damage types are made regarding the simulated intact building with non-reflecting glass.

Type 1: Inclined plane

The first damage type to be addressed is defined by an inclination regarding the roof area, which can occur for a partial one-sided collapse of walls. Figure 3.4 illustrates this type of damage for the introduced 3d building model. Even though the damage to the building is profound, in terms of schematic signature change, there is only a slight alteration to the signature formation. Since these changes are best visible for frontal viewing angles, the SAR signatures show the simulations for those aspect angles. The change is most obvious in the projection of the roof area, which, depending on the inclination angle, shows distinct distortions. Also, direct reflection is affected by whether the roof is sloped towards the sensor or away from it, resulting in a respective increase or decrease of intensities.

Types 2 and 3: Multilayer collapse

A multilayer collapse covers both, inward and outward collapses of multiple stories. In particular this type of building damage can feature quite varying traits that can not be covered with just a few models. Instead, one exemplary case is presented of an outward multilayer collapse, causing interesting SAR signatures. Figure 3.5(a) shows this damage type as 3d model and corresponding simulated signatures. Even though real life damage does not develop this accurately, the presented signature characteristics are expected to show nonetheless, though diminished in specificity. Due to the height reduction and the outward expansion, the shadow and the layover area are considerably changed. Depending on the aspect angle, there is strong dihedral corner reflectance, caused by the almost parallel displacement of the different layers. The severity of this damage type implicates substantial amount of debris surrounding the building area, and with it a significant alteration of signatures. Figure 3.5(b) shows these signatures, as they would more likely appear in reality. The heaps of debris cause strong backscattering, however, due to the damage severity, the type specific signatures are still recognisable.
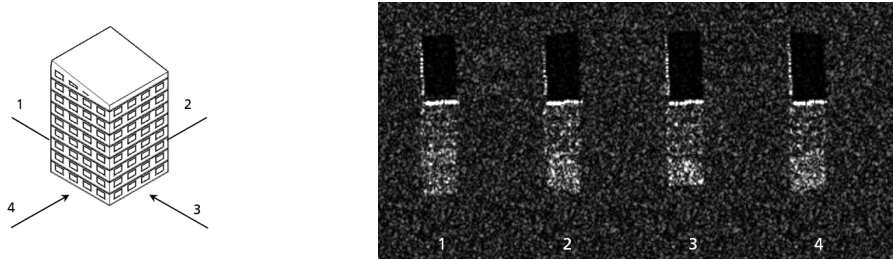
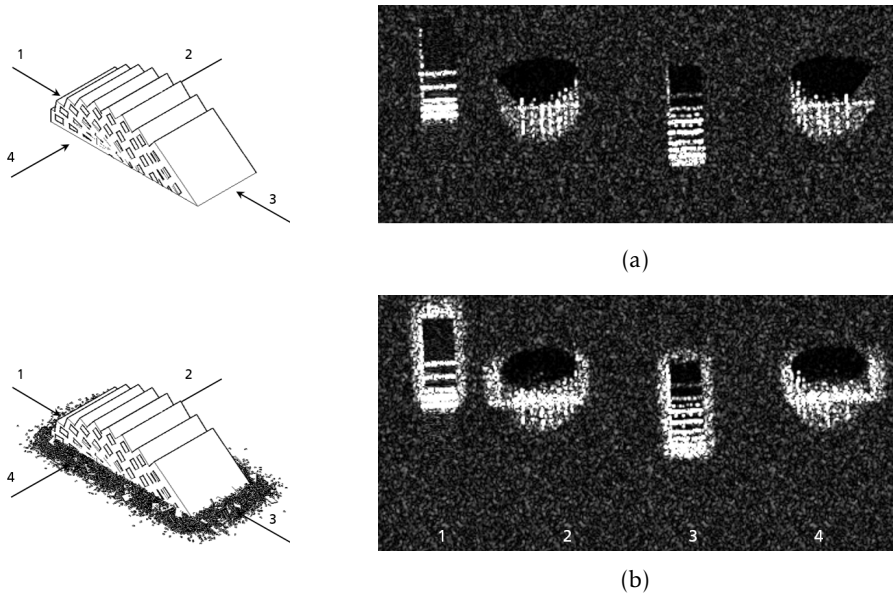Figure 3.4.: Building damage type: Inclined plane.

(a)

(b)

Figure 3.5.: Building damage type: Outspread multi layer collapse; a) without debris and b) with debris.
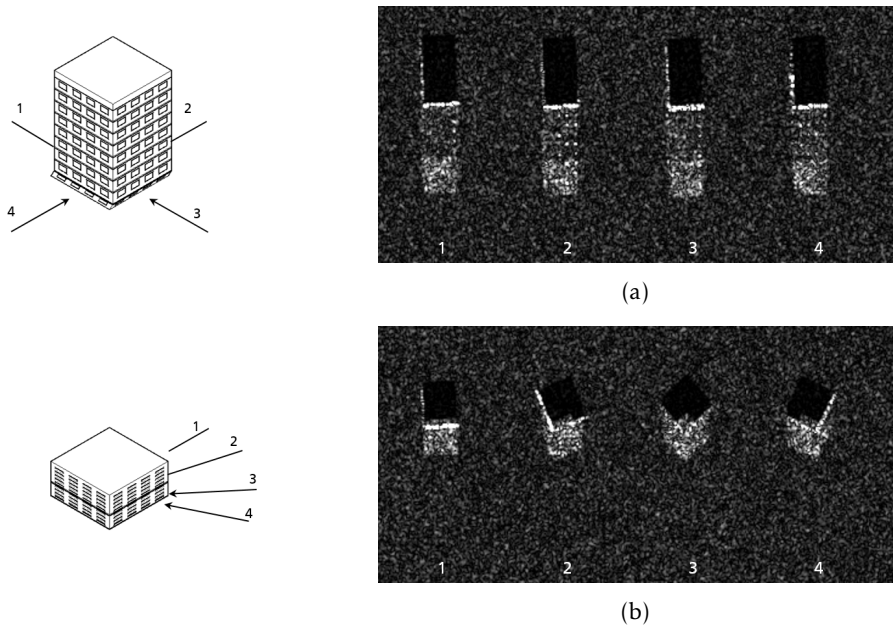

(a)

(b)

Figure 3.6.: Building damage type: Pancake collapse; a) first floor and b) all stories.

Types 4 and 5: Pancake collapse

The damage types regarding pancake collapses differentiate not only between the collapse of single or multiple stories but also between the actual story levels that are affected. Since it is very unlikely that the SAR signatures can reflect these differences, the damage types were combined for this analysis. The two examples presented for a pancake collapse are depicted in Figures 3.6(a) and 3.6(b). First, the collapse of the first floor shows a downward shift of all of the building above as well as some shift to the side. Compared to the rest of the introduced damage types this is a rather inconspicuous damage in terms of structural change. Even though, depending on the aspect angle, the sideward shift of the building causes a measurable shift of the building corner signature towards (or away from) the sensor. Regarding the downward shift, the second example shows the corresponding traits more clearly. The pancake collapse of all of the stories yields a severe height reduction, which in the SAR signature shows with a corresponding reduction of the shadow and layover areas and a shift of the roof area closer to the building footprint. Also the intensity of the building corner is reduced measurably. This is of course directly dependent on the number of stories affected by the collapse or rather the height reduction that is caused.

Types 6 and 7: Heaps of debris

The most severe type of damage is the total collapse of the building resulting in a large heap of debris. This is further subdivided into categories, which describe types of debris that can yield quite different SAR signatures and thus turn out to be very interesting for this survey. A standard heap of debris, consisting of small-scale bricks of different sizes and shapes, is introduced in Figure 3.7(a). The corresponding SAR signature displays a noticeable texture, which is quite consistent throughout the images. In Figure 3.7(b) a heap of debris including large planes is shown, representing larger structural parts that did not fall to pieces. The SAR signature is distinctly lower in intensity, due to fewer small-scale dihedral and trihedral corners forming and as a result of occurring shadow areas. Next, the case of vertical elements within the heap of debris, brought forth by still standing parts of walls, is introduced in Figure 3.7(c). For a clarification of which specific signatures are caused by the vertical elements, this damage type is additionally presented without the surrounding heap of debris. Thus, the dihedral corner lines and the trihedral corner points that are a result of the unroofed interior structure are much more noticeable. Including the heap of debris, this signature is reduced in intensity quite a bit due to the lack of the perpendicular plane regarding the vertical elements. Lastly, the damage type that is defined as heap of debris on uncollapsed stories is also included in this subsection, since it shows the same effect but at a certain height. As Figure 3.7(d) demonstrates, the debris covering the building top results in the distinct texture of debris, projected corresponding to the height of the remaining building.

Types 8 and 9: Inclination and overturn collapse

The defined damage type describing an overturn collapse of the building was combined with the case of a building inclination, caused by a one-sided subsidence, since technically it is the case of an utmost inclination of the building, yielding a corresponding SAR signature. Figure 3.8 shows the case of a building inclination of 15° with and without debris. Aspect angles 1 and 3, where the building leans away or towards the sensor, respectively, point out several traits. For one, a broadening of the area that used to be the building corner is observable, which is due to the fact that the multi-bounce reflections of building wall and ground no longer cover the same path length. Furthermore, as was the case for the damage type in Figure 3.4, the sloped roof results in a reduction or increase of direct reflection. Meanwhile, for aspect angles 2 and 4 the building inclination is visible directly and the building corner is preserved, however stretched lengthwise, due to the new range extent. Adding debris to the model causes the main characteristics at the base of the building to be overlaid by the strong texture of debris.
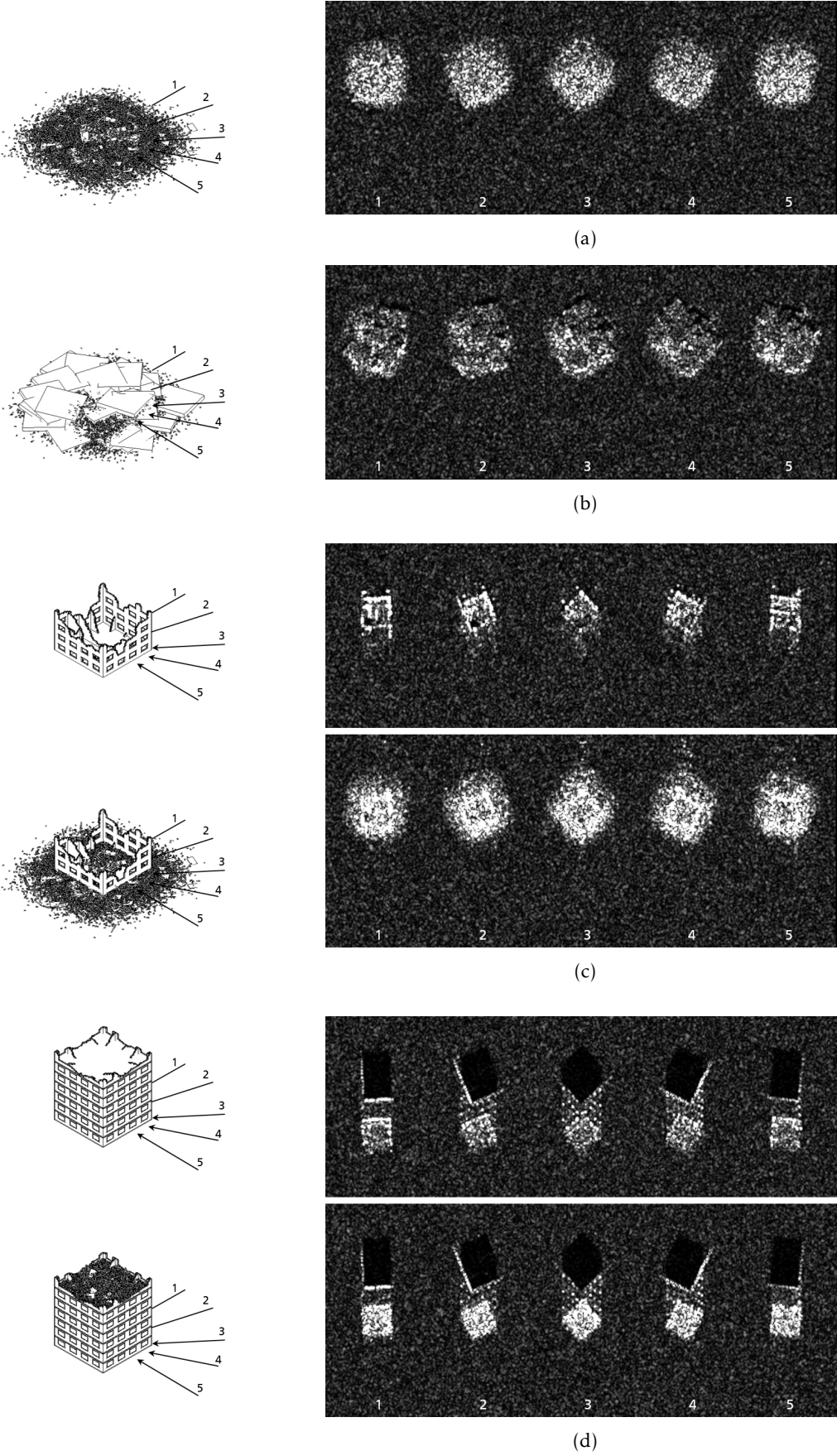
Figure 3.7.: Building damage type: Debris; a) heap of debris, b) heap of debris with planes, c) vertical elements without and with debris, and d) uncollapsed stories without and with debris.
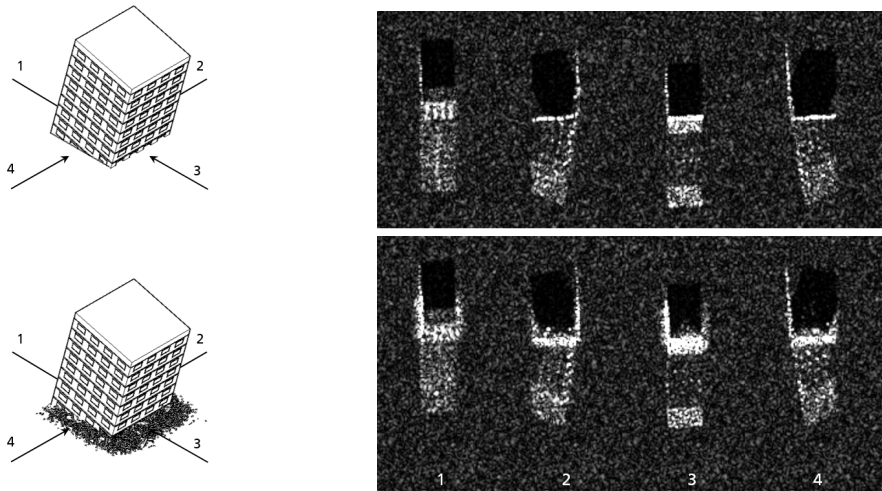
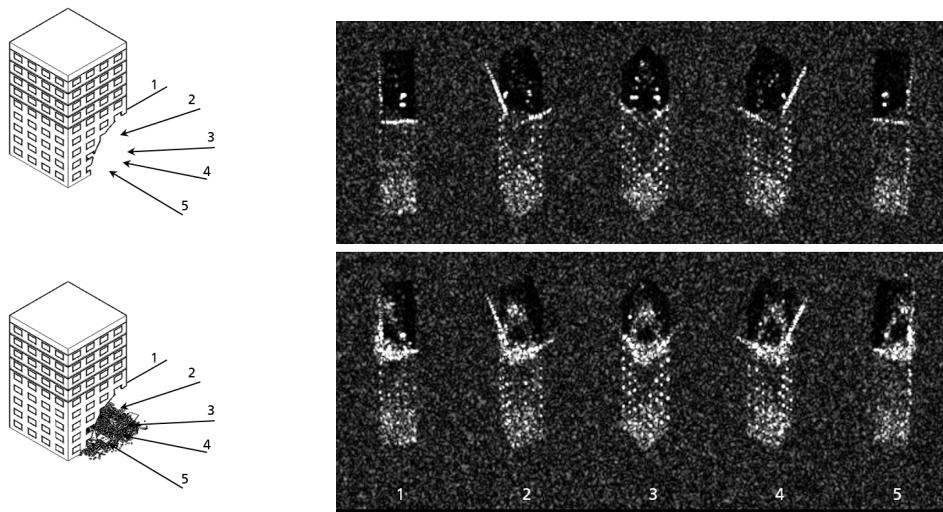Figure 3.8.: Building damage type: Inclination (without and with debris).

Figure 3.9.: Building damage type: Overhanging elements (without and with debris).

Type 10: Overhanging elements

As the last damage type to be addressed, Type 10 is defined as collapse of walls at the base of the building or possibly at intermediate stories, resulting in overhanging elements. Figure 3.9 shows a corresponding model with the damage at its base and its simulated signatures. Most noticeable in the SAR signatures are the reflections of the building interior, since they lie in the otherwise not illuminated shadow area. The specific interior reflections, however, are only of limited approximation to reality, since the interior of the building was not modelled with this priority. Additional debris below the overhanging elements, thus, shows a much more realistic outcome.

3.3. Discussion on signature characteristics and prospects

The previous section provided a survey about the theoretical SAR characteristics of commonly occurring building damage types. If and how the thus gained information can be exploited for the purpose of a damage detection is the focus of this section.

(b) TerraSAR-X scene of city

(a) Detail of a LoD2.5 3d city model
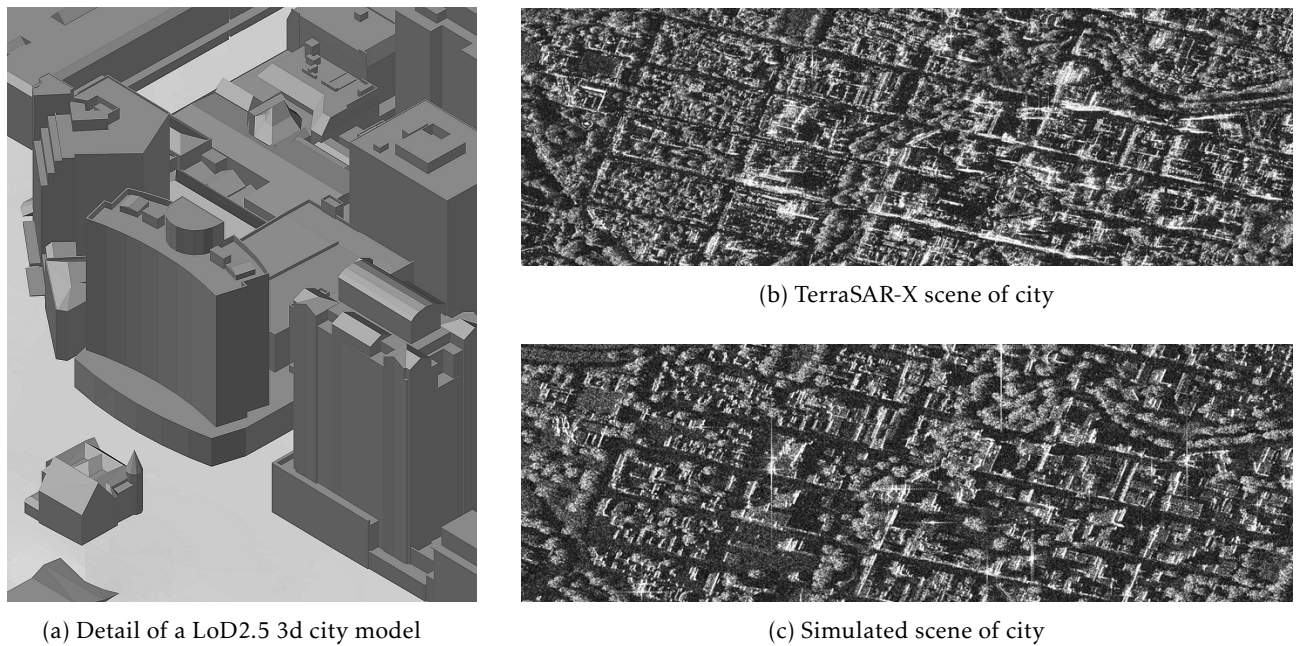
(c) Simulated scene of city

Figure 3.10.: Prospect of exchanging pre-event image with a simulation by use of a 3d city model.

The simulation based signature analysis showed that for most damage types the structural change of signature is observable quite well. This is the case for the comparison of the intact building with the damaged building with as well as without the surrounding heaps of debris. Hence the prospect of a detailed change detection approach in a real pre- and post-event image scenario is rather promising, given limited changes caused by other sources such as e.g. vegetation or vehicles. However, HR pre-event imagery often times is not available, since usually only specific areas, which e.g. stand at risk of some natural phenomenon are monitored. If in such a case pre-event information in form of a 3d city model is at hand, a SAR image of the scene can be simulated and then may function as a substitute for the missing pre-event image. As discussed in Section 3.2 a minimum level of detail (LoD) is required in order for the essential building signatures to be simulated correctly. For the concept of 3d city modelling several standards are commonly in use. Regarding the CityGML standard described in [26] the simulation requirements are met positively for a LoD3 model, which includes detailed roof structures and also openings for windows and doors. For most cases, though, a LoD2.5 model or even a LoD2 model would suffice, where roof structures are more generalised and window and door openings are not accounted for, as shown in an exemplary model in Figure 3.10(a).

Figures 3.10(b) and 3.10(c) show an exemplary scenario, with a post-event TerraSAR-X image and the correspondingly simulated pre-event image, where also vegetation and additional geographical data are taken into account. Since the availability of accurate 3d city models has improved drastically over the last years, the prospect of using this information to generate pre-event imagery also shows potential. However, without any pre-event data about the signature of the intact building, the task of damage detection is much more challenging. It quickly becomes clear, that based only on the texture of a post-event amplitude image, the damage type specific signatures do not provide enough characteristics for a categorised damage detection. Instead, the most prominent texture of the damaged buildings is caused by the heap of debris surrounding the area. Heaps of debris are certain to occur for every major damage type and thus are a reliable element of a damage site. So, this approach disregards the notion of categorising damage types and instead focuses primarily on the detection of the signature of heaps of debris with the aim of a reliable detection algorithm of buildings with major damages.

Chapter 4.

Analysis of the SAR amplitude signature of debris

As was discussed in Section 3.3, the most prominent aspect regarding the SAR signature of a damaged building is the texture of debris. Also, the prospect of using synthetically generated debris texture for the purpose of signature analysis and damage detection instead of using samples from real imagery was introduced. Since the use as training samples involves simulations covering the wide range of potential real debris occurrences, an understanding regarding their nature and characteristics is called for. This includes facts on potential building construction types, involved materials, the cause of damage and composition characteristics, so that the geometric debris surface as well as radiometric backscattering properties subsequently can be assessed and imitated. The process of generating accurate signatures of debris relies on precise input material, which most importantly includes realistic 3d modelling and an adequate imitation of backscattering characteristics for all materials involved. Using synthetically generated signatures provides additional advantages, since it allows for an analysis regarding systematically changing input instances, be it the input geometry or the input backscattering properties. Such investigations can aid in the understanding of the resulting signature and support setting margins to possible texture peculiarities.

The aim of debris detection by means of its SAR texture also entails the challenge of dealing with textures of a similar nature. Even though the signature of debris is rather prominent, there prove to be surfaces that produce a SAR texture of comparable characteristics. In order to be able to account for them in the debris detection algorithm, these surfaces require further looking into.

The chapter is organised as follows: Section 4.1 gives a short overview of real heaps of debris and their signature in SAR imagery, in Section 4.2 the process of generating accurate SAR signatures is described, and in Section 4.3 specific cases of textural similarity are introduced.

4.1. Properties of heaps of debris

Heaps of debris, in terms of a building collapse, mainly occur due to natural disasters, including earthquakes, floodings, tsunamis, and hurricanes as well as controlled blastings or as a result of bombing raids. The nature of debris varies distinctly depending on the type of disaster that has occurred. Earthquake caused building collapses for example predominantly result in a locally restricted heap of debris, where building floors collapse on top of each other and thus enclose other kinds of waste inside, whereas for hurricanes, floods and tsunamis the debris is more widespread and also mixed with vegetational and other waste. Meanwhile, debris caused by bombings often is burnt and thus materials solely consist of concrete, brick and stone. A more detailed description of the specific debris characteristics regarding these disaster types can be found in [39].

The cause for destruction, however, is contemplated to play but a secondary role regarding its impact on the characteristics the heap of debris takes on and thus on the resulting SAR signature. The mix of different building materials is considered to have the essential influence, and that theoretically can vary greatly. Construction types typically used in industrialised countries were discussed in Chapter 3 and amount to concrete structures, masonry, steel buildings, and timber structures. As a consequence, heaps of debris in these regions consist mainly of the materials concrete, stone, structural steel, and timber with numerous additional materials used for construction such as plastics, insulation materials and so on. Heap sizes vary depending
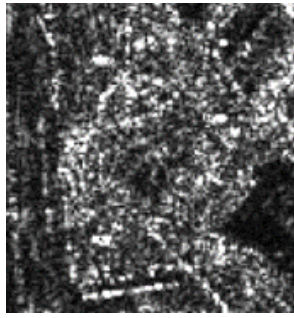
Figure 4.1.: Exemplary SAR signature of heap of debris.

on the destruction type and the building size, which can span up to several hundreds of square metres. However, most occurrences are distinctly smaller. Figure 4.1 shows an exemplary debris signature in a TerraSAR-X amplitude image, caused by a controlled collapse of a building located in Munich, Germany. It is considered worth mentioning that due to SAR being based on a distance measurement, heaps of debris located not on ground level but on an intermediate floor are shifted in range direction towards near range depending on the floor height. Also, they are frequently overlaid by signatures of neighbouring high objects, making the extraction of the signature challenging and thus prompting the usage of synthetically generated signatures.

4.2. Process of generating accurate SAR signatures of debris

In the following, the different factors influencing the quality of debris simulations are discussed one by one. This includes the generation of realistic 3d models, the specification of material backscattering properties regarding multiple materials, and the setting of simulation parameters.

4.2.1. 3d modelling of heaps of debris

The analysis on heaps of debris, that was discussed in Section 4.1, revealed typical composition characteristics. Aside from the aspect of material backscattering properties, the geometric surface of the heaps is decisive for the SAR signature. This refers to the more or less randomly oriented objects (mostly bricks) provoking multi-bounce backscattering. Given a wavelength in the centimetre range, the relevance for shapes of a scale smaller than a few centimetres is but minor, whereas the roughness in the scale of decimetres has great impact on the SAR signature. For the purpose of describing this decimetre roughness, the term *macroscopic surface roughness* is introduced here, as opposed to the roughness concerning material backscattering properties in millimetre range. Figure 4.2 visualises schematically the changing backscattering mechanism for a decreasing macroscopic surface roughness.

The aim of the modelling process is to imitate the macroscopic surface roughness present in real heaps of debris, which is mainly caused by bricks, beams, wall sections and similar forms. Since heaps of debris usually are very chaotic structures that cannot be totally accounted for in 3d modelling, the synthetic heaps used in this study are reduced to these essential elements. The use of various randomly piled up cuboids of different form, size and orientation is considered to be sufficient, since the use of more complex forms does not provide
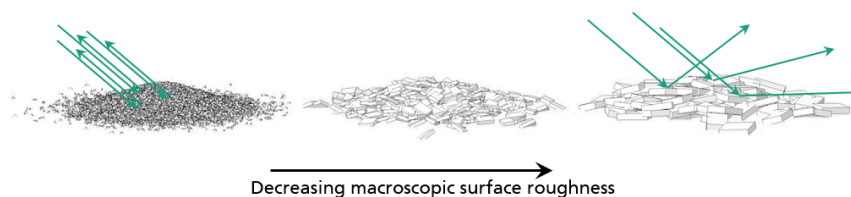

Decreasing macroscopic surface roughness

Figure 4.2.: Schematic backscattering mechanism for heaps of debris with decreasing macroscopic surface roughness.
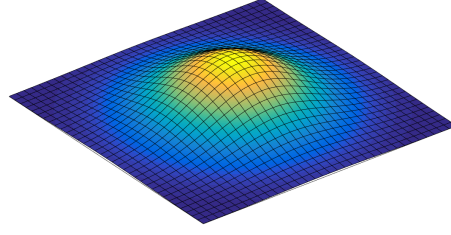
Figure 4.3.: Model surface hull described by two-dimensional Gaussian function.

additional accuracy regarding the random occurrence of corner reflectors nor the face orientation. By a variation of the cuboid parameters the surface of the model can be varied, thus covering a large range of possible types of debris. A stepwise alteration further produces a controlled change of the macroscopic surface roughness, which is of importance for the understanding of its effect on the SAR signature. The manual handling of the modelling process comes along with great expense. Hence, the process is automated, thus making the use of a large variation of models feasible.

Automatic model generation   A heap of debris features typical characteristics regarding its form as a whole. On these grounds it is assumed that the hull of a generalised heap of debris is best fitted by a bell shape, which for reasons of convenience has symmetric spreads in both horizontal directions. Thus, the hull is defined by a symmetric two-dimensional Gaussian function as follows

$$h = h_{max} \cdot e^{-(\frac{x^2}{2\sigma^2} + \frac{y^2}{2\sigma^2})} \tag{4.1}$$

where h_{max} denotes the maximum height of the model and σ the standard deviation. The horizontal radius r of the model is defined here as the width corresponding to the 99%-quantile $z_{0.99} = 2.576$ of the curve. Hence, the standard deviation is $\sigma = \frac{r}{z_{0.99}}$. The thus generated surface hull (depicted in Figure 4.3) is the basis for the following modelling steps.

In a first step, types of cuboids are defined, specifying width, length, height, number of entities per area and the range of orientation. The range of orientation is included to prevent large cuboids (wall sections) to stick in unrealistic angles, thus causing strong uncommon signatures. For every type of cuboid a 3d cluster (Gaussian distributed coordinates) is then generated with the hull defining the maximum height at each position. Figure 4.4(a) shows such a cluster. Since the polygon count for this method of modelling reaches a high level, which involves a high computational cost, a fixed thickness is defined for the debris layer underneath which the heap is hollow, meaning the cluster points are dropped. Figure 4.4(b) visualises this by means of a slice plane of the cluster. In order to prevent strange effects caused by multi-bounce reflections inside this hollow model, care has to be taken, that the layer thickness and the number of entities is set high enough.   For every cluster point coordinate (x_i, y_i, z_i) a cuboid of the specified dimensions is generated with its centre at (x_i, y_i, z_i). Subsequently, it is randomly oriented in the coordinate space. To prevent unrealistic scenarios, the rotation around the x- and y-axis is restricted to angles in the range of orientations, specified in the cuboid type specifications. After generating the heaps for every type of cuboid the combined model is exported as a CAD file. By tagging the cuboid type information in the layer structure of the CAD file, the assignment of different materials is enabled for the subsequent simulation process.


(a)   (b)

Figure 4.4.: Cluster of cuboid centre points of a) whole model b) slice plane of model, showing layer thickness.

Table 4.1.: Specifics on 3d models of heaps of debris: *Models T-1* to *T-6*.

	Description	Sizes [cm]	Range of rotation [degrees]	Number per m^3
Model T-1	Brick	15x20x40	360	13
	Bar	10x10x400	50	0.6
	Concrete slab	30x300x400	45	0.13
Model T-2	Brick	25x30x60	360	10
	Bar	10x10x400	50	0.6
	Concrete slab	30x200x300	45	0.13
Model T-3	Brick	10x30x40	75	13
	Beam	15x20x400	90	0.6
Model T-4	Pillar	50x50x80	360	1.3
	Beam	10x30x400	70	0.5
	Brick	15x20x30	360	10
Model T-5	Brick	15x20x40	360	13
	Bar	10x10x400	80	0.32
	Concrete slab	20x300x500	30	0.06
Model T-6	Brick	20x30x50	360	6.4
	Concrete slab	10x150x250	50	1
	Concrete slab	30x450x500	40	0.06

Table 4.2.: Components of Model sets M1 and M2, showing decreasing macroscopic surface roughness.

	Model set M1	**Model set M2**
No 1		
...		
No 10		
...		
No 20		
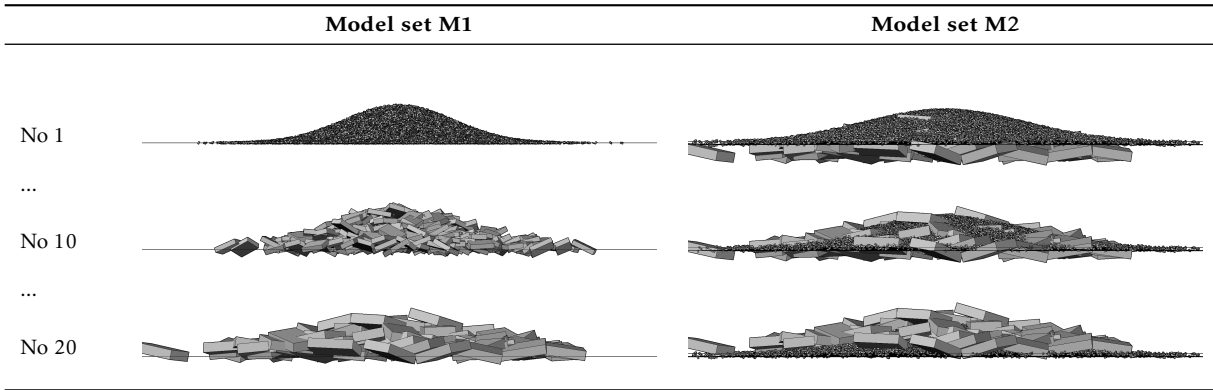
The algorithm used to generate the heaps leads to the occurrence of numerous intersections between the cuboids as well as between the cuboids and the ground. This method of modelling neither prevents intersections among the cuboids nor intersections of cuboids with the ground. However, this bears no conflict with a realistic surface, which exclusively is accountable for the resulting signatures. Also, theoretically it is possible that a cuboid is in no contact to ground or other cuboids, thus hovering above ground. This however, is rather unlikely, since by any means the cluster density is required to be rather high.

In the following, two series of 3d models are introduced that are employed for different aspects: firstly the prospect of generating training data for a classification task described in Section 5.2.1 (*Model set T*); and secondly the prospect of exploring the effect of the macroscopic surface roughness on the SAR signature, discussed in Section 5.3.1 (*Model set M*) .

Model set T   For the purpose of simulating training data, a set of 3d models is required that features different surface types, thus covering the wide range of debris variations found in real conditions. Accordingly, a fixed set of models is generated, which vary in their composition of cuboid types and their macroscopic surface roughness. Their surface hulls, however, feature matching dimensions (15 m radius, 4 m maximum height, and 1 m layer thickness). For analytical reasons the radius r was chosen such, that the generated spatial extent of the signature is large enough to contain several windows of sizes up to 15x15 pixels. In most cases actual heaps of debris have a much smaller footprint, in particular when buildings sustain merely a partial damage. However, for the prospect of texture extraction this is considered non-relevant.

In the following, a set of six models is introduced, which is referred to as *Model set T*. They are used for the generation of signature classes for the prospect of texture classification in Chapter 5 and are designed such, that the variations of common surface types are represented. Accordingly, each model shows a varying occurrence of the main debris components, consisting of bricks, bars, beams, and slabs. In Table 4.1 the model set is visualised and specifics are listed regarding the compositions of cuboids, along with their size, frequency of occurrence and maximal range of vertical rotation.

Model set M   In order to assess the impact of the macroscopic surface roughness on the signature of debris a uniformly changing surface roughness is required. The assumption is, that (for X band) a compilation of small bricks (20 cm edge length) qualifies for a very rough surface, and a composition of cuboids with large-scale flat planes (edge length 5 m) represents a heap of debris with a rather smooth surface (with the actual dimensions depending on the wavelength in question). A stepwise alteration between these two model conditions can be realised in several ways, of which two approaches are contemplated here. A first set of 3d models, referred to as *Model set M1*, is realised by the stepwise alteration of the cuboid dimensions and a simultaneous reduction of the cluster density. A second set of models, referred to as *Model set M2*, is designed such that a heap of small
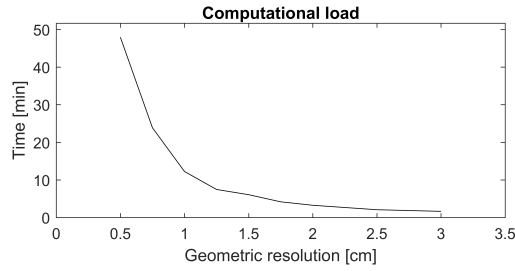
Figure 4.5.: Influence of geometric resolution on computation time.

bricks is gradually exchanged by a subjacent heap of large cuboids, which is raised vertically to the surface. Both sets consist of 20 models (radii of 25 to 35 metres) of decreasing macroscopic surface roughness, with Table 4.2 visualising three exemplary stages each. Since the range of surface roughnesses is the same for both sets, it is refrained from introducing any profile roughness parameter.

4.2.2. Simulation parameter settings

A SAR signature is influenced by multiple factors, first and foremost by specifications regarding sensor, acquisition and processing. Consequently, for simulated SAR signatures to be comparable to reference signatures, real parameters need to be imitated. The necessary simulation parameters were described in Section 2.3.1 in detail. Some parameter settings, including *Pixel Spacing* and *Wavelength*, are copied from respective sensor specifications, others need to be set as a trade-off between accuracy and computational cost.

The parameter *Number of Bounces* can be computationally costly if set too high, since every ray is traced for up to that number of bounces between surfaces. Testing showed that a limit of 5 bounces covers the prevalent multi-bounce signatures, while being computationally feasible. For rare peculiar signatures (predominantly occurring in man made objects) this number may be too low; for the simulation of regular debris, however, it is adequate.

The *Geometric Resolution*, describing the voxel size, which the model scene is divided into for ray tracing, is a main factor regarding the computational load. The direct influence on the computation time concerning a simulation of debris is plotted in Figure 4.5. The corresponding simulations were executed on a standard desktop computer equipped with an Intel[R] Core[TM] i7-6700 CPU @ 3.40GHz processor (4 cores), 64-bit architecture, using a Windows 10 operating system. For this test, a model of medium complexity (approximately 300.000 polygons) was used. The plot shows that for the conditions at hand the simulation is computationally reasonable for a *Geometric Resolution* down to about 1.5 to 1 centimetres. Further, the recommendation to use no less than half the wavelength (established in Section 2.3.1) also suggests a value of 1.5 centimetres. The corresponding computation time amounts to approximately 6 minutes per simulation, however, due to the widely differing polygon count amongst the 3d models used in this study, this is but an average value. Table 4.3 lists sensor and processing parameters with settings that imitate a TerraSAR-X image in HS mode.

Table 4.3.: Sensor and processing parameters.

Sensor parameters (TerraSAR-X HS mode)	
Wavelength [cm]	3.1
Pixel Spacing [cm]	45.5 (Range) 85.7 (Azimuth)
Computation and processing parameters	
Geometric Resolution [cm]	1.5
Windowing	Hamming
Number of Point Scatterers	6
Number of Bounces	5

(a) Influence of maximal backscatter coefficient σ_0

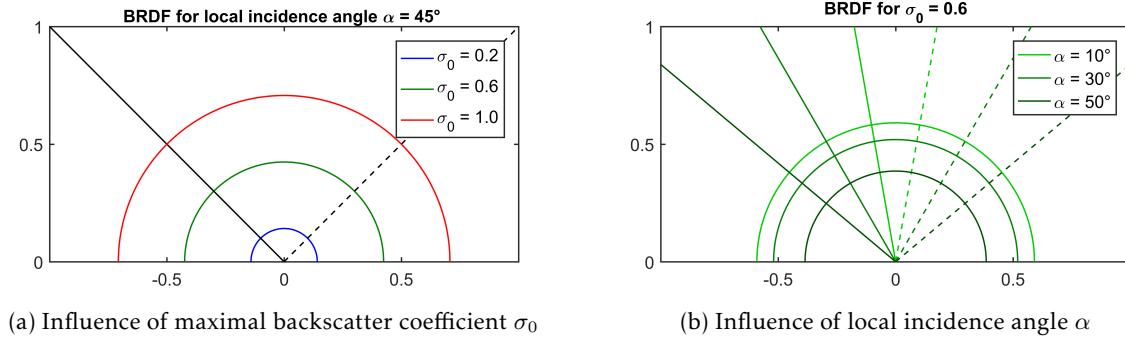(b) Influence of local incidence angle α

Figure 4.6.: BRDF of diffuse scattering model.

Also, the backscattered intensities are substantially influenced by acquisition parameters. In particular the dependence on the incidence angle has been focus of investigations in many fields of interest, e.g. sea ice [53] or vegetation [83].

4.2.3. Adjustment of radiometric backscattering characteristics

The modelling process of the scattering mechanisms and the resulting backscattering intensities are handled by the simulator as described in Section 2.3.2. Finding appropriate parameter settings for the different kinds of materials requires understanding of the settable parameters, as well as a process of recursive tuning in combination with suitable reference signatures. In the following, an insight is given as to how the changing of individual material parameters affects the backscatter intensities. Subsequently, the process of extracting backscatter properties is described for several materials using reference signatures obtained from real SAR imagery.

Parameter influence on scattering model

The backscattering model is tunable by means of the five material parameters σ_0, σ_{max}, x, y and d. How and to what extent these parameters influence the distribution of the reflected signal is demonstrated by means of the bidirectional reflectance distribution function (BRDF). Diffuse scattering is modelled as a function of the parameter σ_0 (maximal diffuse backscattering coefficient) and the local incidence angle α (equation 2.45). The impact of a parameter change on the backscattering distribution is exemplified in Figure 4.6(a) by the BRDF for three exemplary values of σ_0 and a local incidence angle $\alpha = 45°$. As is typical for the visualisation of BRDFs the incoming ray is plotted using a continuous line, whereas the theoretical specular reflection is plotted using a dashed line. Figure 4.6(b) points out the difference in scattered intensities for different local incidence angles while maintaining a fixed σ_0. Including specular reflections in the model, which is specified by equation 2.46, involves shaping the specular reflectance lobe by means of the parameters σ_{max}, x, y, and d. Figure 4.7(a) points out the influence of parameter σ_{max}, namely the maximal specularly reflected energy, on the reflectance lobe of the BRDF by means of three exemplary settings. Meanwhile, the breadth of the lobe is controlled by parameter y, as exemplified for three settings in Figure 4.7(b). To what extent the specularly reflected energy is influenced by the local incidence angle α, is regulated by parameter $x \in [0, 1]$. This context is demonstrated in Figure 4.8, showing BRDFs for three different local incidence angles with the effect of a reduced specular reflection for flat local incidence angles. And finally, with parameter $d \in [0, 1]$ there is an option to apply a straightforward dampening factor to the specular reflection, which can e.g. be used to simulate materials that absorb a part of the incoming energy.
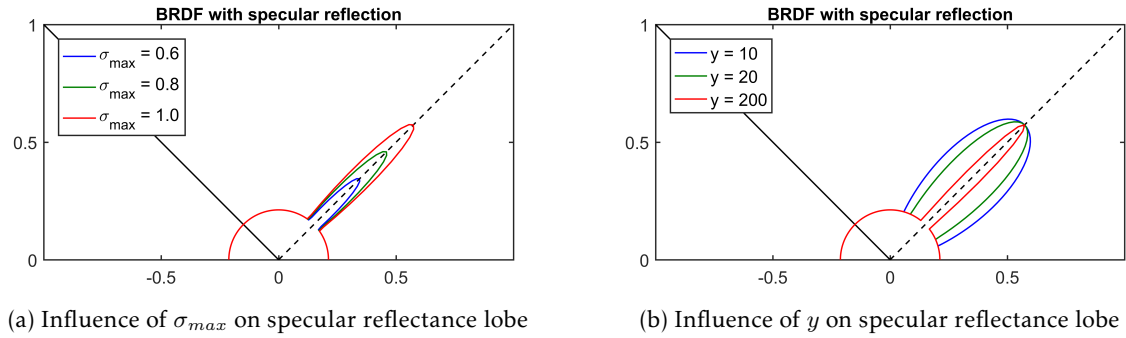
(a) Influence of σ_{max} on specular reflectance lobe

(b) Influence of y on specular reflectance lobe

Figure 4.7.: BRDF of scattering mode with specular reflectance lobe.

(a)   (b)   (c)
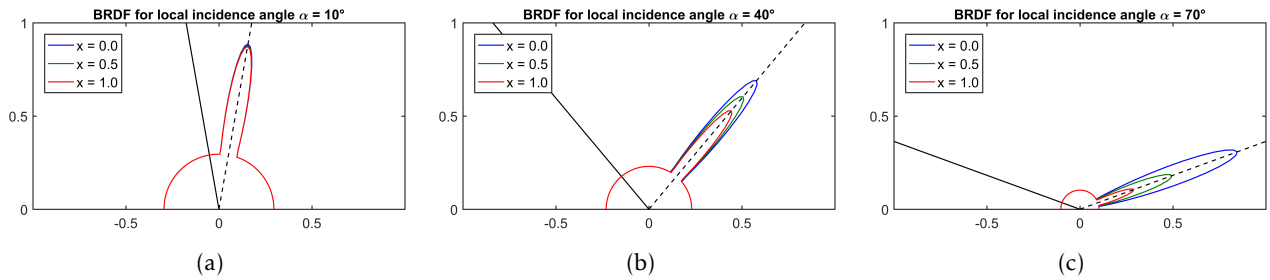
Figure 4.8.: Influence of x on specular reflectance (BRDF) for local incidence angles of a) 10°, b) 40°and c) 70°.

Backscatter characteristics regarding specific materials

It has been reasoned in Chapter 4.1 that the surface of heaps of debris consists of multiple construction materials, including concrete, stone, structural steel, lumber, plastics, and insulation materials. In the course of differentiating radiometric backscattering characteristics, though, it is reasonable to reduce these to a few material instances with similar characteristics. It is considered unlikely that the backscattering characteristics of concrete and stone are that different to induce a measurable difference in signature. The same is pondered for plastics and metal. Also, insulation materials, due to a low density, are assumed to be penetrated by the signal and thus are disregarded, so that concrete, metal, and wood are regarded to cover the main backscattering characteristics.

Further, the surrounding ground plays a part in the simulation and extraction of the signature, not only due to the partially intermixing of signatures at the borders, but also due to potential multi-bounces between ground and debris. Consequently, asphalt is a crucial material, since in urban areas this is the prevailing surrounding ground. Table 4.4 lists the four materials that are distinguished and used in subsequent chapters, with italic type indicating the defined material instances. In the following, the procedure of adjusting material parameters is addressed, using reference signatures extracted from corresponding SAR imagery.

Even though the system noise is not a backscattering characteristic, it directly affects the image radiometry, and thus is part of generating correct radiometry. Due to the fact that the entire image is affected this has to be addressed as a first step. The *NESZ* parameter is tuned so as to attain a system noise similar to that of the real imagery. Since this factor is independent of target scattering, it best can be observed in image

Table 4.4.: Materials regarding heaps of debris.

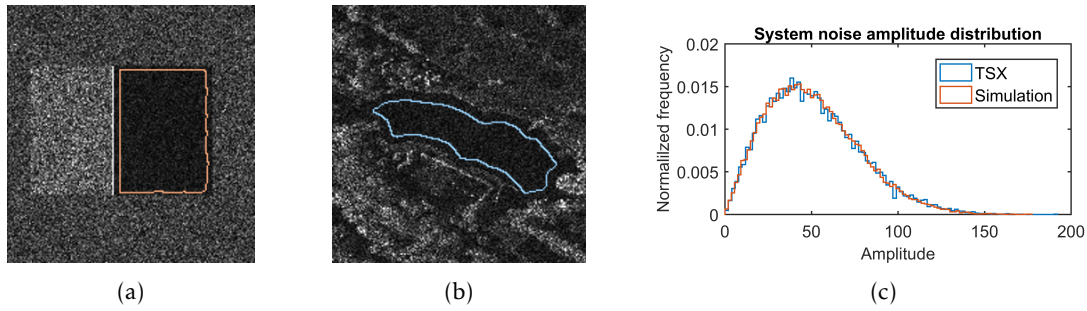| Instance	Name	Diffuse backscattering	Specular backscattering
1	*Asphalt*	little	medium
2	*Concrete, shattered*	rather high	dampened
3	*Wood*	medium	dampened
4	*Metal*	none at all	high

Figure 4.9.: Extraction of system noise; a) simulated amplitude image of shadow area (orange), b) reference SAR image showing a lake surface (blue) and c) their respective normalised grey level distributions.
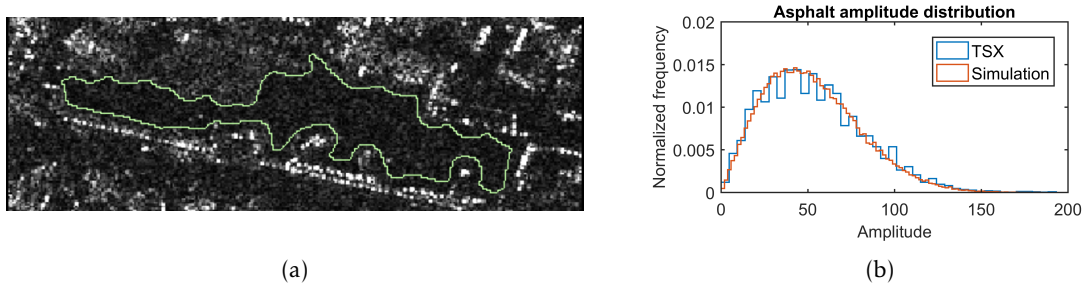

Figure 4.10.: Extraction of direct backscattering of asphalt; a) reference SAR image showing an empty car park (green) and b) the corresponding grey level distribution.

areas, for which no scatterer caused echo signal is received. The most straightforward area to meet this requirement is a shadow area, which using a plain high wall is very simple to simulate and that at an arbitrary size. Figure 4.9(a) shows a thus simulated amplitude signature, outlining (orange) the area in question. An extraction of shadow signature from real SAR imagery, though, proves to be rather unsatisfactory in terms of size, because real shadow areas in general have a rather limited size. A more suitable solution is presented by calm water surfaces, which specularly reflect all incoming signals away from the sensor and thus also yield mere system noise. Figure 4.9(b) shows the outlined (blue) amplitude signature of a small lake. Matching the simulated signature to the reference signature, by adjusting the parameter *NESZ*, produces a noise comparable to the (additive) system noise (see their conform normalised amplitude distributions in Figure 4.9(c)).

Regarding debris, there are three materials that are of interest (metal, concrete, and wood), which all possess rather smooth surfaces with respect to the wavelength. Hence their backscattering properties are rather high in specular reflection and very low in diffuse reflection. However, only the signature of asphalt occurs in large, planar and easy to extract areas and consequently is the only material suitable to be investigated straightforwardly. The diffuse part of the backscattering characteristics can be extracted directly from a planar reference area representing the corresponding material, whereas the specular part requires the shape of a dihedral or trihedral corner under a known aspect angle.

Diffuse scattering characteristics With asphalt being prevalent throughout urban scenes, a suitable reference area is presented for example by an empty car park, with Figure 4.10(a) showing such an area (green). The corresponding grey level distribution, plotted (blue) in Figure 4.10(b), shows a strong resemblance to the distribution of the pure system noise in Figure 4.9(c) and thus suggests that asphalt induces very little diffuse backscattering. Hence, the simulation of asphalt requires only a very small σ_0 to match the direct reflection observed in the reference signature. It is to be noted that the backscattering coefficient for asphalt can vary depending on the state of maintenance, due to a changing surface roughness, which in itself is the focus of investigations [56]. However, the impact on X-band is rather small and thus is dismissed as irrelevant for this approach.
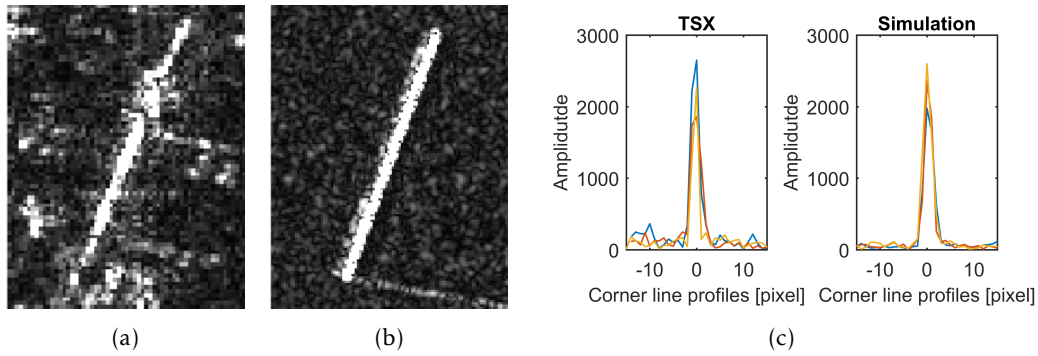
Figure 4.11.: A dihedral corner line caused by a single wall in a) a TerraSAR-X amplitude image and in b) a simulated amplitude image; c) Profiles across the corner lines of a) and b) respectively.

Compared to asphalt, the surface of metal is even smoother and thus does not require further investigation in terms of diffuse backscatter properties. Planar concrete and also plastering, commonly employed for building walls, has a surface roughness not too different to that of asphalt. However, debris that is formed by a building collapse, usually contains shattered concrete, which can have a distinctly rougher surface and thus induces more diffuse scattering. To acknowledge this fact, σ_0 is assumed to be markedly higher for the material referred to as *Concrete*. For similar reasons, this also is assumed for the backscattering properties of a wooden surface.

Specular scattering characteristics To determine the properties of specular scattering for asphalt, the case of a dihedral corner line is examined, with Figure 4.11(a) depicting the SAR signature of an individually standing wall. The supposed wall material is not asphalt but planar concrete; however, the similarities in roughness justify an interchangeable use of these materials for simulation purposes. Spatial wall dimensions, in particular the height, which is needed for the corresponding simulation, are estimated on the basis of optical reference data. The simulation of a dihedral corner is then generated using a simple cuboid formed wall standing on a ground plane (see Figure 4.11(b)). It is crucial to use the matching aspect angle to achieve comparable amplitude values for the corner line. In Figure 4.11(c) the amplitude course of profiles across the corner line (in range direction) is plotted for both, the TerraSAR-X signature and the simulated signature, showing the comparability of corner values. In order to be able to derive adequate parameter settings for σ_{max}, x, and y, this is repeated for further dihedral corners under different aspect angles. Since the materials (shattered) concrete and wood are distinctly rougher, the specular reflection is assumed to be markedly dampened in comparison. Metal on the other hand is assumed to be maximally specular, so that a large value is chosen for σ_{max}, with $x = 0$.

4.2.4. Simulated SAR signature of debris

In the previous sections the respective steps to enable the simulation of accurate debris signatures were described. Based on the representative variation of 3d models that was introduced as *Model set T* in Section 4.2.1
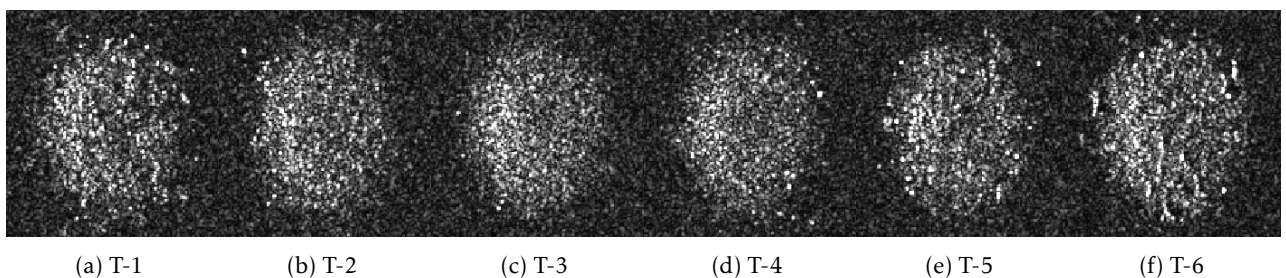

(a) T-1   (b) T-2   (c) T-3   (d) T-4   (e) T-5   (f) T-6

Figure 4.12.: SAR simulations of heaps of debris, based on *Model set T*.
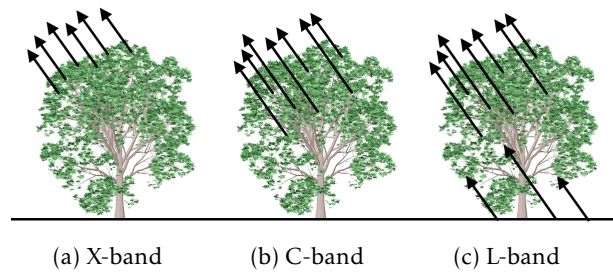
(a) X-band   (b) C-band   (c) L-band

Figure 4.13.: Schematic backscattering mechanism of foliated tree for several frequency bands.

the simulation process is carried out using simulation parameter settings specified in Section 4.2.2. The four material instances described in Section 4.2.3 are assigned according to the individual cuboid form and their contemplated representation. Figure 4.12 depicts the resulting simulated amplitude images for a 30° incidence angle. A distinct difference in signature originates as a combination of varying macroscopic surface roughness and prevalent material backscattering properties. Combined, these simulations are considered to cover predominantly occurring types of debris signatures.

4.3. Cases of texture similarity

Even though the signature of debris with its type of random clutter is rather exceptional, signatures of similar character exist and thus need to be addressed in order to enable a reliable debris detection algorithm. The proposition of being independent of post-event image data concerning training samples necessitates the simulation of these similar textures as well. By far the most substantial cause for a similar texture turns out to be high vegetation, meaning single trees or also clusters of trees (forests). The large quantity of high vegetation occurrences even in urban scenes makes this a high priority aspect. Further, the surface of gravel as in small scale rubble was identified to also induce a signature very similar to that of debris. The following focuses on the analysis and simulation of these two signatures with the aim of producing textures that allow for a separation from the signature of debris. While there exist further textures of similar character, those are not caused by surfaces belonging to individual objects but rather are the result of a random mix of object surfaces and thus cannot be categorised and generalised.

4.3.1. Vegetation

The SAR signature of vegetation is focused on in multiple investigations mostly for large scale biomass assessment [41] using C-, L- or even P-band. This includes assessment of the forest area and structure, tree height measurements, and monitoring changes. The preferential use of low frequency bands is rooted in the fact that the penetration depth regarding foliated trees varies heavily for the different wavelengths. Figure 4.13 demonstrates the schematic backscattering mechanisms for several frequency bands, showing that for C- and L-band
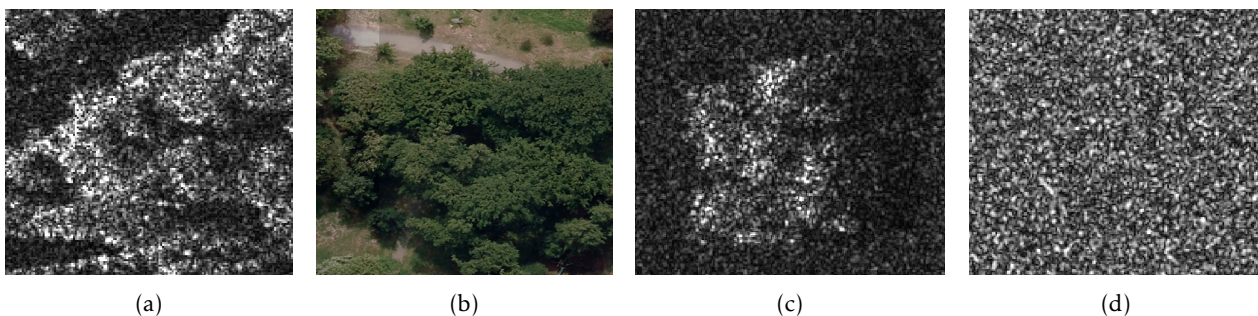

(a)   (b)   (c)   (d)

Figure 4.14.: Cluster of trees in a) TerraSAR-X imagery, b) optical imagery and c) simulated image; d) simulated signature of gravel.

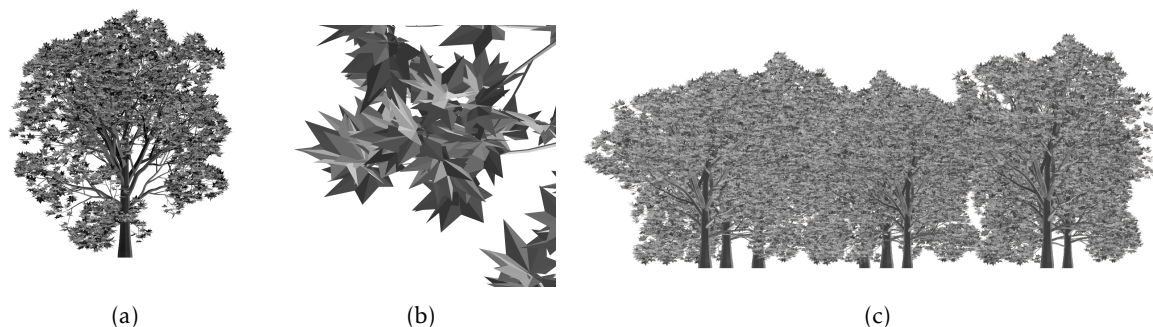(a)   (b)   (c)

Figure 4.15.: Detailed 3d model of a cluster of trees.

the signal penetrates as deep as branches or even the ground, which is exploited in biomass assessment. In contrast, the X-band signal is reflected almost entirely from the tree crown. Thus, the developing signature is characterised by random volume scattering regarding the outer surface of the tree crown. Figure 4.14(a) displays the typical X-band SAR signature of foliated trees (see Figure 4.14(b) for the optical counterpart), making the texture similarity to debris apparent.

On account of the formation mechanism regarding the signature of vegetation, an accurate simulation can only be achieved by using a highly detailed 3d model, with separately modelled leaves. A more rudimental approach to modelling, in contrast, leads to strong unrealistic backscattering in the simulation. The 3d model that was used here consists of over 195,000 polygons and represents a fully foliated oak tree of approximately 16 m height. Figure 4.15(a) shows this tree model while Figure 4.15(b) demonstrates the level of detail regarding the leaf modelling. In order to also cover the passages between crowns, a 3d model representing a grove is used in the following, visualised in Figure 4.15(c) . It consists of a cluster of the introduced tree model featuring slightly different heights. Appropriate parameters regarding the backscattering characteristics of leaves were assigned, using high direct reflectance (σ_0) and a somewhat damped specular reflectance (with a rather wide specular reflectance lobe). Figure 4.14(c) shows the simulated signature of the cluster of trees, demonstrating the texture similarity in question. For reasons of comparison, the simulation was conducted with parameters matching those of previous debris simulations. In the following chapters, the simulated signatures of this oak tree are used for the generation of training samples and considered to be representative for all deciduous tree species in their foliated condition.

4.3.2. Gravel

Regarding the X-band wavelength of 3.1 cm, gravel has a very small-scale surface roughness. This means that with respect to the 3d modelling it is not necessary to employ a realistic scenario, actually consisting of millions of small gravel stones. It is sufficient to capture the (large scale) statistical characteristics of the surface, which can be achieved using simply a flat plane, which is endowed with a material consistent with a very rough and non-specular surface. Figure 4.14(d) shows the simulated signature achieved with this approach.

Chapter 5.

Detection of debris in post-event SAR data - Methodology

The analysis on building damages in Chapter 3 showed that the texture of debris is the most prominent characteristic of the SAR signature of damaged buildings and thus is most promising regarding a detection. Chapter 3 also included a discussion of the concept and the advantages of using simulated SAR signatures as training samples. Based on this framework, a debris detection algorithm was developed for the detection of debris texture in a single post-event HR SAR image using synthetic training samples. The general workflow of the algorithm is visualised in Figure 5.1, showing the consecutive processing steps. Note that the steps regarding the generation of synthetic training samples have already been recounted in Chapter 4, whereas the quantitative evaluation is focussed on in Chapter 6.
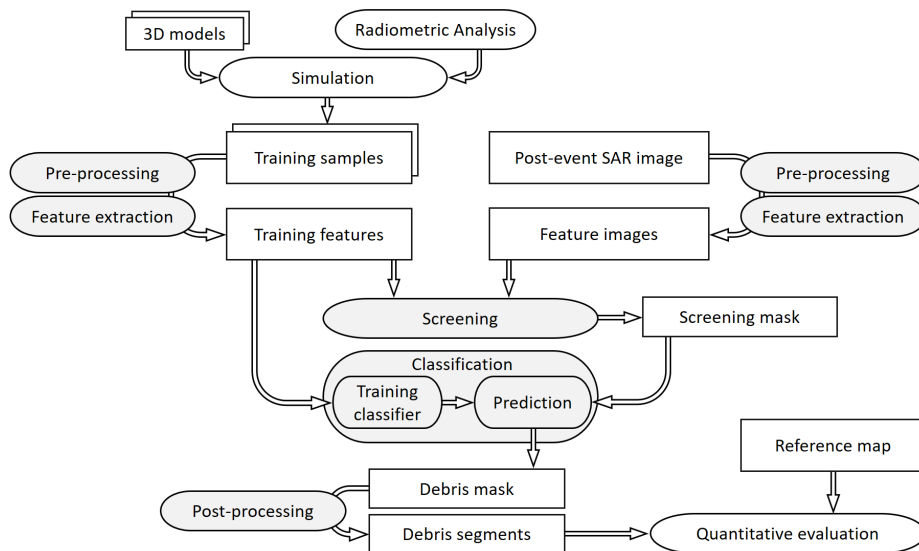

Figure 5.1.: Workflow of debris detection algorithm.

This chapter describes the individual processing steps that form the core of the algorithm (highlighted in grey), and provides a discussion on the choice of parameters and on alternative methods. It is structured as follows:

In Section 5.1 the pre-processing steps are presented, which involve radiometric calibration and dynamic scaling of the data base; Section 5.2 gives an account of aspects regarding the feature extraction; subsequently, in Section 5.3 a screening step is described, which localises areas of debris-like texture in the post-event SAR image based on an analysis regarding the potential variety of synthetic debris signatures; Section 5.4 specifies the classification process of separating debris from similar textures in the screening mask and the subsequent post-processing methods; and lastly, in Section 5.5 a short discussion is given regarding prospects and limitations of this approach.

5.1. Pre-processing

The approach to damage detection is based on a HS SAR image with a pixel spacing of about 1 m. The provided image format is SLC (see Section 2.1.4) with the signal represented by real (I) and imaginary (Q)

component, which then are converted to amplitude and phase. For the debris detection algorithm only the amplitude information is of interest; hence the phase component is dropped at this stage. In order for the amplitude information to be of use in the algorithm, several aspects have to be taken into account before feature extraction can be performed. This pre-processing comprises two steps, radiometric calibration and a dynamic scaling, which are applied to both the post-event SAR image and the synthetically generated training samples. The basics on these processing techniques were addressed in Section 2.1.5 .

5.1.1. Radiometric calibration

Aim of the algorithm is to introduce a method that is applicable to diverse HR SAR images of an individual X-band sensor and potentially even HR images of X-band SAR sensors in general. This requires a comparable data basis, and in particular that influences of the acquisition geometry on the radar backscattering are factored out. By applying a radiometric calibration, this issue, as well as potential differences regarding both sensor characteristics and image processing, are taken into account. As a result, the grey level values are directly related to the radar backscattering of the scene and are comparable to other images of the sensor. It is to be noted, though, that this does not cover potential radiometric variations caused by the topography in the scene or processing-specific differences such as the choice of windowing function.

The process of radiometric calibration is sensor specific. In the case at hand TerraSAR-X imagery is employed, hence the radiometric calibration is performed as specified by Equation 2.12. All input parameters are extracted from the meta data of the SAR image: Aside from the local incidence angle θ_{loc} (assuming a constant scene height) and calibration constant k_s this includes parameters concerning the noise estimate required for the calculation of the $NESZ$.

Regarding the generation of synthetic signatures, it was contemplated whether to directly simulate calibrated data. The fact that simulated data are not prone to changes in both sensor characteristics and image processing would suggest so. However, there is a future demand for simulations of alternative incidence angles since the target surface related backscattering differences caused by a change in incidence angle are not covered by the radiometric calibration. Hence, it was decided to generate uncalibrated simulations and consequently the radiometric calibration step also is required for the synthetic training samples.

5.1.2. Dynamic scaling

The large dynamic range of SAR imagery and the fact that most of the information content resides in the lower values makes a dynamic scaling crucial for many processing techniques. In particular quantisation based methods, such as the formation of a GLCM, which is employed in the following sections, require a reasonable distribution and ideally fixed ranges. In Section 2.1.5, basics on scaling methods were described, with logarithmic scaling being the most common choice of method. However, the lack of a fixed dynamic range renders logarithmic scaling problematic for the prospect of a GLCM based feature extraction. For the case at hand, a scaling with the hyperbolic tangent [72] is preferred to logarithmic scaling, since one characteristic of the hyperbolic tangent is a fixed dynamic scale (with the range $[-1, +1]$). Using this scaling method, the concentrated information content in lower values is stretched, whereas the sparsely occurring high value ranges (caused by strong point scatterers) are compressed. The reasoning and benefits of these preconditions are discussed in the quantisation process as a step of feature extraction (Section 5.2.3). The scaling is performed as specified in Equation 2.14 for both the training data (simulated signatures) and the post-event SAR image, whereas the calibrated intensities serve as input.

5.1.3. Discussion

The fact that the quality of SAR imagery is impaired by speckle noise hinders image interpretation significantly. This commonly prompts the use of established speckle filter algorithms, such as Lee, Kuan or Frost,
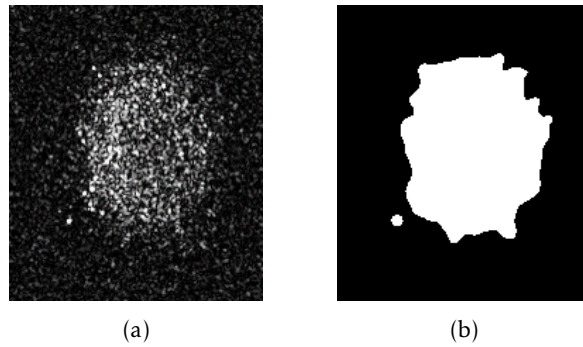
Figure 5.2.: Extraction of pixels of interest: a) Exemplary synthetic signature of debris and b) the corresponding extraction mask.

etc., which for a vast range of applications yields a considerable improvement. In the case of debris texture, though, this approach is arguable, since most speckle filters change the local statistics and thus cannot preserve the characteristics of debris texture. Regardless, it was assessed whether the debris detection algorithm would benefit from a Lee or a Frost filter. However, as hypothesised, this concept has proven to be counter-productive to the aim at hand and hence was abandoned.

5.2. Feature extraction

As a next step, the pre-processed image data, which comprise the training samples and the post-event SAR image, both in slant range geometry, are subjected to the process of feature extraction. With the quantitative analysis of the post-event test image in mind, the choice was made to use fully overlapping windows, even though this is computationally costly. Consequently, a segmentation resolution of one pixel is retained. As a result of this processing step, the post-event image is transformed to an $n \,\mathrm{x}\, m \,\mathrm{x}\, N_f$ feature matrix, where $n \,\mathrm{x}\, m$ denotes the size of the post-event test area and N_f stands for the number of features that are used. Accordingly, the necessary N_f-dimensional training feature vectors are obtained from the synthetic samples. Specifics on the process of feature extraction are discussed in the following. One aspect that needs to be taken into account in view of a classification is the potential benefit of a feature reduction. For this, an assessment regarding the relevance and redundancy of the feature set is conducted.

5.2.1. Training samples

In Section 4.2 the process of generating synthetic SAR signatures was discussed regarding debris, vegetation, and gravel, also introducing suitable 3d models and parameter settings. For the use as training samples with regard to a specific post-event SAR image the sensor and acquisition parameters need to match this post-event SAR image. In order to obtain a large enough data basis for the training process, the individual 3d models are simulated for 36 aspect angles in steps of 10°. Since surrounding signatures in real SAR imagery are random and thus cannot be simulated, there is made a point of using mainly sample windows located fully inside the signature.

In real SAR imagery an extraction of suitable signatures can be challenging, since other objects can interact with the signature in question. Synthetically generated samples (of debris, etc.) have the advantage that the texture can be extracted automatically, since no unexpected confounding factors can arise. Hence, to locate pixels in a simulated amplitude image around which sample windows are to be selected, a mask is generated by first filtering the images with a 2-D Gaussian smoothing kernel with standard deviation of 4 and then using a threshold as binarisation. Subsequently, for this area, the training samples are cut out from the original simulated images. Figure 5.2 shows this process for an exemplary simulated amplitude image. This process is applied accordingly for the extraction of vegetation samples, whereas the signature of gravel does not require this processing step, due to its simpler method of simulation.

Table 5.1.: Training samples used for debris detection algorithm.

Class	Model	Number of simulations	Number of samples
Debris	Model T-1	36	500
	Model T-2	36	500
	Model T-3	36	500
	Model T-4	36	500
	Model T-5	36	500
	Model T-6	36	500
Vegetation	Oak trees	36	3000
Gravel	Plane	1	3000

In Table 5.1 the effective set of training samples is listed that are used for the following procedures of screening and classification. Note that the use of synthetically generated training samples facilitates the establishment of a perfectly uniform class representation. The limit was set to 3000 samples for each class, which were evenly selected from the entirety of the class simulations. In the case of debris, it was ensured that an equal number of 500 samples was picked for each of the six debris models. The corresponding 3d models were introduced in Section 4.2.1.

5.2.2. Choice of texture features

The nature of debris texture is very random and not characterised by recurring patterns, as could be seen in Chapter 4. This suggests the use of statistical texture features instead of model- and transform-based methods or structural approaches. Several established statistical texture features were considered potentially suitable for the task at hand, including Haralick features [32], Laws texture energy measures (LTE) [52] and local binary patterns (LBP) [62]. First results regarding the texture analysis of debris showed that neither LTEs nor LBPs could keep up with Haralick features in terms of capturing debris specific characteristics and thus were not included in the following studies. Consequently the decision was made to exploit 21 features, consisting of 13 Haralick features and 8 statistics of the first order, listed in Table 5.2. Theoretical basics on these features were presented in Section 2.2.1. It is to be noted that the range of values amongst these features is vastly different, which is an issue for various processing techniques and thus requires further attention. In Appendix A this issue is addressed in more detail.

Table 5.2.: List of texture features exploited for debris detection.

	Feature	Notation	computed on
1	ASM	f_1	
2	Contrast	f_2	
3	Correlation	f_3	
4	Variance	f_4	
5	IDM	f_5	
6	Sum average	f_6	
7	Sum variance	f_7	GLCM
8	Sum entropy	f_8	
9	Entropy$_H$	f_9	
10	Difference variance	f_{10}	
11	Difference entropy	f_{11}	
12	Information measure 1	f_{12}	
13	Information measure 2	f_{13}	
14	Mean	μ	
15	Variance	σ^2	
16	Standard deviation	σ	
17	Kurtosis	κ	
18	Skewness	γ	amplitude image
19	Entropy	H	
20	Median	$\tilde{x}$	
21	Maximum	x_{max}	

Table 5.3.: Parameters regarding feature computation.

Parameters		Proposed settings
Window	Method	fully overlapping
	Form	quadratic
	Size	11 x 11
GLCM quantisation	Type	linear binning of hyperbolic tangent scaled grey values
	Value range	[-1,1]
	Number of bins	64
GLCM spatial pixel relation	Distance	1
	Orientation	rotation invariant: 0°, 45°, 90°, 135°
	Symmetry	symmetric

5.2.3. Parameters of feature computation

The information content of the used features depends significantly on several aspects concerning their computation. Hence, parameters need to be set carefully in order not to loose essential information regarding debris specific texture. This applies in particular to the Haralick features, which are derived from the GLCM and hence rely on a reasonable GLCM generation. It is crucial to use parameter values that are independent of any individual image to preserve image independence and consequently retain transferability towards other imagery. In the following, the choices for individual parameter settings are discussed in detail, whereas Section 2.2.1 provides the fundamentals regarding the formation of a GLCM, which is the computational basis of the Haralick features. The GLCM formation process involves the definition of the inter pixel relation, as well as several aspects regarding the quantisation, all of which have a strong impact on the GLCM occupancy and thus on the information content of the texture features. A list of parameter values that are used in this thesis for the extraction of debris specific SAR texture is provided in Table 5.3.

Window dimensions

Suitable dimensions regarding the feature extraction window are a main aspect of optimising the information content of features. The decision on window form and size, though, is target dependent and calls for the consideration of several aspects.

Window form   Slant range imagery in combination with the use of a quadratic window leads to a corresponding non-square ground range area, which can be problematic on account of two aspects: a potential orientation dependency of the texture and a false expectancy regarding the likely shape of the debris footprint. This would suggest the use of non-square windows to capture a uniform area. However, the case of an orientation dependency is better dealt with in the GLCM generation, which provides the option of a rotation variant (or invariant) processing. Also, since the aim is to use windows small enough to fit into the target signature multiple times, the issue of a distorted signature footprint proves to be irrelevant. Further, even though it is possible to conduct feature computation (also Haralick features) on even sized windows, it brings about problems concerning the definition of the window centre. On these grounds it was decided to use square, uneven sized windows.

Window size   The optimal window size is determined as a trade-off between locality and feature stability. To capture the locally characteristic texture, the window must be smaller than the object itself. On the other hand, feature stability decreases rapidly for small windows and thus cannot provide a reliable representation of the texture. For the HR SAR signature of debris, an 11 x 11 pixel window is used, based on the following considerations. On the one hand, the aim is to detect heaps of debris that are 10 m x 10 m or possibly even smaller. Given the full performance range (regarding incidence angle θ) of HS TerraSAR-X (see Table 2.4), the

Table 5.4.: Decreasing spread (Variance) of texture feature values for increasing window sizes.

Window size	f_1	f_2	f_3	f_4	f_5	f_6
7x7	1.0942e-06	427.726	0.00086354	429.5926	0.00014548	6.8799
9x9	5.6733e-07	282.2088	0.00054976	295.3991	0.00010441	4.7662
11x11	3.5962e-07	212.1634	0.00039783	222.9332	8.51e-05	3.6788
13x13	2.5385e-07	164.5575	0.0002889	182.4194	7.3106e-05	3.0426
15x15	2.0468e-07	140.2068	0.0002253	153.3511	6.6281e-05	2.6405

ground range pixel spacing can span from 133.0 cm x 85.7 cm (θ =20°) to 55.5 cm x 85.7 cm (θ =55°). Consequently, a potential heap of debris with a 10 m x 10 m extent is mapped to approximately 8 x 12 and 18 x 12 pixels, respectively. This demonstrates the need for a window size as small as 11 x 11 pixels or even smaller. On the other hand, a perceptible loss of feature stability can be observed for smaller windows, as was to be expected. A direct influence of the decreasing window size can be observed in the increasing spread (variance) of feature values. Table 5.4 shows the change of feature variance for an exemplary number of features regarding a set of window sizes. For this the simulated signature of debris (*Model T-2*) was used, a signature which represents a very homogeneous and extensive debris texture. Thus, for these values the potential problem of locality can be ruled out and all change can be attributed to the specifics of one texture in combination with an increasing window size.

Quantisation

In order to gain maximal significance for the Haralick features, a reasonable GLCM occupancy is crucial, which is achieved by a suitable quantisation of the image grey levels. In other words, an inapt quantisation can discard useful information. The quantisation step involves the definition of a quantisation method, the number of grey level bins and the range of values. SAR imagery in particular demands for a prudent approach to the quantisation step, due to its large dynamic range and non-uniform distribution.

Method and range of values   The suitability of a quantisation method depends on the image type and the corresponding signal statistics, which renders the common established methods, such as uniform or gaussian quantisation, inapt for the unscaled SAR intensities. A uniform quantisation, for example, would result in an immense information loss, since most relevant grey levels would end up in the lowest quantisation bins. Also it is refrained from setting some arbitrary maximal value (and thus cutting off the high intensity grey levels), since this disagrees with the prospect of preserving image independence. Instead, in Section 5.1.2, a scaling with the hyperolic tangent was introduced, which has two advantages: A fixed dynamic scale (in the range of $[-1, +1]$) and a beneficial stretching of relevant grey levels. The fixed dynamic scale provides the opportunity to use the entire range of values instead of choosing some arbitrary quantisation threshold for the GLCM computation. Since this scaling method with a subsequent uniform binning enables reasonable GLCM occupancies, it is the preferred quantisation method and as such is employed in the algorithm.

Number of bins   For a full dynamic range of the SAR image the GLCM would have dimension 2^{16}, a number that is much too large for computational reasons as well as due to a resulting GLCM sparseness. A reasonably large average occupancy level is required for the computation of the Haralick features. By decreasing the number of bins in the quantisation step and thus the size of the GLCM, the occupancy level is increased. In return, a quantisation too strong can cause a loss of information. Studies have shown that the ideal number of bins depends on the particular texture and may even be different for the individual texture features [16]. This however, exceeds the scope of this work and has not been investigated further. Figure 5.3 visualises the exemplary occupancy of a GLCM for a debris sample using 16, 32 and 64 grey levels. It becomes clear that the combination of a high number of grey levels and a very small texture window leads to a very sparsely occupied GLCM. Taking into account the window size of 11 x 11 pixels, 64 grey levels are used for the proposed

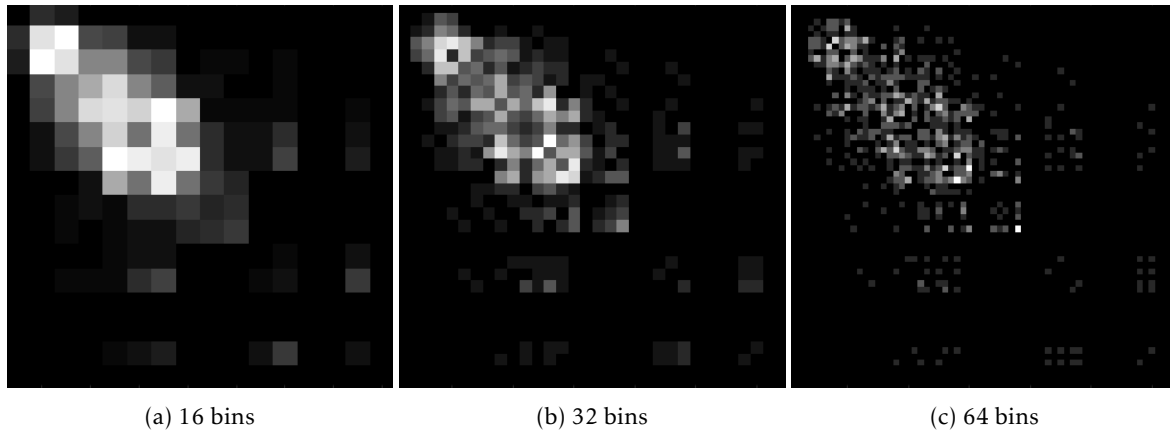(a) 16 bins   (b) 32 bins   (c) 64 bins

Figure 5.3.: Occupancy of the GLCM for an exemplary debris sample using different bin numbers.

analysis since this provides the best compromise between GLCM occupancy and preservation of detail for the task at hand.

Inter pixel relation

A further factor influencing the information content of the resulting feature values is the definition of the inter pixel relation. This involves the distance and orientation between pixels as well as aspects such as symmetry and rotation invariance.

Distance   The general aim is to select the pixel distance that best represents the target distinctive pattern/texture. Most commonly this is $d = 1$, since the fine scale information is lost when using larger pixel distances. The HR SAR texture of debris is judged such that in particular the fine scale pixel relation is of interest, rather than larger distances which prove to be increasingly random. Reoccurring relations at larger distance such as in patterns are not expected in debris texture. Hence, a pixel distance $d = 1$ is considered appropriate for the algorithm.

Rotation invariance   Theoretically, the SAR texture can exhibit a dependence on the inter pixel angle of orientation, in particular due to the differing pixel spacing in range and azimuth. Hence, a rotation variant computation of the GLCMs was considered. However, for the texture of debris no orientation depending differences in feature values could be observed, so that it was decided to produce symmetric and rotation invariant GLCMs. This implies using all four orientations ($\theta =$0°, 45°, 90°, 135°) and adding the transposed copy of the GLCM (thus making the matrix symmetric).

5.2.4. Discriminant analysis

Depending on the choice of classifier, redundant features (multicollinearity) and irrelevant features may cause overfitting and reduce the model performance, as well as lead to an unnecessarily high computational load. A random forest, though, which is the classifier of choice for this algorithm, is robust to redundancy in the feature set as are all tree based classifiers. As a consequence, a feature reduction can decrease the computational load but is not expected to improve the model performance. Since also the computational scope is manageable, it is refrained from performing a feature reduction for the random forest classification. However, in the course of a performance comparison regarding alternative classifiers (see Appendix A), which also involves an SVM, the concept of feature reduction is crucial. For this purpose, an impartial discriminant analysis is conducted with the aim of providing information about relevance and redundancy of the individual texture features and about the potential benefit of a dimensionality reduction.
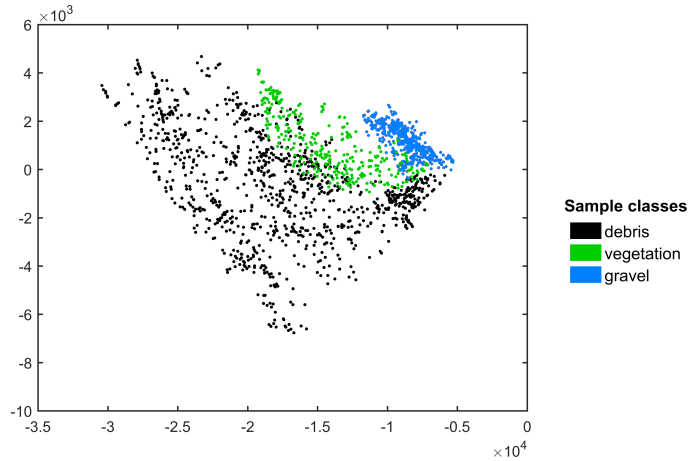
Figure 5.4.: 2d scatter plot of Sammon-projected feature values regarding the simulated signatures of the classes: debris (black), vegetation (green) and gravel (blue).

Class distinctness

Section 4.3 identified vegetation and gravel as sources of texture that are similar to debris. Whereas gravel occurrences are but isolated incidences, vegetation (if not separable from debris) inevitably poses a problem due to its commonly ample appearance in urban areas. Both labels are handled as classes in the classification process described in Section 5.4. Hence, it is of interest how well the chosen feature set is capable of distinguishing between the three classes. Following pre-processing and the extraction of features from the introduced training samples, first assessments regarding a potential separability can be conducted. For the purpose of a visual perception regarding the defined classes and their distinguishability, a multidimensional scaling is applied. For this a Sammon projection [71] is used, which maps high-dimensional spaces to a lower dimensionality (in this case 2 dimensions), while seeking to preserve the structure of inter-point distances. This is done by minimizing the error function E:

$$E = \frac{1}{\sum_{i<j} d_{ij}^*} \sum_{i<j} \frac{(d_{ij}^* - d_{ij})^2}{d_{ij}^*},$$ (5.1)

where d_{ij}^* denotes the distance between the ith and jth objects in the original space and d_{ij} is the distance between their projections. Figure 5.4 depicts the Sammon-projected feature clusters of the simulated signatures of debris (black), vegetation (green) and gravel (blue). The plot reveals that the signature of debris comprises a comparably wide diversity of texture characteristics, which is reasonable given the large range of possible debris configurations. The feature clusters of the three classes do overlap partially due to their texture similarity, however, large parts of vegetation and especially of gravel seem to be clearly discriminable by the feature set.

Feature redundancy

The chosen feature set is expected to be correlated to some extent. Figure 5.5(a) visualises the mutual information of the 21 features, employing the order of features that was introduced in Table 5.2. It was calculated as described by Peng et al. [64] based on the feature vectors derived from the training samples. White pixels denote a high interdependence between two features, whereas black pixels denote a lack of any mutual information. The plot provides an idea about the multicollinearity and confirms the assumption of feature redundancy in the set, thus suggesting a feature reduction.
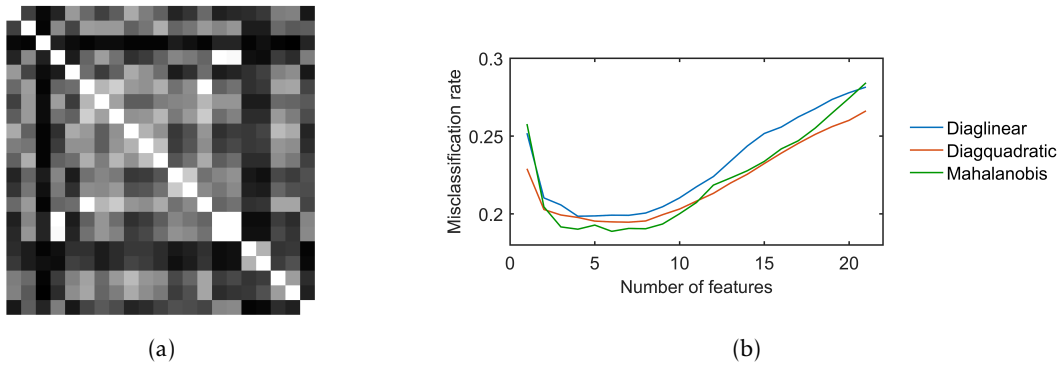
Figure 5.5.: a) Mutual information of the 21 texture features introduced in Table 5.2 (white pixels denote a high correlation whereas black pixels denote a low correlation); b) misclassification rate regarding a sequential feature selection for three different discriminant functions.

Sequential feature selection

Dimensionality reduction can be performed with a number of techniques, either choosing a suitable subset of features or projecting the features to a lower dimension. It was decided to perform a forward sequential feature selection, which involves a repeated and sequential adding of a feature until no further improvement of the classification rate is achieved. With changing subsets (random sampling) of training and test samples a 10-fold cross validation without stratification is carried out for each feature subset. Since the range of values for the different features varies strongly, a z-score standardisation (transformation to a mean of zero and a standard deviation of 1) is conducted on the feature vectors prior to classification. The analysis is performed on the simulated samples of debris, vegetation and gravel.

Figure 5.5(b) shows the criterion describing the misclassification rate for several types of discriminant functions. Due to several strongly correlated features, the resulting feature order varies with the random sample subset and the chosen discrimination function. However, they agree on the fact that a minimal misclassification rate is achieved for up to 8 features and that retaining all features leads to a drastic reduction of the model performance (overfitting).

A final subset of features was chosen based on the results of the feature selection using Mahalanobis distances. Table 5.5 lists the corresponding sequential feature selection regarding the 10 first picks. The minimal misclassification rate (0.1887) suggests a selection of the first 6 features. As was mentioned before, for many classifiers, amongst others the SVM, a feature reduction is crucial for a good performance. Thus, the later use of an SVM in Appendix A makes use of this feature selection, not however the random forest classification of the described algorithm.

Table 5.5.: Forward sequential feature selection (Mahalanobis distance): order of features with their corresponding misclassification rate.

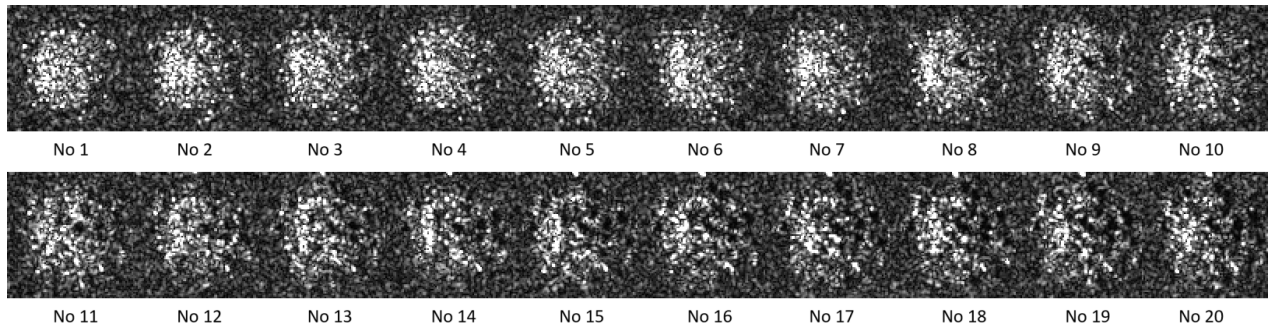| No	Feature	Criterion
1	σ	0.2577
2	f_1	0.2044
3	f_{13}	0.1915
4	f_{10}	0.1901
5	κ	0.1927
6	f_3	0.1887
7	f_5	0.1905
8	f_9	0.1904
9	σ^2	0.1934
10	x_{max}	0.2000

Figure 5.6.: Synthetic SAR signatures of debris with decreasing macroscopic surface roughness (left to right) based on model set *M2*.

5.3. Screening

To directly exclude areas that feature a type of texture that is easily separable from the texture of debris, a screening is conducted on the post-event test area. This is accomplished using fixed intervals for the introduced set of texture features that represent the full characteristic feature ranges of the texture of debris. To define these feature intervals, in the following insight is acquired as to the factors influencing the texture. As a result of the screening, a pixel mask is gained, which pinpoints areas of debris-like texture in the post-event SAR image.

5.3.1. Characteristic range of debris texture

Chapter 4.2 pointed out the two main factors affecting the texture of debris: The macroscopic surface roughness and the predominant materials (backscattering characteristics). In the course of defining characteristic feature limits, these factors and their extent of influence on the texture features are of interest.

Macroscopic surface roughness

In order to encompass and follow the influence of the macroscopic surface roughness, a systematic analysis is conducted. The limited availability of real debris signatures renders the use of simulated signatures necessary, which enables the observation of changes caused by controlled, stepwise debris model alterations. For this purpose two sets of 3d models (*M1* and *M2*) have been introduced in Section 4.2.1, both consisting of 20 heaps with a gradually decreasing macroscopic surface roughness, generated using two different methods. Firstly, it is assumed that the model sets span the whole range of real macroscopic surface roughnesses, so that the essential texture variations are covered by the simulations. Secondly, the two model sets start and close with 3d models that have approximately the same degree of macroscopic roughness, thus enabling a direct comparison. In order to be able to isolate the texture change corresponding to the macroscopic roughness, all cuboids of the models are assigned the same backscattering characteristics, using the previously introduced material *Concrete* (see Section 4.2.3), which is the predominant type of material in heaps of debris. To achieve robustness in the signature analysis, a high quantity of signatures is required. Rather than using several models per degree of macroscopic roughness, each model is simulated for 36 aspect angles in steps of 10° to mitigate the effect of randomly generated corner reflectors on the texture analysis. The simulations are conducted using sensor parameter settings that match those of TerraSAR-X HS mode (specified in Table 4.3). Figure 5.6 depicts the simulated amplitude images regarding the full range of macroscopic surface roughness (model set *M2*) for an exemplary aspect angle. A distinct change in texture can be observed.

How this texture change manifests itself in the chosen set of texture features is assessed in the following. For this, feature extraction is conducted as described in Section 5.2 on the pre-processed multi-aspect simulations of the model sets *M1* and *M2*. To best observe the changes in feature values regarding the individual models (degree of macroscopic roughness), the arithmetic means as well as the corresponding 0.05- and 0.95-quantiles
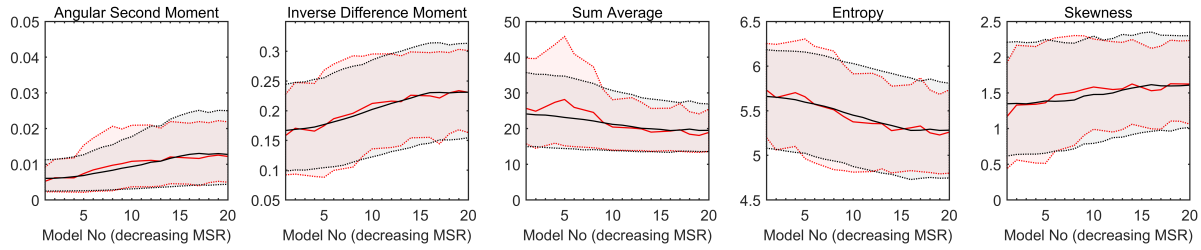
Figure 5.7.: Feature development of 20 heaps of decreasing macroscopic surface roughness regarding Model set M1 (red) and Model set M2 (black) simulated for material *Concrete*. Plotted are the arithmetic means and the 0.05/0.95-quantiles, respectively.
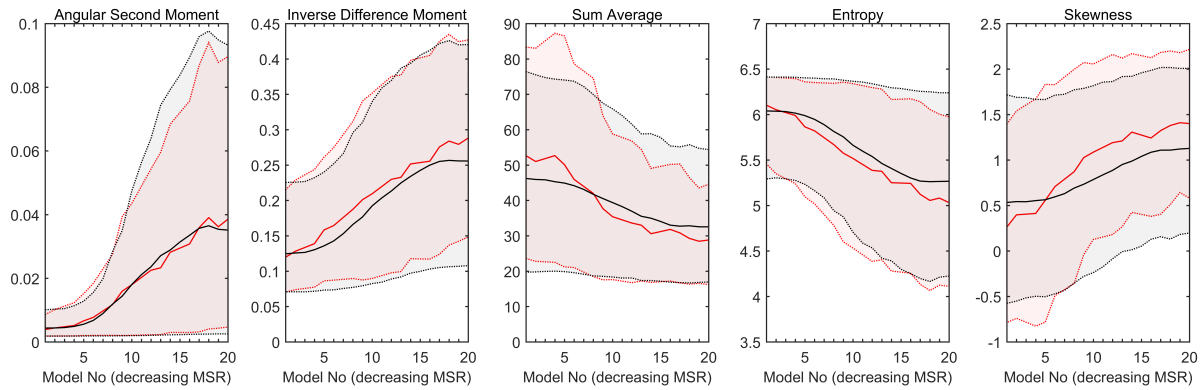

Figure 5.8.: Feature development of 20 heaps of decreasing macroscopic surface roughness regarding Model set M1 (red) and Model set M2 (black) simulated for material *Metal*. Plotted are the arithmetic means and the 0.05/0.95-quantiles, respectively.

are monitored, respectively. For an exemplary feature subset, Figure 5.7 shows these values, plotted against the model sets *M1* and *M2* of decreasing macroscopic surface roughness (from left to right). As expected, the constant, stepwise change of roughness yields a (mostly) monotonic change in all feature values. Even though the manner of changing the macroscopic roughness was different for the two model sets, while only an equal range of roughness was defined, the resulting feature curves coincide very well. It is necessary to include this extent of texture variations in the screening step of the detection algorithm.

Material backscattering properties

The backscattering properties of different kinds of materials that are present in heaps of debris are known to have major influence on the texture of debris. In particular, the presence of highly specular areas in combination with the formation of corner reflectors has a great impact. To understand the extent of texture change due to a more specular material, the assessment that was conducted for the macroscopic surface roughness is repeated for the material *Metal*. However, this is a purely theoretical case since metal does not typically occur for large planes in such formations and hence provides only for a better understanding of the influence on the texture features. Comparable to Figure 5.7, Figure 5.8 shows the results for the textures that were simulated assuming a specular surface. Note the unequal scaling range regarding the two figures. Results show for one, that the spread of feature values is considerably higher than for the more diffuse material *Concrete* and also, that the monotone texture change caused by the surface roughness is more distinct. Even though these findings are not directly taken into account, they make the importance clear that in order to provide for a representative set of debris textures, realistic amounts of specular objects need to be included.

5.3.2. Feature intervals and screening mask

Having defined the extent of the macroscopic influence, as well as the importance of a realistic specular presence, feature intervals are defined for the subsequent screening step. The synthetic signatures, simulated with the six 3d models in set *T* (introduced in Section 4.2.1), combine the relevant range of macroscopic surface
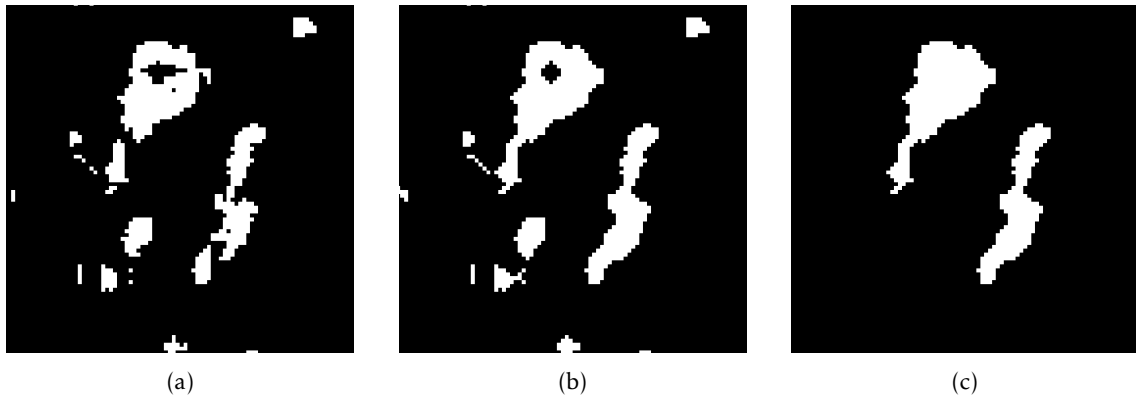
(a)   (b)   (c)

Figure 5.9.: Processing stages of the screening mask for an exemplary set of components: a) original state, b) after morphological closing, c) after dropping small components and filling holes.

roughness as well as a realistic specular presence. The full range of the corresponding feature values contains outliers, which are not only not representative for the texture of debris but also are problematic since they increase the feature intervals significantly. On that account, the feature intervals are defined instead by the 0.05- and 0.95-quantiles, with Table 5.6 listing the effective feature intervals.

The process of screening is subsequently carried out using a test of inclusion for each pixel of the post-event feature images with respect to each feature interval. As a result a binary mask is obtained that specifies areas with a debris-like texture, which then is transformed to connected components using 8-pixel connectivity. Since this mask is the basis for a classification as well as the subsequent evaluation, some basic post-processing steps are required. By nature, the mask is rather pixelated and contains numerous very small components that are below the area size that is expected to be detectable. Correspondingly, components of a small pixel count (less than 50) are removed from the mask. In order for this process not to drop small areas that are in direct adjacency to larger areas, the elimination of small components is carried out only after a morphological closing operation. Also, the mask components are cleared of small holes, which may be caused by single strong point scatterers amid the texture. The resulting mask is referred to as screening mask in the following. In Figure 5.9 the effects of these screening mask operations are visualised for an exemplary scene.

Table 5.6.: Effective feature intervals used for the process of screening.

| Feature	Interval		Feature	Interval	
f_1	[0.0018	0.0072]	μ	[0.9799	$3.1744] \cdot 10^4$
f_2	[91.9333	374.4328]	σ^2	[0.9005	$3.7424] \cdot 10^8$
f_3	[0.2501	0.6156]	σ	[0.9489	$1.9345] \cdot 10^4$
f_4	[80.9291	359.2313]	κ	[1.8002	5.7359]
f_5	[0.0674	0.1920]	γ	[-0.1450	1.7146]
f_6	[19.9412	63.1715]	H	[5.7450	6.5200]
f_7	[0.5083	$4.2893] \cdot 10^3$	$\tilde{x}$	[0.5893	$3.3049] \cdot 10^4$
f_8	[3.7526	4.5664]	x_{max}	[4.1066	$6.5320] \cdot 10^4$
f_9	[5.4911	6.4391]			
f_{10}	[0.2588	$0.8842] \cdot 10^3$			
f_{11}	[2.9124	3.6166]			
f_{12}	[-0.3361	-0.1796]			
f_{13}	[0.8156	0.9607]			
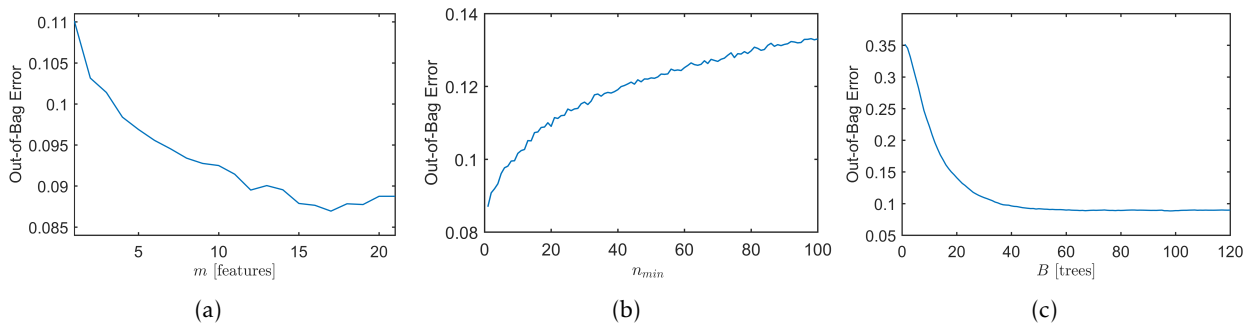
Figure 5.10.: OOB error regarding three hyperparameters: a) the maximum number of features m, b) the minimum number of leaf samples n_{min} and c) the number of trees B.

5.4. Classification

Since there are surface areas that result in SAR signatures of similar character as debris, the screening mask cannot be a reliable indication for debris occurrences. The most prominent sources of similar texture have already been identified as vegetation and gravel and corresponding training samples have been generated (see Table 5.1). Based on these training samples a classifier is trained and optimised and subsequently predictions are made for the post-event image samples with the aim of a reliable separation of non-debris signature from proper debris. A random forest classifier is employed for this, with the basics and the required parameters having been described in Section 2.2.2.

5.4.1. Training

The training of a random forest consists of the building of an ensemble of decision trees using random subsets of the introduced training samples. By tuning several hyperparameters this ensemble is optimised.

Building of trees

Controlling the tree building process is a matter of several hyperparameters, which need to be optimised to obtain a good model performance. In the following, the adjustment of the main hyperparameters is described, whereas Out-of-bag Error (OOB) estimates are employed as measure of prediction error, thus avoiding the need for an independent validation dataset.

Number of features   To reduce the correlation between trees it is recommended to decrease the number of input features to select at random for each split (parameter m), thus providing for a certain randomness in the ensemble. However, for a feature set that contains noisy features or many redundant features, reducing the number of features also decreases the probability of choosing able features. In Section 5.2.4 a redundancy regarding the full feature set has already been established, hence disqualifying the recommended number of $m = \sqrt{p}$ features of the p input features. The tuning of the parameter m showed a minimum OOB error for $m = 17$ features (see Figure 5.10(a)). Thus, the parameter m was set to 17 features.

Tree depth   It is important to grow trees deep enough to prevent underfitting of the model, whereas the computational cost is the main downturn of using fully grown trees. Meanwhile, overfitting usually is not a problem but for very complex trees. The tree depth can be controlled e.g. by the minimum number of samples per tree leaf n_{min}, with 1 producing fully grown trees. Figure 5.10(b) shows the OOB error for the tuning of n_{min}. For the classification fully grown trees are used since the computational load is manageable, however, it was found that reducing tree depth moderately does not decrease the classification performance.

Number of trees   A high number of trees generally leads to a better accuracy but also increases the computational load considerably. The aim is to build enough trees to produce a good model performance, but as few as possible in order to have a manageable computation time. Figure 5.10(c) shows the OOB error for an increasing number of trees B. It is revealed that a number larger than approximately 60 trees does not improve the model performance significantly and thus represents an appropriate setting for the classification process.

Data balance

A lacking balance in the training data (or test data) often is a problem for classification algorithms, since they aim to minimise the overall error rate. An under-representation of a class may thus cause a poor prediction rate for that class. Since the introduced training data set is perfectly balanced - an advantage of using synthetically generated samples - this is no issue for the approach at hand. Nevertheless, a cost sensitive learning is deemed beneficial, since the aim is to reliably detect debris rather than achieve an overall accurate classification result. Hence in this case it is expedient to adapt the misclassification cost in favour of the class debris. By means of the square matrix

$$C_{i,j} = \begin{pmatrix} 0 & 1 & 1 \\ 0.8 & 0 & 0.4 \\ 0.8 & 0.4 & 0 \end{pmatrix}, \tag{5.2}$$

where rows denote the true classes i (debris, vegetation, gravel) and columns denote the predicted classes j (debris, vegetation, gravel), the cost is redistributed. High cost is applied for the misclassification of true debris ($C_{i,j}$=1), moderate cost for falsely predicted debris ($C_{i,j}$=0.8) whereas little cost is applied for the misclassification between the two classes vegetation and gravel ($C_{i,j}$=0.4). This is done in order to prevent loosing much of the true debris while accepting the trade off to allow for falsely classified debris. It is to be noted, that as a consequence the predicted class debris is bound to contain a rather high level of misclassified vegetation and gravel.

5.4.2. Prediction

Using the generated ensemble of decision trees, a pixel-wise prediction is then conducted on the areas defined by the screening mask. Based on the posterior probabilities regarding the individual trees, an ensemble decision (weighted voting) is made for every sample. As such, the classification produces pixel-wise class results.

5.4.3. Post-processing

In practice, a component-wise decision rule (connected component labelling) is preferred to a pixel-wise class result. It stands to reason that the individual connected component may contain more than one class for the case of adjacently located class occurrences. In particular for large connected components this needs to be taken into account, thus necessitating a segmentation. The segmentation is realised using the median filtered pixel-wise classification results and conducting a dilation based region growing emanating from class components that have a minimum size of 50 pixels. Meanwhile, for small components a simple majority vote is deemed adequate. Returning to the exemplary set of components shown in Section 5.3, Figure 5.11 illustrates the effect of the post-processing operation on the pixel-wise classification result.
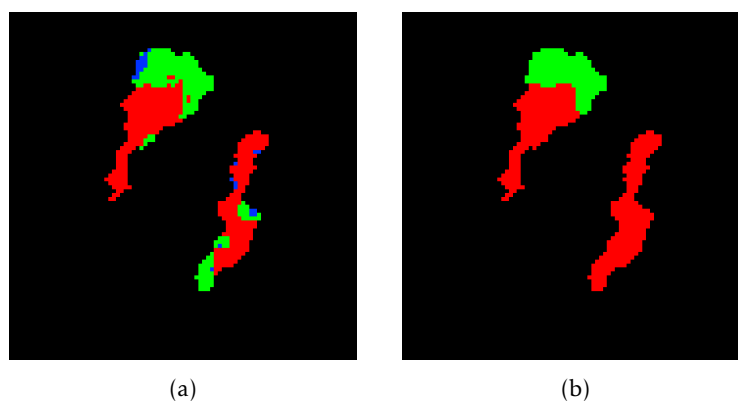
Figure 5.11.: Processing stages of a classification result with debris (red), vegetation (green) and gravel (blue) for an exemplary set of components : a) the pixel-wise class results, b) the post-processed component-wise class results.

5.5. Discussion

The previous sections described the methodology of the debris detection algorithm, split into the individual processing steps. In the following, some limitations of the detectability are discussed that are brought about by different aspects.

A major downside of using SAR imagery for this kind of problem is the typical image acquisition geometry. The oblique line of sight leads to extensive shadowing (and layover effects) in urban areas and particularly in inner-city districts. As a consequence a significant share of the actual number of heaps of debris are not mapped in SAR imagery and hence cannot be detected based on one image. An assessment as to the extent of shadowing for an urban scene in given in Section 6.3.3. The detectability of heaps of debris is also limited by the introduced processing chain of the algorithm and its settings in combination with the image resolution. In Section 5.2.3 a window size of 11 x 11 pixels was established as the minimum requirement for the generation of stable texture features. Assuming a HS TerraSAR-X image with an incidence angle of 45°, this represents a corresponding debris area of 7.1 m x 9.5 m. With this setting a hard limiting factor is introduced to the proposed approach in terms of debris detectability, since debris areas of a smaller footprint are very unlikely to be detected. This is taken into account in the quantitative evaluations conducted in Chapter 6. Further, a minimum number of component pixels (generated by overlapping windows) is defined to allow for small components to be dropped (see Section 5.3.2). Depending on the incidence angle/ pixel spacing of the given image this value may require adjustment. Note that this step further increases the minimum footprint of potentially detectable debris instances.

Chapter 6.

Results

This chapter starts with a description of the test data set, comprising a post-event HS SAR image and corresponding reference data (Section 6.1). In Section 6.2 the viability of the synthetically generated signatures is explored. Then, the results of the individual steps of the debris detection algorithm are shown in Section 6.3. Lastly, the chapter is concluded with a discussion on the methodology and the results in Section 6.4.

6.1. Data Set

On February 22, 2011 at 12:51 (local time) Christchurch, New Zealand (43°31'48"S / 172°37'13"E) was struck by a M_w 6.2 earthquake, with the epicentre located only 10 kilometres away from the city centre. Devastating destructions were caused throughout the city, whilst the central city (Central Business District) was hit particularly hard. The high number of heavy building damages renders this a fitting test area regarding a debris detection algorithm. As often is the case, initial post-event optical satellite images were obstructed by cloud cover as well as dust and smoke plumes, making SAR imagery the superior choice. The post-event data set acquired for this purpose includes a HS TerraSAR-X image and optical imagery (serving as reference data), both recorded shortly after the earthquake. In the following, specifics on these images are presented, as well as on training and test data used in the process and evaluation of the assessment.

6.1.1. Post-event SAR image

A High Resolution Spotlight 300MHz (HS300) TerraSAR-X image was acquired, recorded on February 23, 2011 at 20:23 (local time), showing large parts of the city of Christchurch, including the city centre. Image specifications are listed in Table 6.1, whereas technical facts on TerraSAR-X in general have been specified in Table 2.4. In the literature, post-event clean-up operations are reported to come in several phases, starting with the emergency phase with a duration of a few days to two weeks [10]. During this phase the efforts focus on immediate safety hazards and the clearance of access routes for the search and rescue operations [39]. Only after the emergency phase, the recovery phase starts, where the bulk of heaps of debris is removed systematically over a period of several years. On account of this, the time lag of 32 hours between earthquake and image acquisition is considered to be short enough for the majority of heaps of debris to remain in their pristine state. Figure 6.1 gives an understanding regarding the coverage of the acquired SAR image, showing the extent of the rectified SAR image and the corresponding general acquisition footprint. It is to be noted that the SAR image has been rectified only for visual purposes. The green outline marks the Central Business District, which serves as test area in the following assessment.

Table 6.1.: Specifications on post-event TerraSAR-X image.

Acquisition time	2011-02-23 20:23 local time (1 day post-event)
Mode	High Resolution Spotlight 300MHz (HS300)
Polarisation	HH
Pixel spacing	45.47 cm (slant range) x 85.72 cm (azimuth)
Scene size	7 km x 5 km
Incidence angle	47.38°
Path direction	Ascending
Product type	SLC

(a)
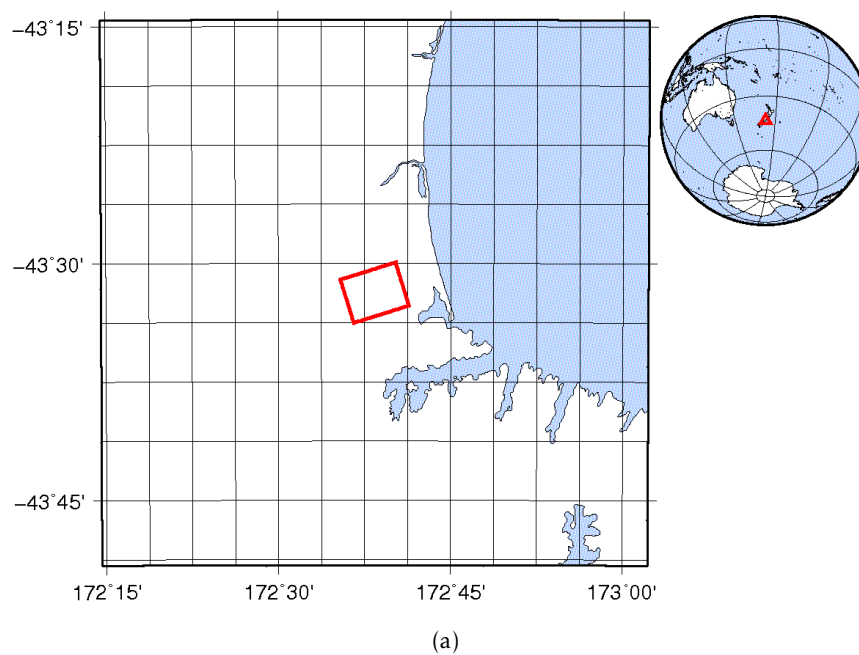
(b)

Figure 6.1.: Overview of the post-event TerraSAR-X image of Christchurch, New Zealand, delivered as part of the image ordering. a) the image footprint and b) the rectified SAR image with the outlined (green) city centre.
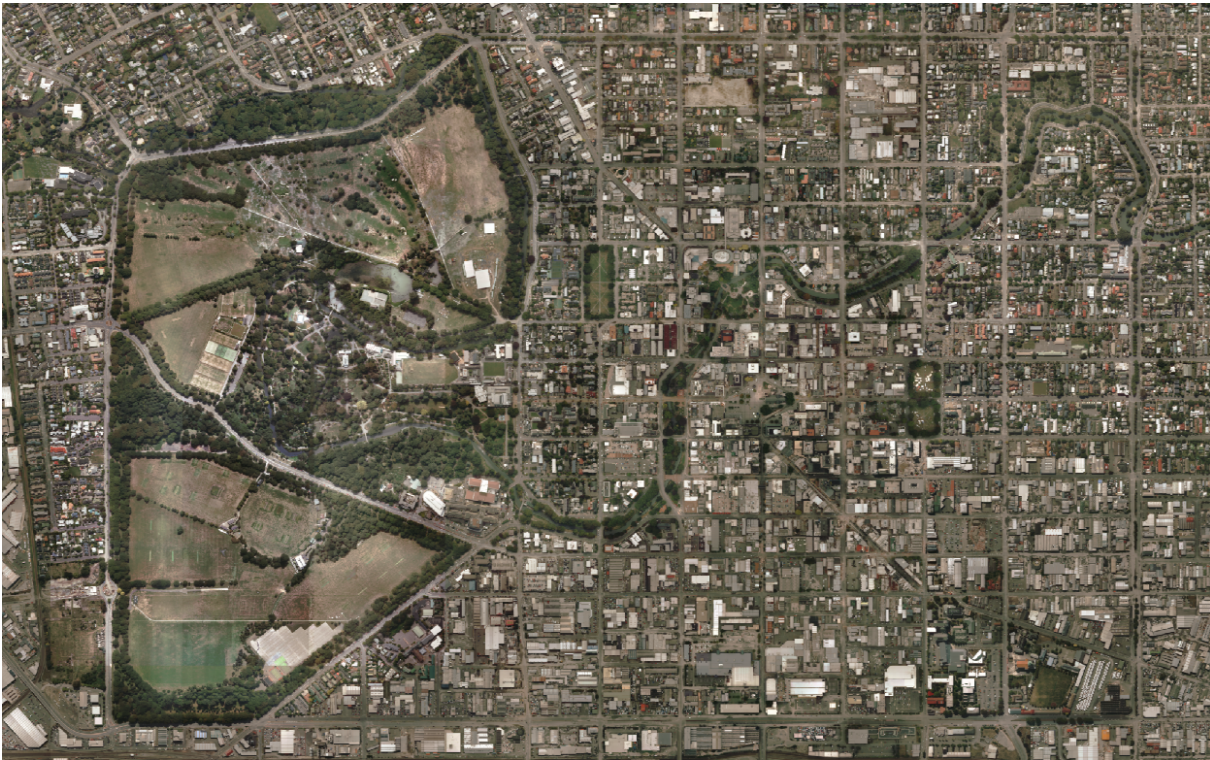
Figure 6.2.: RGB orthophoto mosaic of the city centre of Christchurch, New Zealand, after the earthquake in 2011 (imagery was provided by Land Information New Zealand).

6.1.2. Reference data

In the aftermath of the earthquake different kinds of damage maps were generated: various maps focusing on liquefaction or the problematic road and bridge qualification [17], maps of property-based land damage [78], and also commercially available building damage maps. However, a ground truth of sub-building precision, which ideally puts focus on the presence of debris, was not available. On these grounds, a reference map was generated based on additional data, as described in the following.

Orthophoto mosaic

On February 24, 2011 (local time), New Zealand Aerial Mapping acquired airborne optical images of the city, with 10 cm resolution for the Christchurch Response Centre to help the rescue operations. The ortho-rectified RGB images are provided by Land Information New Zealand and are available for download at [51]. Corresponding image specifications are summarised in Table 6.2. As the acquisition time is only one day after the TerraSAR-X image acquisition time, the use as source of reference is considered to be valid. The area referred to as Central Business District, located at the city centre, was chosen to serve as test area for the debris detection algorithm, since this area provides all aspects of interest. There are residential as well as commercial and industrial areas, thus comprising a wide range of construction types; the area shows plenty of high vegetation; and the city centre was hit particularly hard so that numerous severe building damages were caused. Figure 6.2 displays the orthophoto mosaic containing the city centre of Christchurch.

Table 6.2.: Specifications on optical reference image.

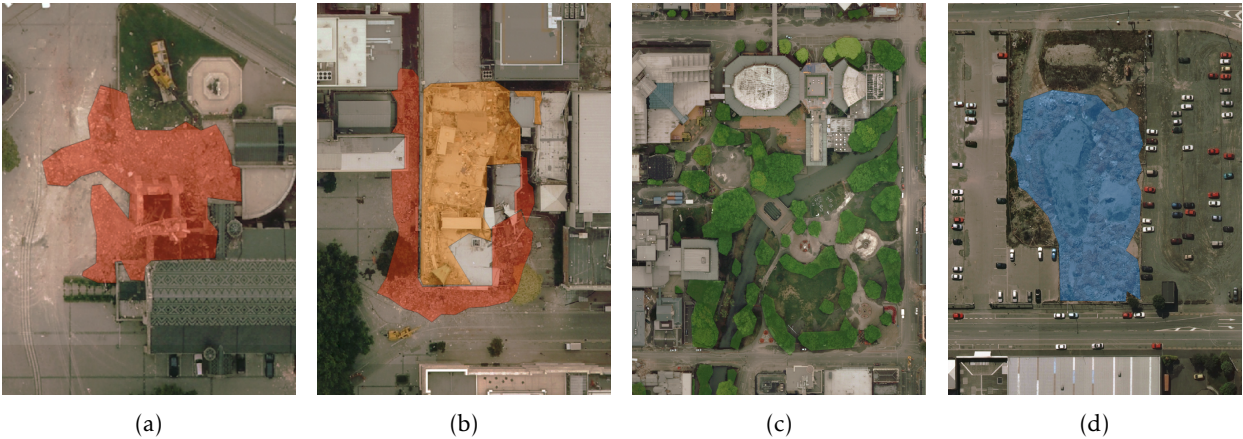|	
Acquisition time	2011-02-24 local time (2 days post-event)
Pixel spacing	0.1 m GSD
Bands	3-band (RGB)
Format	uncompressed GeoTIFF

69

Figure 6.3.: Image details on extraction of areas of interest: a) ground-level debris, b) higher-level debris, c) high vegetation, d) gravel.

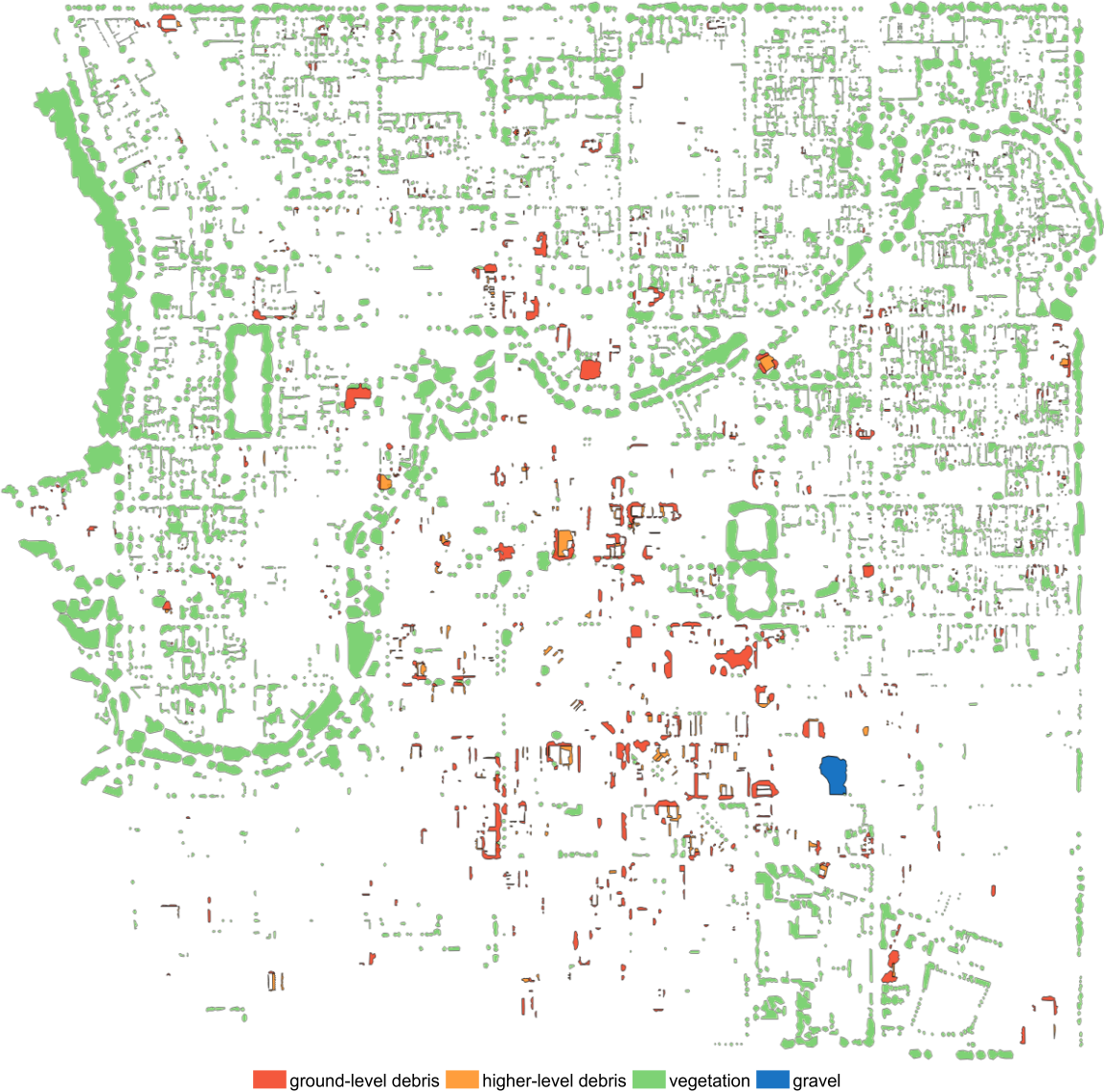◼ ground-level debris ◼ higher-level debris ◼ vegetation ◼ gravel

Figure 6.4.: Vector-based map of manually extracted ground truth with a differentiation between ground-level debris (red), higher-level debris (orange), high vegetation (green) and gravel (blue). The map geometry corresponds to the orthophoto mosaic.

Manual debris extraction

The prospect was to generate a map that is usable as reference (ground truth) for a quantitative evaluation of the debris detection algorithm in slant range image geometry. For a start, this was approached by manually extracting reference areas of interest based on the orthophoto mosaic of the Christchurch city centre. The resolution of 10 cm allows for a distinct identification and an exact mapping of even small heaps of debris. This can be observed in Figure 6.3(a), where a detail of an exemplary debris extraction is illustrated. Meanwhile, debris areas at ground level were distinguished from areas that are located on top of a building and thus reside at a higher altitude (see Figure 6.3(b)). Further, for reasons discussed in Section 4.3 high vegetation as well as gravel also are of interest and hence were included in the creation of the reference map (see Figure 6.3(c)). The prospect of detecting heaps of debris smaller than the feature window size (11 x 11 pixels), which corresponds to approximately $70\,m^2$ in the test image, is highly unrealistic and therefore all extraction areas smaller than $75\,m^2$ were dropped. Figure 6.4 depicts the thus generated entire vector-based reference map, with ground-level debris (red), higher-level debris (orange), vegetation (green) and gravel (blue).

SAR image geometry

In order to render the reference map directly comparable to the SAR image, two aspects require further consideration: Image geometry and target elevations. Since the debris detection algorithm is carried out on the slant range image, the geometry needs to be taken into account in the reference map. Image registration is achieved by rasterisation of the reference map and a subsequent tie point based transformation into slant range geometry. Accounting for the prevailing topography is considered unnecessary, since the elevation of the Christchurch city centre is formed by a rather constant ramp and thus is covered in the mentioned transformation. From this point on, reference areas are referred to as connected components. The fact that areas of higher-level debris as well as high vegetation are projected towards near-range, is rather precarious, since the respective heights are unknown. For vegetation at least it can be argued that the spread of the heights is much smaller (commonly not much higher than 10 m) and it is assumed that the heights correlate with the horizontal extent. Regarding the 47.38° incidence angle and the 45.47 cm range pixel spacing of the post-event TerraSAR-X image, this approximately amounts to a -15 pixel shift in range direction. Using attributes such as surface area and diameter, the reference components of vegetation are divided into two groups, representing coarsely the heights 5 and 10 m and subsequently are shifted by -8 and -15 pixels, respectively. Debris located on top of a building level is another matter, since heights can theoretically span up to more than 20 m, and thus averaging the height is not a reasonable approach. It is considered important though, to include the more common case of debris on lower levels of buildings (up to 13 m) and hence the reference components of higher-level debris are stretched in range by a corresponding 20 pixels, i.e. the component is elongated so as to cover all possible building heights. As a direct consequence of the shift and stretch operation, there is a problem of overlaying reference classes. This includes for one the case of ground located debris that is blocked by high vegetation and secondly higher-level debris that in SAR geometry is overlaying the signature of vegetation (or gravel for that matter). In order to take account of the first case, the reference map drops areas of ground-level debris if they coincide with areas of vegetation. In the second case the reference debris area is markedly larger than the actual debris signature due to the process of component stretching. Hence, the prospect of dropping all coinciding areas of other signature is unreasonable. Instead the areas in question are assigned to the corresponding ground level reference class. With a component wise evaluation in mind, this approach was chosen since it is considered to be essential that the reference map is complete, however, this needs to be taken into account in the evaluation process. Figure 6.5(a) depicts the resulting final slant range reference map with the corresponding SAR image cut-out in Figure 6.5(b).

ground-level debris · higher-level debris · vegetation · gravel

(a)

(b)

Figure 6.5.: a) Final reference map in slant range geometry ; b) the corresponding SAR image cut-out.

Figure 6.6.: 3d city model of the Christchurch Central Business District with a) specifying the model footprint on a WorldView-2 image and b) showing a detail of the model (LoD2.5) placed upon a DTM.

Figure 6.7.: Ancillary data derived from the 3d city model: a) shadow mask and b) layover mask with image parameters matching those of the post-event SAR image. Note that shadow and layover areas both are depicted in black.

6.1.3. Ancillary data: 3d city model

The evaluation process can benefit considerably from the use of ancillary data, such as shadow maps or layover maps. For this purpose, a LoD2.5 3d city model of the Central Business District of Christchurch was utilised, covering 3.2 km^2 in total [43]. As described in Section 3.3, LoD2.5 involves features such as detailed roof structures but lacks formations such as doors and windows. The 3d model was generated by PLW Modelworks using optical imagery from 2010, thus providing pre-event conditions. Figure 6.6(a) specifies the model footprint, which does not cover the entire test scene, but corresponds to approximately 70% of the test area. The model is shown in Figure 6.6(b), consisting of approximately 400,000 triangles and counting over 2100 buildings with accurate positioning in the UTM coordinate system. It was placed upon a triangulated digital terrain model (DTM) for the processing of shadow and layover masks. The simulation suite CohRaS, which was described in Section 2.3, provides the means to generate both a shadow- and a layover mask [29] in slant range geometry. Essentially, this is approached by calculating both the look angle and the distance to the sensor along every range line (from near to far range) using the model heights. Meanwhile, a decreasing distance denotes a layover whereas a decreasing look-angle indicates a shadow area. By imitating the image parameters, such as aspect angle, incidence angle and pixel spacing of the post-event SAR image (Table 6.1) a pixel-wise comparability/matching between the two masks and the SAR image can be accomplished. Merely the image offset needs to be taken into account. An exemplary detail of shadow and layover mask is shown in Figures 6.7(a) and 6.7(b).
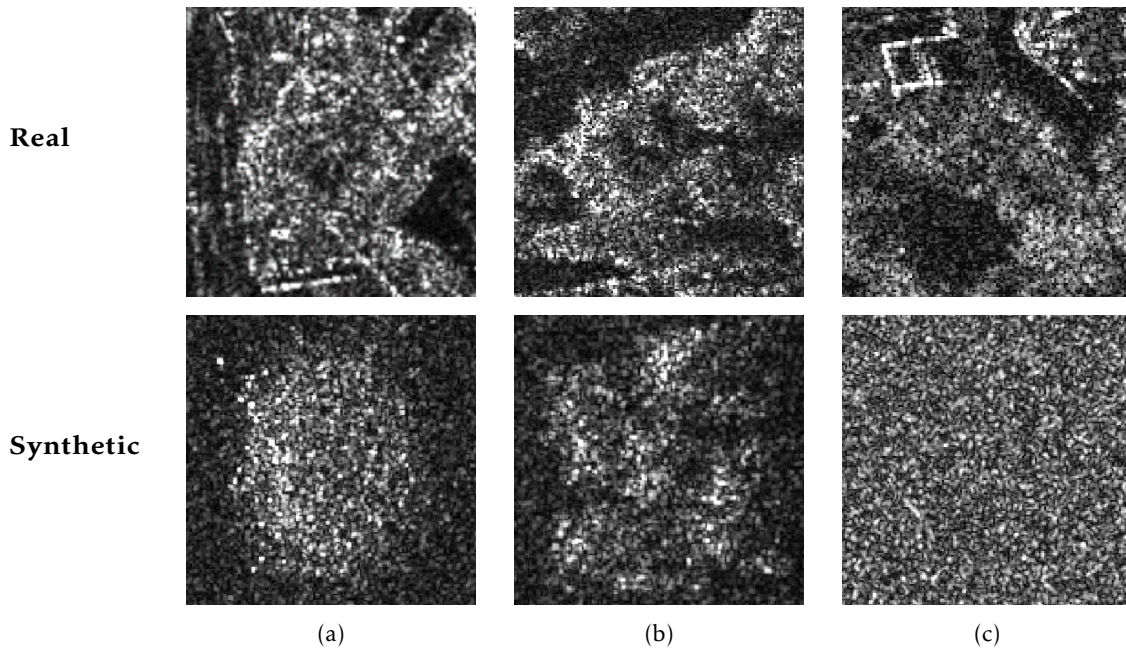
Figure 6.8.: Exemplary samples of real and synthetic textures regarding the classes a) debris, b) vegetation, and c) gravel.

6.1.4. Test samples

Test samples are not employed in the proposed work flow, however, they are used for a direct comparison of classification methods. They are acquired by manual extraction of 14 debris areas and several vegetation areas from the test area of the Christchurch TerraSAR-X image, using both the reference image and visual verification to make sure there is no blockage due to neighbouring buildings. These areas are then parcelled into 11 x 11 pixel samples, with Table 6.3 showing a summary. For the assessment of the classification performance, class gravel is not included for two reasons: The test area does not provide enough areas of reference signatures; secondly and more importantly, feature space has proven that debris and vegetation are much more entwined and thus classification performance is up to the separation of these two classes.

Table 6.3.: Test samples used for classifier performance assessment.

Class	Number of samples	Sample size [pixels]
Debris	1000	11 x 11
Vegetation	1000	11 x 11

6.2. Viability of synthetically generated signatures

The prospect of using synthetically generated training samples instead of real signatures relies on a realistic simulation and the accuracy of the signature characteristics. Before the debris detection algorithm is operated on the test data, it is prudent to ensure the viability of the synthetic signatures. The synthetic training samples for debris, vegetation and gravel were described in Section 5.2.1, whereas a set of test samples was introduced in Section 6.1.4. On the basis of these, the comparableness with regard to the feature set is explored.

6.2.1. Comparison of TerraSAR-X and simulated signature of debris

A visual comparison of synthetic and real samples shows a good accordance as can be seen in Figure 6.8, which depicts exemplary samples of the different signature types. More important, however, is a consistency in terms of the chosen feature set. On this account, the distributions of the feature values can give some
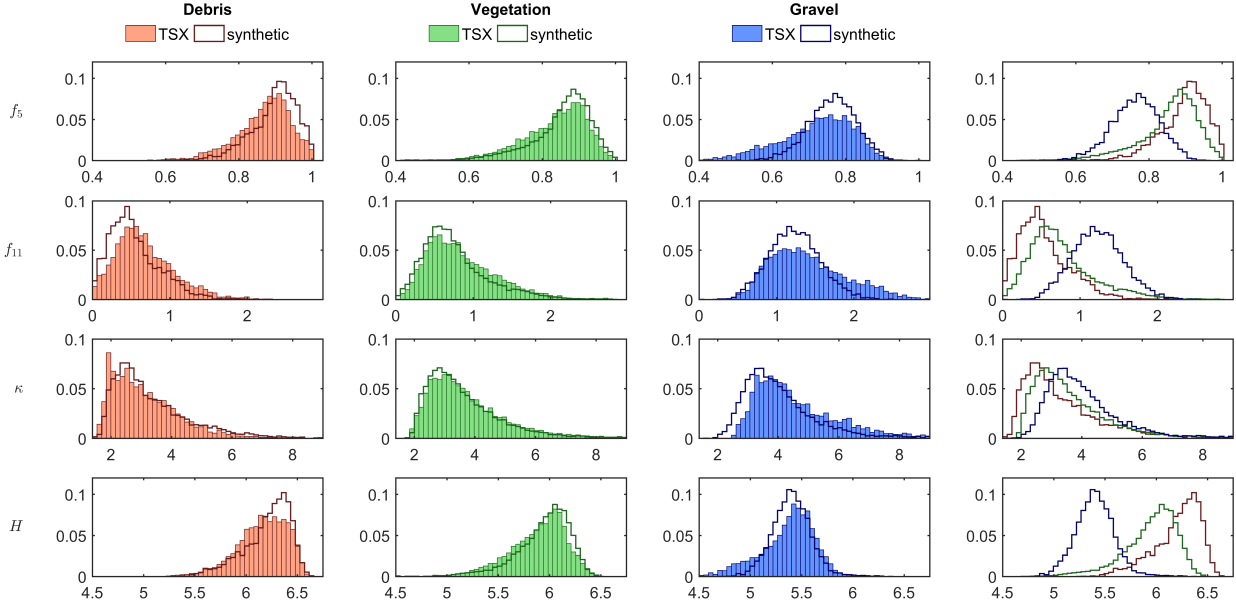
Figure 6.9.: Comparison of the feature distributions regarding TerraSAR-X samples and simulated samples for four exemplary texture features. Focus is on the three classes debris, vegetation and gravel (first three columns). The plots to the far right combine the simulation-based histograms and demonstrate the feature-specific sensitivity towards the difference between the three signature types.

information as to how well the simulations imitate the real SAR texture. Even though the feature distributions cannot prove the correctness of the simulated signature, they are an indication for a realistic simulation. In Figure 6.9, the normalised histograms of four exemplary features are plotted together for the TerraSAR-X samples and for synthetic samples, taking up each class (debris, vegetation, gravel) separately. For each, the two bar charts show good agreement between the feature distributions of simulated and real samples. The histogram similarity is quantified by the euclidean distance D_e, which is calculated as

$$D_e = \sqrt{\sum_{i=1}^{n}(h_{tsx_i} - h_{sim_i})^2} \,, \tag{6.1}$$

where n is the number of bins and h_{tsx_i} and h_{sim_i} denote the histogram bin counts of the real and simulated feature distributions. Accordingly, an accurate simulation manifests itself in a similar feature distribution and thus in a small distance D_e. Table 6.4 lists the distances D_e for the entire feature set. It can be observed that the feature distributions of vegetation in particular are very conform (average distance over all features $\tilde{D}_{e,Veg.} = 0.037$). In comparison, gravel and debris show a small but distinct discrepancy ($\tilde{D}_{e,Gravel} = 0.069$,

Table 6.4.: Euclidean distance D_e between feature distributions (histograms) of TerraSAR-X and simulated samples.

|	$D_{e,Debris}$	$D_{e,Veg.}$	$D_{e,Gravel}$			$D_{e,Debris}$	$D_{e,Veg.}$	$D_{e,Gravel}$
f_1	0.061	0.037	0.063		μ	0.039	0.026	0.061
f_2	0.066	0.035	0.081		σ^2	0.033	0.025	0.089
f_3	0.072	0.023	0.037		σ	0.032	0.024	0.088
f_4	0.065	0.034	0.079		κ	0.046	0.025	0.067
f_5	0.059	0.041	0.063		γ	0.034	0.024	0.061
f_6	0.062	0.036	0.073		H	0.050	0.037	0.052
f_7	0.060	0.036	0.071		$\tilde{x}$	0.065	0.051	0.094
f_8	0.065	0.035	0.055		x_{max}	0.134	0.124	0.156
f_9	0.059	0.036	0.055					
f_{10}	0.060	0.037	0.061					
f_{11}	0.062	0.033	0.055					
f_{12}	0.076	0.031	0.039					
f_{13}	0.068	0.034	0.048					
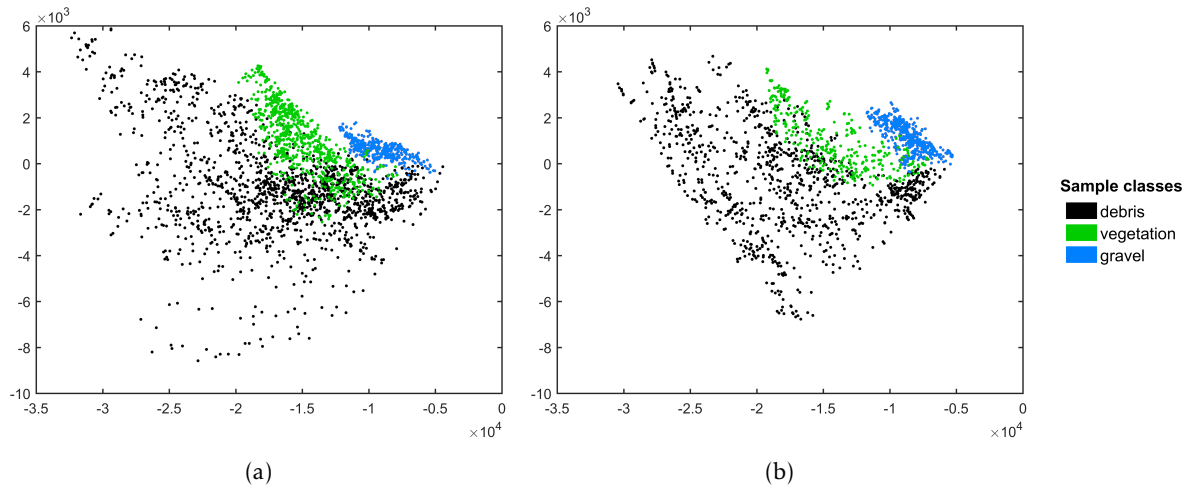
Figure 6.10.: Feature clusters (Sammon mapping) of the signature of debris (black), vegetation (green) and gravel (blue); a) regarding real samples and b) regarding simulated samples.

$\tilde{D}_{e,Debris} = 0.060$). This may be explained by the small range of texture variations regarding real vegetation in comparison to the signature of debris and by the good signature representation of the vegetation test samples. As for the signature of gravel, the assumption that an accurate simulation can be achieved using a flat plane may be at its limits and the cause of a somewhat less correlating feature distribution. In total, however, the deviation of the individual feature distributions is small for all three signature types, thus providing a first indication of a successful simulation. To demonstrate the feature-specific sensitivity towards the difference between the three signature types, Figure 6.9 combines the simulation-based histograms in the column to the far right. Throughout the whole set of features this sensitivity varies strongly, from closely overlapping distributions to showing a distinct difference between the three signatures. A more substantial validation is attainable by a comparison of the projected features. In the context of discriminant analysis (Section 5.2.4), the separability of the three simulated classes debris, vegetation and gravel was visualised with a Sammon projection. The corresponding plot using the test samples (TerraSAR-X samples) instead of the simulated samples is shown in Figure 6.10(a), with Figure 6.10(b) reshowing the Sammon projection regarding the simulated samples for the purpose of comparison. The two plots have the same scaling range, so that a direct comparison is possible. Minor differences can be observed between the two plots. The simulated texture of debris yields rather compact feature clusters, whereas the real texture demonstrates several peculiarities. This can be attributed to the fact that it is represented by a rather small number of real debris occurrences that feature quite diverse characteristics. In the synthetic sample generation the range of characteristics can be covered more evenly. All in all, however, each class shows rather good accordance for simulated and real samples, thus ruling out grave errors in the texture simulation.

6.3. Debris detection performance

The algorithm that was described in detail in Chapter 5 was executed on the post-event SAR image specified in Section 6.1. In the following, the results of the individual processing steps are presented, and a discussion is provided at the end of the section. A test area was specified in Section 6.1, defining a cut-out of the post-event SAR image. According to that, all results shown in the following refer to this cut-out scene, masking out the surrounding area.
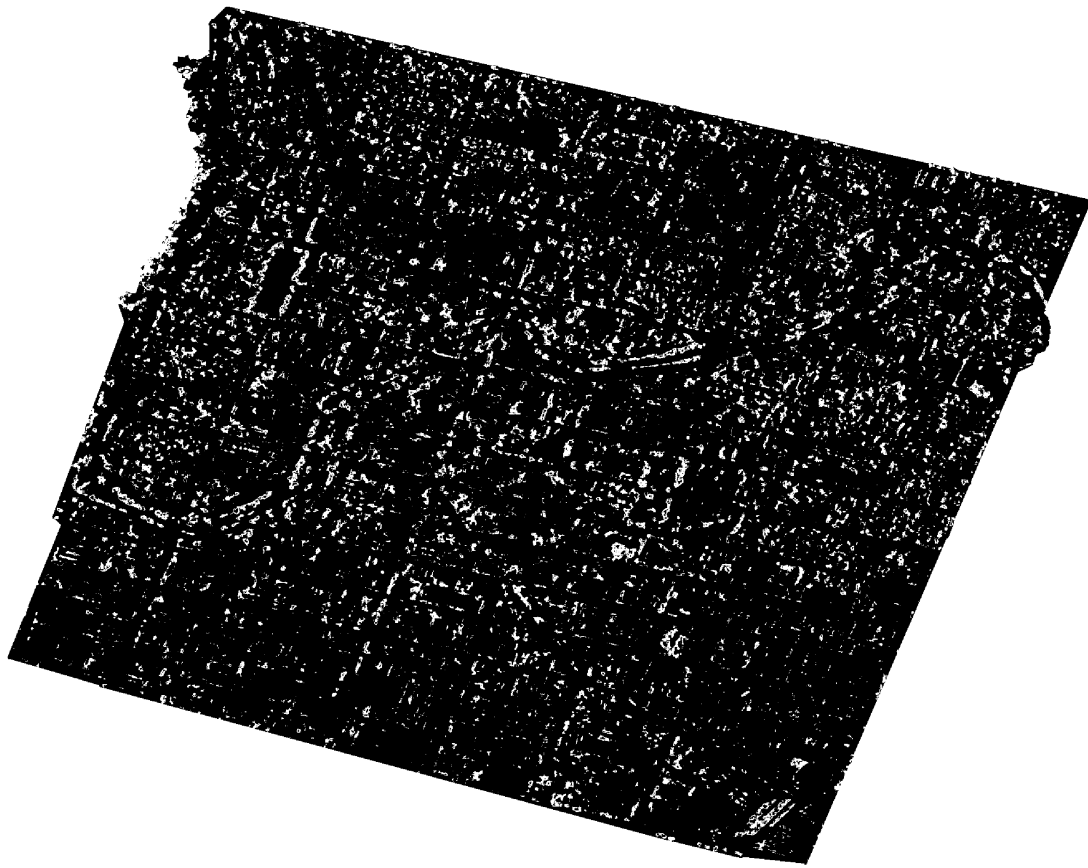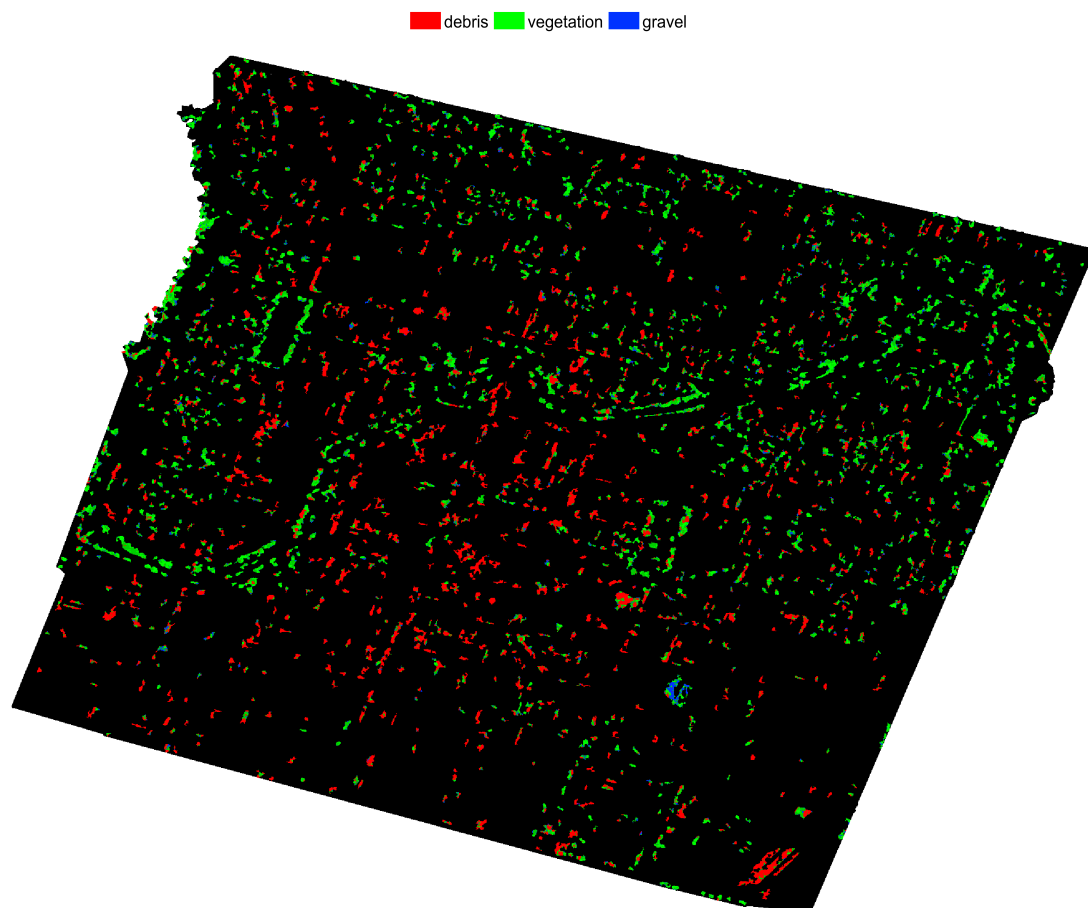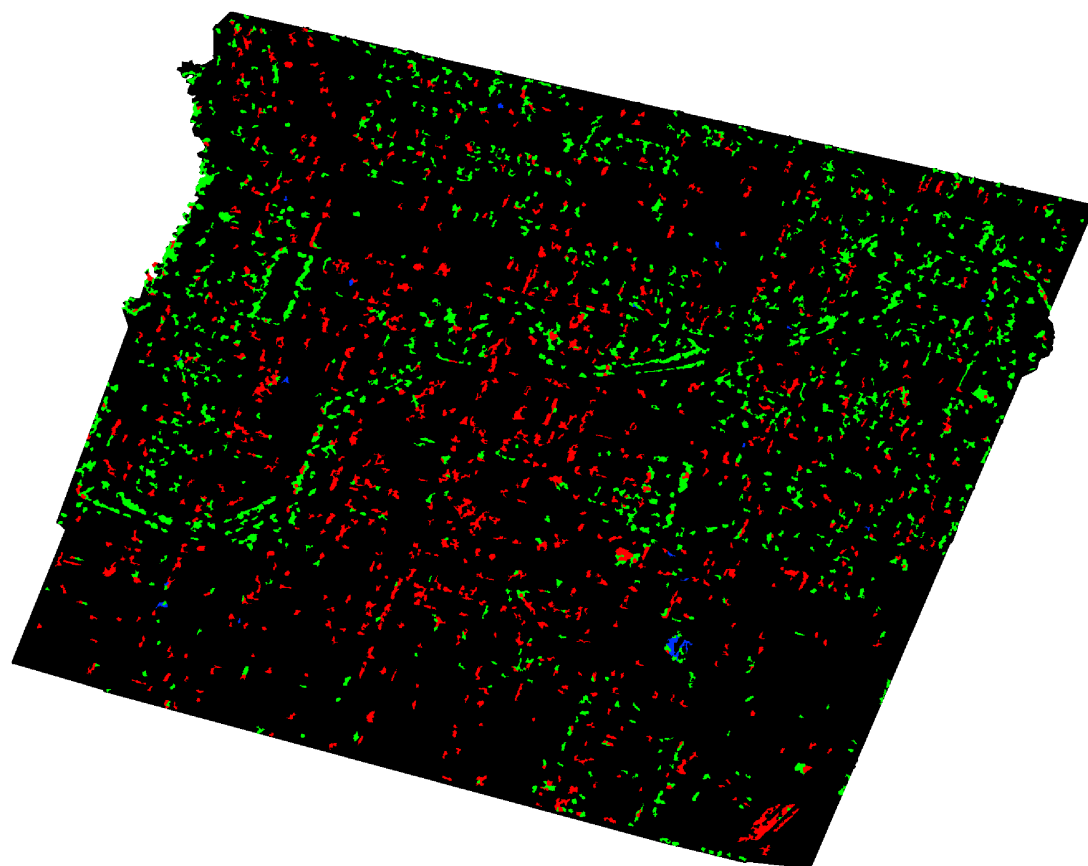
(a)
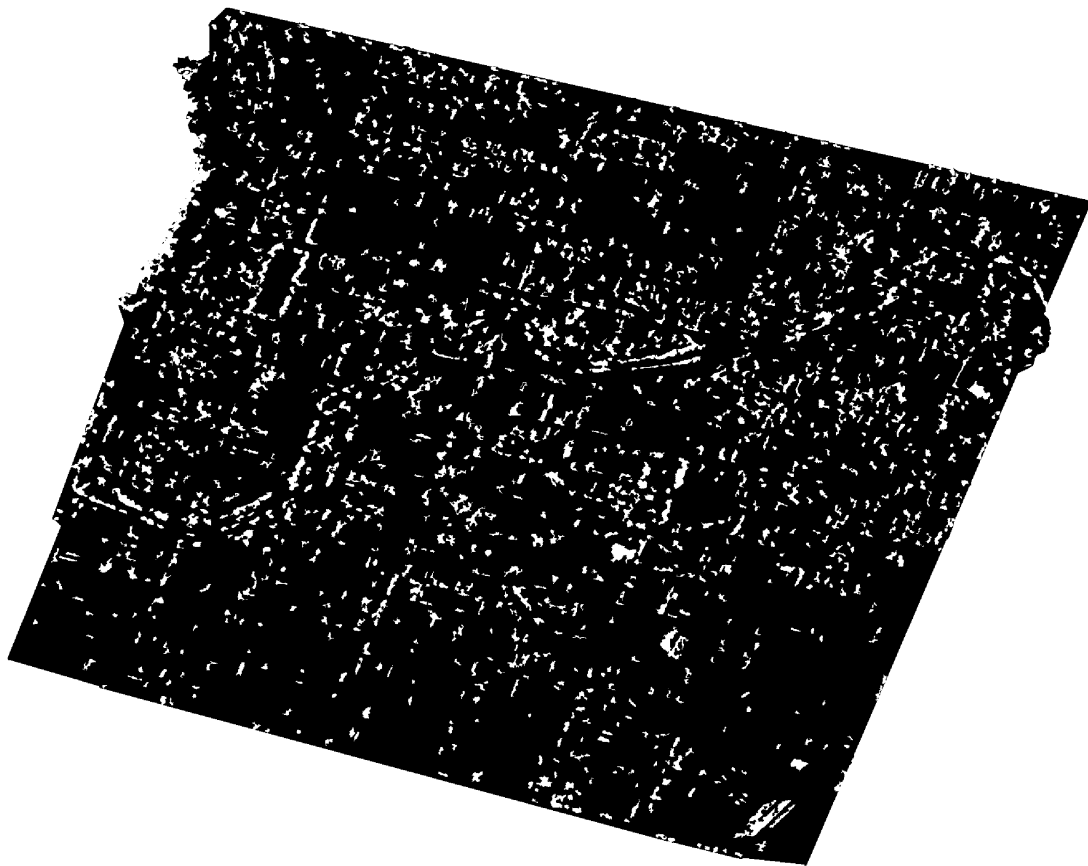
(b)

Figure 6.11.: Screening result for the test area a) unprocessed, b) after component-wise filtering (morphological closing, dropping small components).

(a)

(b)

Figure 6.12.: Predicted classes debris (red), vegetation (green) and gravel (blue) for a closed world scenario; a) pixel-wise classification and b) after component-wise majority voting.

6.3.1. Results of detection algorithm on Christchurch test area

Screening   The screening procedure and its aim to isolate areas of debris-like texture was described in Section 5.3 and was applied on the introduced test area. In Figure 6.11(a), an overview of the resulting unprocessed screening mask is displayed, containing also numerous areas constituting of single pixels or very small cumulations. Correspondingly, Figure 6.11(b) depicts the filtered mask as the result of morphological closing and after dropping small components. The final screening mask describing all areas of debris-like texture, shows a total area of 599.000 pixels, thus narrowing down the working area to less than 7% of the test area. It comprises a total of 1572 components, which aside from debris are caused by similar textures such as mainly the already identified sources: vegetation and gravel.

Classification   The aim of the classification process, which was described in Section 5.4, while using a closed world assumption, is to exclude areas of known texture similarities. Applied on the areas defined by the screening mask, the classification yields the pixel-wise predicted classes debris, vegetation and gravel, shown in Figure 6.12(a). Correspondingly, Figure 6.12(b) depicts the final component-wise classes as a result of the post-processing operations with component-wise majority voting. The predicted class *debris* contains a total of 822 components with class *vegetation* and class *gravel* comprising 1059 and 19 components, respectively. Note that the sum of the components does not match the number of inbound screening components. This is due to the fact that the transformation of pixel-wise to component-wise classification allows for the splitting of screening components.

6.3.2. Exemplary details

For several areas of interest (AoI) a more detailed account of the screening and classification results is provided in the following. Screening and classification results regarding these AoIs, as well as the corresponding cut-out of the TerraSAR-X scene and the reference map are depicted in Table 6.5.

AoI 1   contains a large debris site pictured in Figure 6.13(a). The site is in full line of sight of the SAR sensor and is the result of a fully collapsed building. As such, it can be categorised as building damage type 7 (see Section 3.2). According to the reference map, the site covers almost 2000 m^2 (3474 pixels) with almost no remaining vertical elements at the scene. Examining the screening and classification results versus the reference map in Table 6.5 (first row), several observations can be made. The algorithm results for this area show that the major part of this large debris site was found in the screening process, also catching some of the surrounding smaller debris sites. Apart from these areas, the screening result contains also several areas that belong to non-debris sources, most prominently the vegetation area in the upper right corner. The predicted classes show that these areas of high vegetation are distinguished rather well by the trained classifier, even separating single trees that are located adjacent to debris. While a certain loss regarding actual debris can be observed, most of the large debris site is classified correctly, as well as the elongated site on the opposite side of the road, representing heaps of debris in front of a still standing building.

AoI 2   is a second site of debris, pictured in Figure 6.13(b), where a building block is affected on multiple sides. Contrary to AoI 1, this site is not entirely in line of sight of the sensor, but shows some shadowing for the far side of the building block. Nevertheless, most of the debris area is displayed and detected in the screening process alongside several non-debris textures (Table 6.5 (second row)). Most of the non-debris areas can successfully be separated as vegetation.
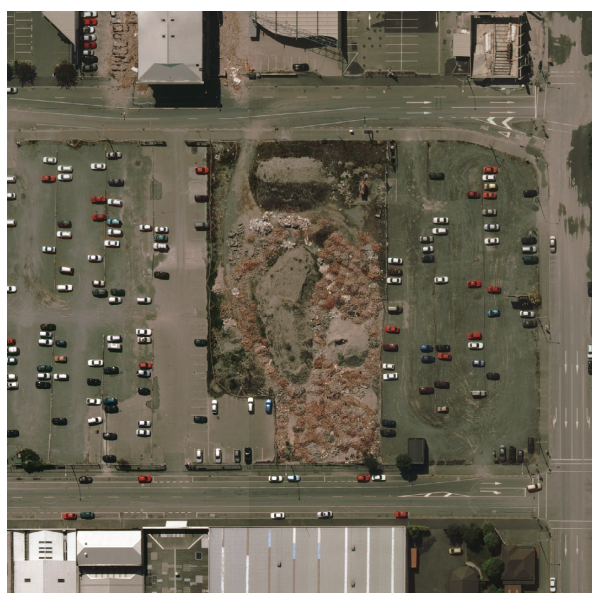
AoI 3   is a large dump site of what appears to be numerous heaps of construction waste in the form of small-sized rubble and as such was labelled class gravel in the reference map rather than class debris. In Figure 6.13(c) a close-up of this site is depicted. Since large areas of gravel are not common in urban zones,

(a) AoI 1 (debris site).

(b) AoI 2 (debris site).

(c) AoI 3 (construction dump site).
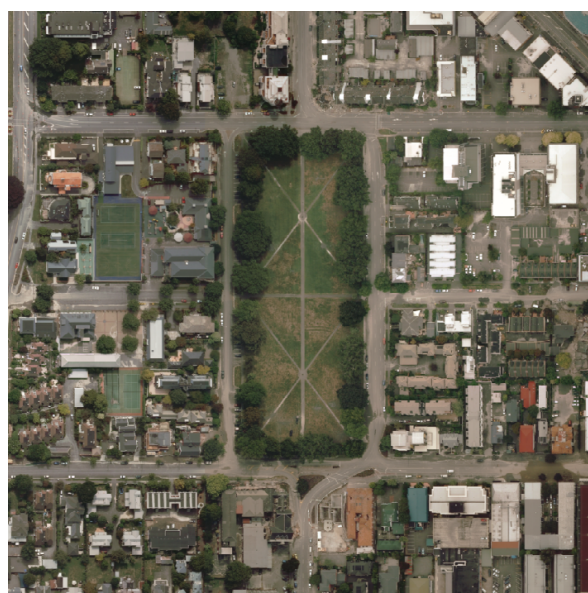
(d) AoI 4 (park area).

Figure 6.13.: Details of four areas of interest (RGB orthophoto).

Figure 6.14.: AoI 5: Typical case of debris occurrence located in shadow area of building (orthophoto rotated so that range points from left to right).

Table 6.5.: Detailed results for four areas of interest.

| TerraSAR-X image | Reference map | Screening mask | Classification result |

Table 6.6.: Detailed results for debris in shadow area.

| TerraSAR-X image | Reference map | Screening mask | Classification result |

this site represents the only incidence of the label gravel in the test area that is large enough not to be filtered out due to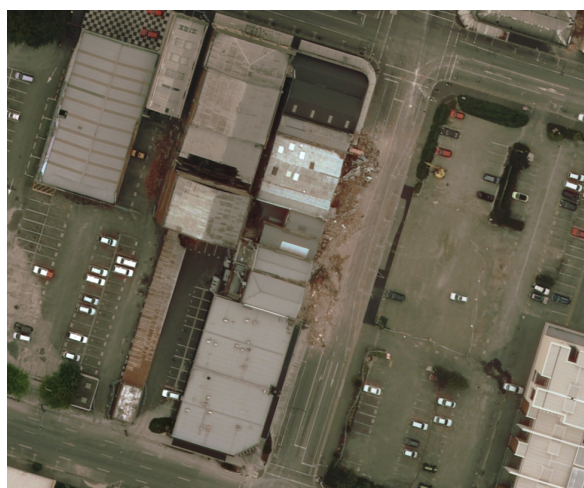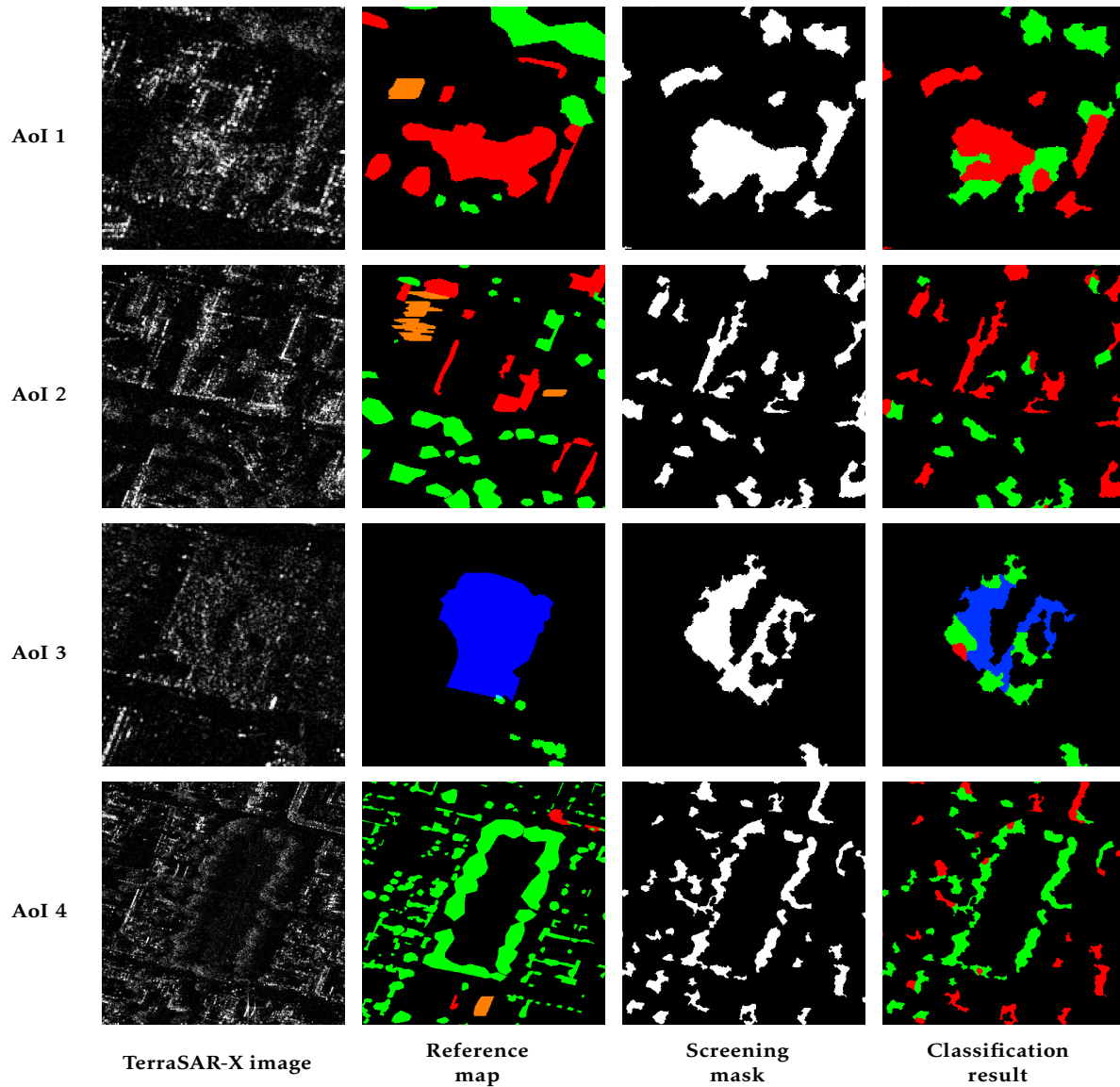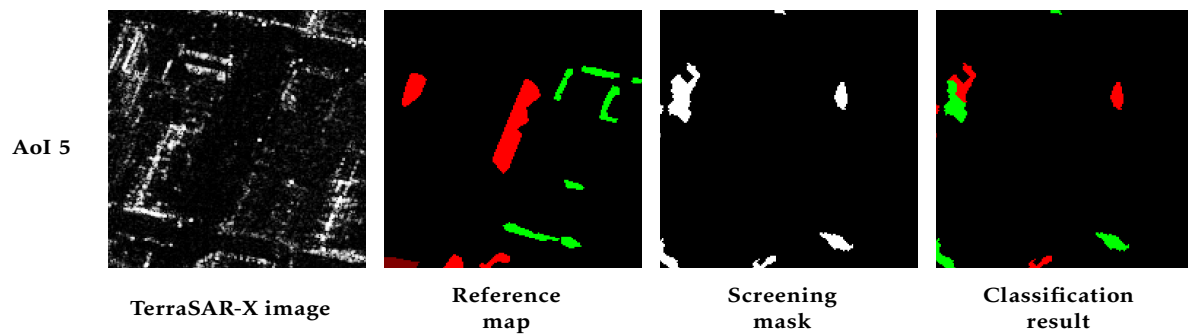 size. The screening finds a large part of this dump site to be of a debris-like texture, as can be seen in Table 6.5 (third row). The trained classifier is successful in distinguishing between this sort of small-sized rubble and debris and predicts this area for the major part to be gravel.

AoI 4 specifies a rectangular park area framed by high trees and surrounded by residential housing. An optical image detail is provided in Figure 6.13(d). It can be observed in Table 6.5 (fourth row) that large enough vegetation, such as the park area, is almost entirely included in the screening mask, but can be separated effectively by the classifier. Further, this area can demonstrate the two main difficulties involving residential areas. As is common for residential areas, there is much vegetation that is rather small but wide-spread. Secondly, there are many small-scale constructions, such as balconies and backyard structures, which for the resolution at hand can lead to a texture similar to that of debris. These incidences located in close proximity result in screening components that are large enough not to be disregarded in the filtering step. Consequently, this results in a large amount of screening components, which due to the closed world assumption without reject option cannot be classified correctly.

6.3.3. Limitations of reference map

In Section 6.1.2 the generation of the reference map was described, involving debris (ground-level and higher-level) as well as vegetation and gravel. The thus generated reference map has several weak points, leading to a limited aptitude regarding the use as evaluation quantity.

Shadowing of the scene

The typically flat incidence angle ($\theta = 47.38°$) of the SAR image acquisitions leads to a considerable amount of shadowing, particularly in areas of high building development such as in the test scene. As a consequence, there are many debris occurrences that are located partly or entirely in the shadow of a building. The reference map, however, as independent data set, does not provide this information. Figure 6.14 visualises **AoI 5**, an example of a debris occurrence located completely in the shadow area of a building and thus producing a non-detection in the screening step (see Table 6.6).

A quantitative evaluation necessitates an assessment regarding the extent of shadowing in the test scene, or rather an estimate of the rate of debris occurrences that are not in line of sight of the sensor. For this purpose, the shadow mask introduced in Section 6.1.3 is used to assess the approximate percentage of debris occurrences affected by shadowing. As a matter of course, this approach neglects the case of reduced shadowing due to the collapse of buildings. However, quantitatively, these incidences are considered scarce enough to be disregarded here. Since the 3d city model covers the test scene only partially, a representative cut-out of the scene (approximately 0.3 km^2) was defined (see Figure 6.15) for an assessment of the shadowing rate regarding ground-level debris occurrences. The shadow mask for this area reveals that for the acquisition geometry in question, the shadow coverage amounts to a total of 38.0% of the cut-out scene. Figure 6.16(a) shows the shadow mask of this cut-out of the test scene overlayed with the reference mask of the ground-level debris, thus marking areas (yellow) that refer to debris occurrences located in the shadow areas. According to this, a total of 54.7% of the ground-level reference debris occurrences are not in line of sight of the sensor, and consequently cannot be detected using this acquisition geometry. For the quantitative evaluation, the consequences are bound to be significant. It is to be expected that an approximate of 55% of the reference ground-level debris components cannot be detected in the screening process. However, this concerns only the 217 reference debris components on ground level; for the 130 components on higher level, shadowing is assumed to be no problem. Theoretically, for steeper incidence angles the shadow coverage is lower, however, this comes with the downturn of a decreased ground range resolution and longer layover areas. The impact of the layover

Figure 6.15.: Cut-out used for the assessment of the shadowing and layover rate for ground-level debris occurrences.

effect on the debris texture may not be as substantial as shadowing, but still can alter the texture significantly. In Figure 6.16(b) an overlay of the reference components with the layover mask is depicted, showing (yellow) reference debris areas that are affected by layover of a neighbouring building. These areas amount to a total of 32.3% of the reference debris areas in this scene.

High vegetation

The use of two average tree heights (5 m and 10 m) for the transformation of reference vegetation components into the SAR image geometry is straightforward but brings along a certain inaccuracy. Considering that a height error of 0.67 m results in a faulty shift of one pixel and assuming that the average height error is about 1.25 m, the average range location error of vegetation is about 1.9 pixels. In proportion to the targeted debris sizes, this error is rather small and the consequence for the quantitative evaluation is hence deemed minor.

Higher level debris

Just as the shift of high vegetation, the stretching of the higher-level debris components for the purpose of geometry transformation is imprecise. For one, debris at a height of more than 13 m is not accounted for. Secondly, the stretching covers a shift of up to 20 pixels and thus the size of the reference component is significantly larger than the actual occurrence. Since the decision rule, whether a reference debris component is declared *detected* or *not detected*, is based on both, absolute number of pixels and percentage of debris area,
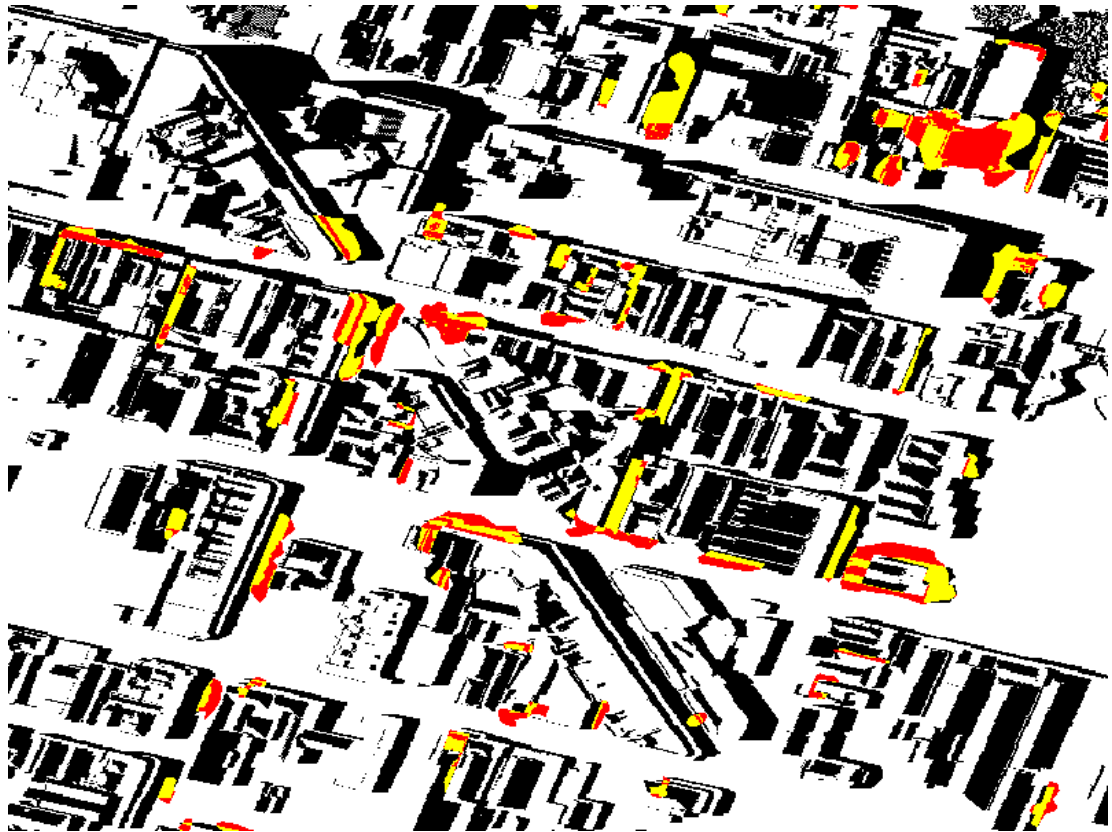
(a)
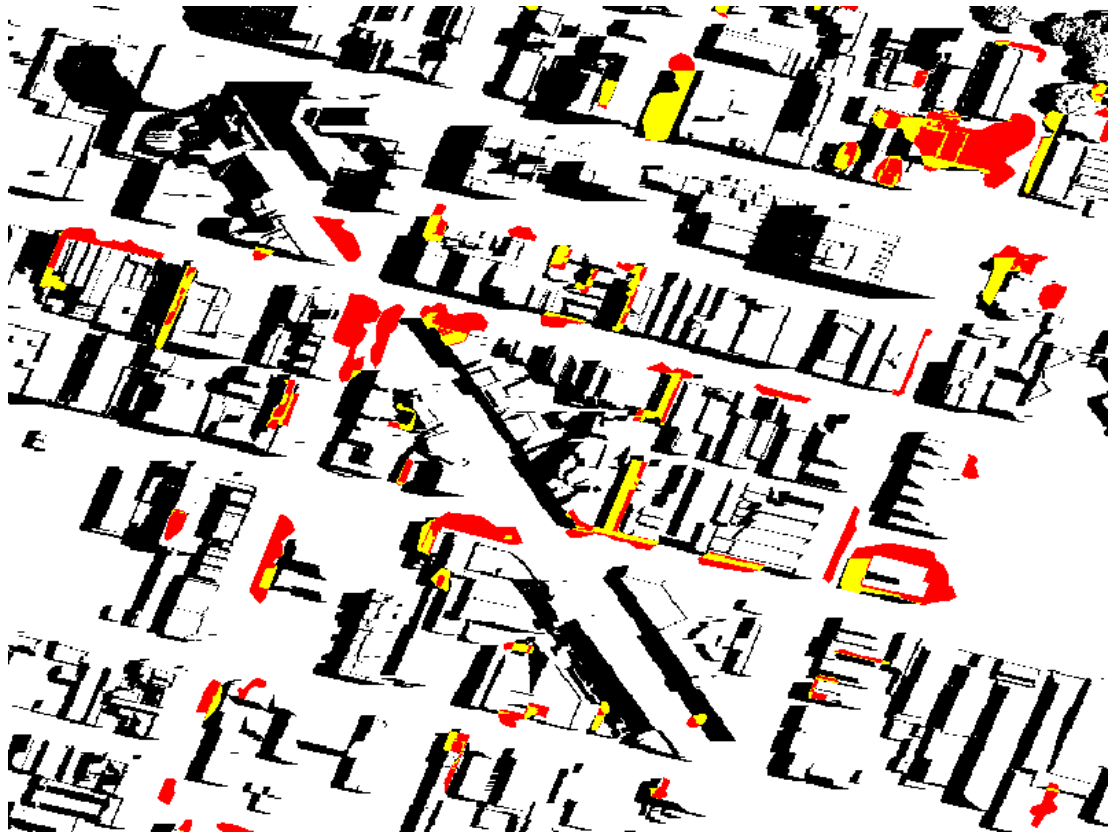
(b)

Figure 6.16.: Cut-out of ground-level reference debris (red) in slant range geometry overlayed with masks (black) derived from 3d city model: a) shadow mask and b) layover mask (yellow denotes overlapping areas).

this may affect the quantitative evaluation perceptibly. Thus, depending on the form of the debris occurrence and the resultant increase in size, there may be cases where the algorithm detects the higher-level debris, but the detection rate does not reflect it.

6.3.4. Quantitative evaluation

Based on the reference map and a decision rule, a quantitative evaluation is conducted both for the screening results and for the classification results of the test scene.

Detection rule for reference components

The decision whether a debris component of the reference map is determined as being detected is defined as follows: For each reference debris component a pixel count is conducted regarding the predicted classes contained in this area. The component is declared *detected*, if there is a minimum count of 20 class debris pixels and if these amount to at least 10% of the reference component. Otherwise, the reference components are proclaimed *undetected*.

Detection of reference debris components

Employing the described decision rule, a screening detection rate is computed regarding the introduced set of 282 debris reference components. Effectively, the screening mask includes 128 of these components, which amounts to 45.5%. Considering the estimated 55% shadowing rate of ground-level debris occurrences, this is a fairly satisfactory rate. Hence it is warranted, that the screening mask provides a good coverage of debris occurrences in line-of-sight of the sensor. In Figure 6.17(a) the reference debris components are depicted, subdividing into those that were detected in the screening process (black) and those that were not detected (grey). The classification of these 128 components led to 85.2% being classified correctly as *debris*, which corresponds to 37.7% of the entire set of reference debris components. Figure 6.17(b) shows the location of these detected components (black), whereas Table 6.7 summarises the reference components and their detection rates regarding the process of screening and classification.
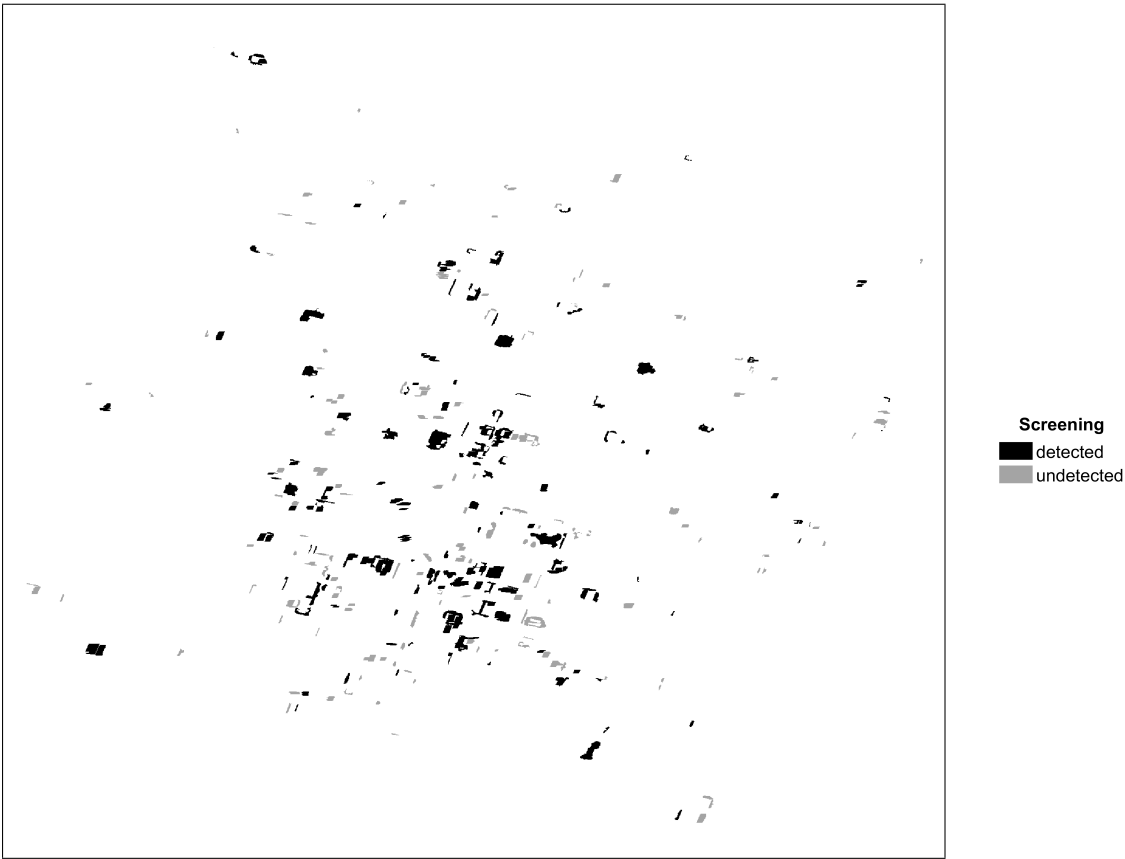
Classification results

For an assessment of the classification process, a confusion matrix is analysed, which is based on the components of the screening matrix. Table 6.8 shows this confusion matrix regarding the true classes *debris*, *vegetation*, *gravel* and *other* as labelled in the reference map, where *other* denotes areas that are unspecified in the reference map, thus appertaining to signatures of unknown source. For a definition of the evaluation measures used in the following see Section 2.2.2. Be reminded that the number of components in the confusion matrix does not match the number of inbound screening components.

Since the true classes of the screening map areas are highly imbalanced, with 150 debris instances, 1254 vegetation instances and only 7 gravel instances ACC is not an ideal evaluation measure and as such is not included in the table. A far more useful depiction of the confusion matrix is given by TPR, PPV and the F_1 score. The TPR of the classes *debris* and *vegetation* shows (with 72.7 % and 71.1 %) a rather high percentage of correctly classified instances, whereas the PPV values reflect the fact that a significant number of vegetation instances

Table 6.7.: Detection rate of reference debris components.

	Components		
	found	not found	Detection rate [%]
Screening	128	154	45.5
Classification	109	173	37.7

(a)
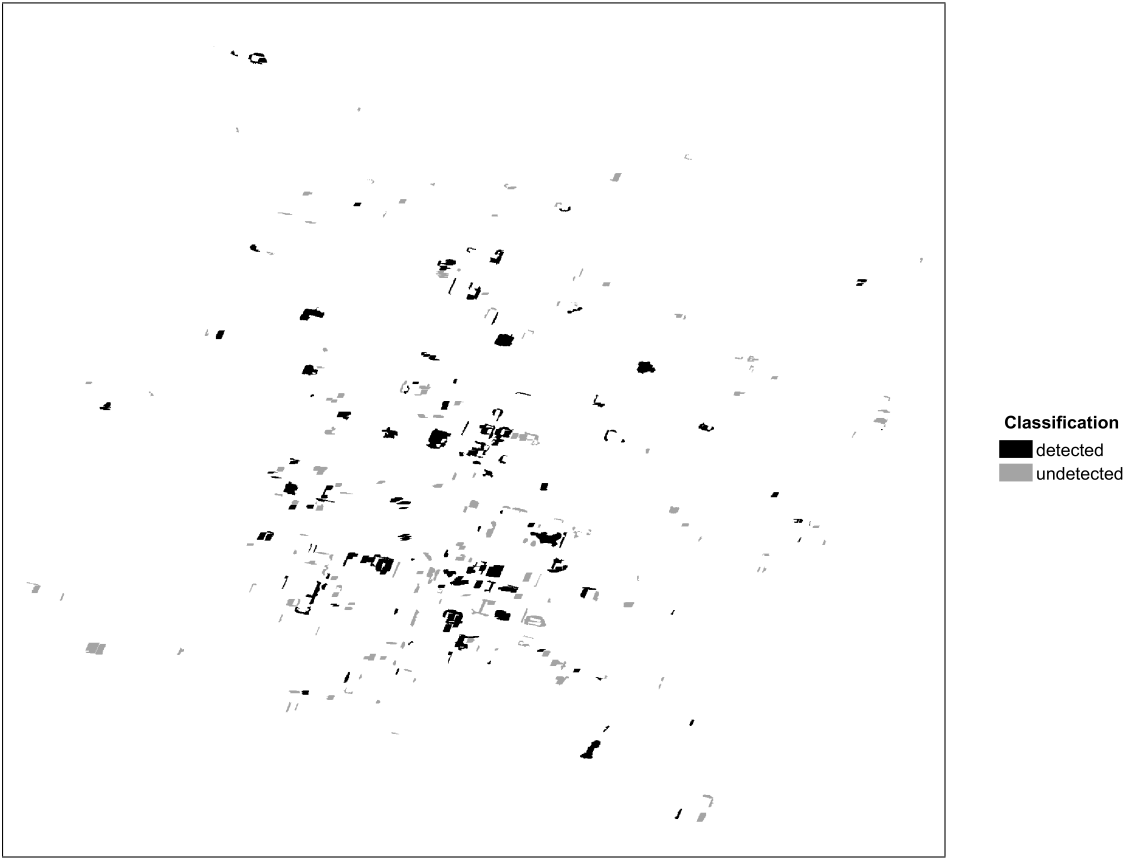
(b)

Figure 6.17.: Reference debris components subdivided into those that were detected (black) and those that were not (grey) in a) the screening process and b) the classification.

Table 6.8.: Confusion matrix.

		Predicted class			TPR [%]	PPV [%]	F$_1$ score [%]
		Deb	Veg	Gra			
True class	Debris	109	41	0	72.7	13.3	22.5
	Vegetation	356	899	10	71.1	84.9	77.4
	Gravel	0	4	2	33.3	10.5	16.0
	Other	357	115	7			

was falsely classified as debris. The rather low number of 13.3% PPV for class debris, however, is condoned in order to have a high TPR value in return since the cost of misclassified debris instances is ranked much higher than cost of instances falsely classified as debris. Though the rates for class *gravel* seem rather low and are debatable due to the very low number of gravel instances, it is to be noted that misclassification cases seem to predominate between the classes gravel and vegetation, whereas the separation from debris is successful.

6.4. Discussion

In this section some aspects of the methodology, including some decision making steps are reviewed with regard to the introduced aims of this thesis. Further the prospect of transferability is discussed.

6.4.1. Methodology

The proposed methodology is motivated by an operational use in the emergency case and as such, the computational cost is a relevant factor. The pixel by pixel computation of the GLCMs is the most costly aspect, so that the 4000 x 3200 pixel TerraSAR-X cut-out (test area) took about 6 hours to compute while using 16 grey levels and even 17 hours using 64 grey levels (using a standard desktop computer equipped with an Intel$^{(R)}$ Core$^{(TM)}$ i7-6700 CPU @ 3.40GHz processor (4 cores), 64-bit architecture, and a Windows 10 operating system). However, it is to be taken into account that the optimisation of the computational performance was considered of low priority, after all this processing step did not require to be executed repeatedly. Since much research has been devoted to fast methods of GLCM computation ([37, 16]), the high computational cost is not considered an actual operational problem.

The motive to conduct the damage detection steps (feature extraction) on slant range imagery rather than in ground range geometry was that it reflects the direct results of the radar measurement. The process of ground projection consists of a resampling to account for significantly differing local incidence angles in near and far range (e.g. occurring in large scenes or in airborne data), or in the simplest case solely to obtain quadratic pixels. Either way the resampling step interferes with the image statistics/ radiometry, which was considered important to retain.

Regarding classification, the random forest is known to perform quite well compared to other classifiers, while requiring little and straightforward tuning. Further, for the classification problem at hand, the robustness towards features of different scales as well as the robustness towards correlated and noisy features is fairly beneficial. This renders it suitable for the task at hand and hence was chosen for this algorithm. To verify the suitability of the random forest classifier for this approach, two very powerful classifiers (namely SVM and CNN) were also considered. A direct comparison of model performances revealed that both alternative classifiers achieve a similar classification rate, but neither of them can surpass the performance of the random forest approach. The direct comparison of model performances is demonstrated in Appendix A.

The success of a closed world assumption in the framework of this classification depends on the extent of unspecified texture that is included in the screening map. High vegetation and gravel were identified as sources of similar texture, whereas no distinct further class could be made out. A visual investigation suggested that

much of the texture falsely classified as *debris* originates from indefinite small-scale structures, such as gardens and balconies, where the mix of different kinds of small-scale objects and vegetation in conjunction with the given resolution of the SAR image apparently cannot produce distinctive textures. Regarding the whole test scene, it was observed that by comparison the inner city area performs distinctly better (shows less false detections) than the suburban areas due to the lack of such structural conditions. It can be argued that the approach is less suited for densely built-up areas such as suburbs. However, since the aim of the methodology is the detection of large heaps of debris, where the most trapped victims are expected, the focus is not on suburban areas but on areas such as the city centre.

6.4.2. Transferability

A vital trait of a damage detection method is its transferability to different kinds of data. Hereby, several aspect are of interest and are discussed in the following.

Given the same sensor, a different acquisition geometry principally is considered unproblematic, since the methodology uses calibrated data. The radiometric calibration minimises amongst other things the radiometric differences caused by the acquisition geometry and thus the influence of a differing local incidence angle (assuming a flat earth). It is expected that for substantially differing incidence angles the texture of debris changes, since calibration does not take into account factors regarding the targets themselves. However, the methodology provides the means to adapt by straight-forwardly re-simulating the training data set for the relevant incidence angle, using the established set of 3d models and backscattering properties and a subsequent adjustment of the screening feature intervals.

For imagery of different SAR sensors, factors such as the resolution and the frequency band are relevant. The radiometric calibration theoretically can account for sensor specific influences and the image processing. As a consequence, a transferability to other sensors is plausible, provided the resolution and frequency band are similar. The prospects of applying the methodology on imagery of substantially different resolutions/ frequency bands, however, is considered problematic. It is expected that, as the presented results on X-band imagery (1 m resolution) already indicate, for a lower resolution, the individual heap of debris does not produce the minimal pixel count required for the detection method to be effective. Rather, the minimal size of potentially detectable heaps of debris would be unrealistically large. Accordingly, it is assumed that for imagery of a higher resolution the performance of the methodology is improved with regard to the detectability of small heaps. A potential influence on the texture due to the changed resolution, can once again be accounted for by a re-simulation of the training data set. Further, wavelength-specific signature differences are also a factor to be considered. The differing backscattering mechanism of X-band, C-band and L-band for the example of vegetation was already established in Section 4.3.1. The involved difference in signature could potentially eliminate vegetation from the list of debris-like texture, yet bring forward other unknown sources of similar texture. This, however, is beyond the scope of this work.

A transferability to arbitrary urban locations around the world requires the consideration of culture-bound construction methods. The introduced methodology was developed for industrialised countries of a European character on the grounds that predominant building materials and consequently the heaps of debris are comparable. This raises the question, whether the methodology can be transferred to countries such as e.g. Japan, where construction methods and building materials may differ. Two aspects need to be considered: firstly the buildings are bound to yield different damage types and secondly the heaps of debris may feature different characteristics. Hence, an application of the methodology in such locations would possibly require an adaptation regarding the 3d modelling of heaps of debris and possibly the backscattering properties.

Due to the far-reaching use of vegetational texture within the presented methodology, another matter to be considered is the transferability regarding different seasons of the year and the involved phenological changes.

After all, fully foliated trees in summer, as is the case for the Christchurch test area, lead to a different backscattering mechanism than defoliated trees in winter. For the methodology it is relevant to know whether or not the proposed set of texture features is stable throughout the year. For this purpose a study was conducted regarding the influence of phenological changes of high vegetation on the texture features, which established a measurable seasonal influence regarding a part of the feature set. Corresponding findings are presented in Appendix B.

Chapter 7.

Conclusion and Outlook

7.1. Conclusion

The aim of this thesis was to provide a new method to perform damage detection on solely a post-event HR SAR image and using simulated SAR signatures as means to obtain a capable training data set. With this in mind, the SAR signature of damaged buildings was analysed, differentiating between a set of commonly occurring damage types. Conclusions were drawn for the detection of damages in a post-event HR SAR image only: firstly, the signatures of most damage types do not provide distinct enough characteristics to allow for a damage type specific detection of buildings (a higher resolution would provide valuable additional information); and secondly, debris poses the most prominent aspect of damaged buildings, hence suggesting the use of simulated debris textures as means to conduct damage detection.

The process of simulating realistic SAR signatures of heaps of debris that meet the demands of a direct comparison to real signatures was described, with the point of producing a capable training data set. Firstly, this includes the process of generating 3d models of heaps of debris that feature a realistic macroscopic surface roughness. A point was made of providing a full scope of possible types of debris by generating model sets of varying surface roughness. And secondly, this includes the process of producing realistic backscattering characteristics in order to achieve a realistic radiometry. This involves the imitation of materials commonly found in heaps of debris that are the result of building collapses.

Following, an algorithm was introduced that is based on the simulated training data set and provides the means for debris detection. The core of the algorithm consists of a series of processing steps:

- Pre-processing involving radiometric calibration and dynamic scaling

- Feature extraction using statistics of the first and second order

- Definition of feature intervals representing the characteristic feature range of debris

- A screening step based on the feature intervals providing a map of potential areas of debris

- Pixel-wise random forest-based classification as a means to separate debris from similar textures

- Post-processing steps involving the conversion into a segment-wise classification result

A suitable set of texture features was identified, and where necessary, the aptitude of parameter settings was discussed and put to the test. In the context of feature extraction a discriminant analysis was conducted in order to determine the relevancy and redundancy of the feature set. The characteristic feature range for typical debris textures was investigated by methodically exploring the influence of underlying factors such as the macroscopic surface roughness and the backscattering properties. Based on these findings, the screening step was conducted resulting in a map of areas featuring a debris-like signature. High vegetation and gravel were identified as the main sources of misinterpretation due to their strong textural similarity to debris. With a classification in mind, the process of simulating training data was repeated for the two additional classes. The potential for a successful separation of the three classes debris, vegetation and gravel was examined using a multidimensional scaling to comprehend the class representation in feature space. Finally, the training of a

random forest classifier and the post-processing steps were described (an independent performance comparison with two other classifiers was able to confirm the aptitude of the random forest classifier for this task). Subsequently, prospects and limitations of the methodology were discussed.

A data set of earthquake-ridden Christchurch, New Zealand, was introduced, which consists of a post-event HR Spotlight TerraSAR-X image and a debris reference map that was manually extracted from airborne optical imagery and transformed into SAR geometry. The limitations of the debris reference map were discussed and an investigation regarding the inner-city shadowing rate of ground-level debris occurrences was conducted in order to have insight into the prospects of the quantitative evaluation. For this a 3d city model was exploited to obtain shadow and layover masks. The viability of using simulated signatures in exchange for real SAR signature was verified in terms of a signature comparison in feature space showing good accordance between simulated and real samples.

Results of the debris detection algorithm were presented both for exemplary details and in form of a quantitative evaluation. The classification results demonstrate a good separation of vegetation and gravel from the texture of debris. Due to further undefined texture similarities and the closed world approach, though, the false positives rate is still high. 37% of all reference heaps of debris were identified. Taking into consideration that for the inner city of Christchurch an estimated 55% of debris occurrences is affected by shadowing, this value is rather high. Even though the classification step could not exclude all non-debris sources, the debris detection results provide the means to focus on a manageable number of detections and thus may provide helpful information for rescue efforts.

7.2. Outlook

The fact that sub-metre SAR images, also referred to as very high resolution (VHR) SAR images, can provide a much more detailed depiction of building damages than HR SAR images raises the question whether the proposed methodology can be successfully used on VHR SAR imagery. The additionally gained features and details on the signature of building damages could provide the necessary information for a classification into different damage classes (some indications are contained in [12]). Hence, the prospect of a simulation-based and damage type-specific training in the framework of a damage detection on post-event VHR SAR imagery is very intriguing.

The availability of a second post-event HR SAR image at short notice is not unlikely given missions such as TerraSAR-X, PAZ and COSMO-SkyMed. A combined use of two or more images under different aspect angles (e.g. taken on ascending and descending orbits) can considerably reduce the non-visible areas (shadowing) and the overlaid areas (layover) in inner cities. For areas visible in both images, a combination of the damage information may prove to enhance detection results.

Dual polarised or full polarimetric SAR imagery features another interesting prospect, since it potentially can produce additional vital information of debris and the scene altogether. It is expected that the damage detection task could benefit greatly from such an information gain.

Further, the structure of a city is bound to have an impact on the performance of the introduced damage detection algorithm. Old city structures, in particular, pose a different environment (see e.g. earthquake-ridden L'Aquila, Italy), with aspects such as the predominance of roofing type or the distance between buildings playing a role. The prospects for such structurally different environments are appealing.

Appendix A.

Classifier performance

Depending on the classification problem, factors such as the choice of classifier can have a large impact on the performance. To validate the use of a random forest for differentiating debris from similar textures, the following section addresses a performance comparison between the chosen random forest classifier and two alternative classifiers (SVM and CNN). For this analysis it was refrained from including gravel as a debris-like texture, since the presented results on the test scene (see Chapter 6) suggest vegetation to be the far more challenging factor.

In Section 6.1.4 a set of 2000 labelled TerraSAR-X samples of size 11 x 11 pixels (1000 for debris and 1000 for vegetation) was described, functioning as test data for the subsequent classification experiments. The training data consists of 1000 simulated samples, 500 for each class, which is considered sufficient for the training of the random forest and the SVM. However, since the training of a CNN requires significantly more data, the set was extended by additional simulations to a total of 14.000 samples for the training of this classifier exclusively. It was found that both SVM and CNN benefit strongly from an energy normalisation of the input samples. Hence, both training and test data were normalised as specified by

$$f_{norm} = \frac{f}{\sqrt{\sum f^2}}.$$ (A.1)

Since there is no observable benefit for the random forest classification, though, and also to provide a comparability to the described debris detection approach, the original input samples are used for the random forest classification. In the following, specifics on the implementation and the training process regarding the three classifiers are documented, whereas the fundamentals were described in Section 2.2.2.

Support Vector Machine In Section 5.2.4 the relevancy of a feature selection with respect to an SVM based classification was established and a reduced set of features was specified. The following performance assessment is based on this reduced feature set. It was mentioned in Section 2.2.2 that SVM algorithms are not scale invariant as are for example tree based algorithms. This leads to an unbalanced feature influence in cases that individual features do not have a similar range of values. For that reason it was decided to standardise the features before they are fed to the SVM, which implies a scaling to have zero- mean and unit-variance. Also, an energy normalisation of the feature vectors is conducted.

For the performance comparison a Radial Basis Function (RBF) kernel SVM is employed, which consists of a two-step SVM developed at Fraunhofer IOSB. Firstly, 2-class SVMs are used to discriminate all pairs of classes (a pre-classification) and secondly 1-class SVMs determine the class memberships based on the resulting new feature vector. It is a rather universal tool, where much of its power consists of the aptitude to handle more than two classes, which for the problem at hand is non-relevant. For a detailed description of the method see [58].
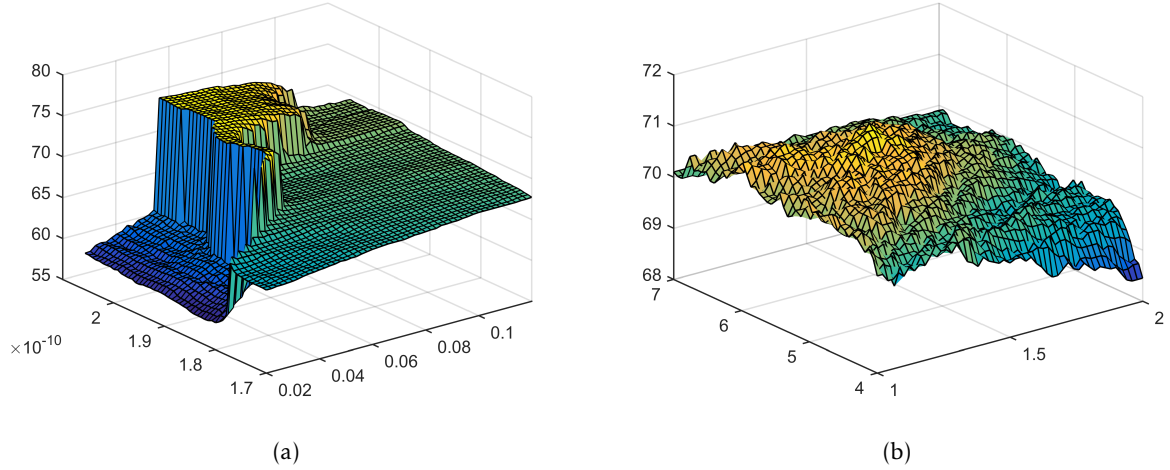
Figure A.1.: Grid search of the RBF kernel SVM a) using the defined feature set and b) using Fast Fourier Transform-based features.

The RBF kernel, which is defined as

$$k(x, y) = e^{-\frac{\|x-y\|^2}{\sigma^2}}, \tag{A.2}$$

where x and y denote sample data (support vectors) and σ is the standard deviation, maps the sample data to a high dimensional space. By maximising the minimal distance between the supporting vectors and the separating hyper plane the ideal kernel parameter σ is identified. The SVM mainly uses three hyper-parameters: the kernel parameter σ_2 of the 2-class SVMs, the kernel parameter σ_1 of the 1-class SVMs and a reject threshold. To identify the ideal values for the hyper-parameters σ_2 and σ_1 a grid search is conducted aiming to locate the global maximum. Figure A.1(a) visualises the grid search including the located maximum. For comparison, Figure A.1(b) demonstrates the grid search using Fast Fourier Transform-based features instead of the selected texture features. However, the maximal reached accuracy cannot compete.

CNN For many fields of application CNNs prove to be the most powerful tool available, and hence need to be considered for the task at hand. A notable difference to the described classification approach with random forest or SVM is the input data. Whereas random forest and SVM classification are based on the introduced set of extracted texture features, the CNN, as a feature extractor of its own, is fed with the image samples.

The nature of the problem under consideration suggests a rather shallow architecture model, thus focussing on models with no more than two convolution layers. Deeper structures were tested, however, the performance was bad, also due to the involved substantial overfitting of the model. Pooling can be a means to reduce overfitting. However, in this case an abundant use of pooling layers is not an option, since the 11 x 11 pixel sample size is very small to begin with and further sub-sampling would result in a significant loss of information.

```
 1   ''   Image Input             11x11x1 images with 'zerocenter' normalization
 2   ''   Convolution             10 3x3 convolutions with stride [1  1] and padding [1  1]
 3   ''   ReLU                    ReLU
 4   ''   Max Pooling             2x2 max pooling with stride [2  2] and padding [0  0]
 5   ''   Convolution             20 3x3 convolutions with stride [1  1] and padding [1  1]
 6   ''   ReLU                    ReLU
 7   ''   Fully Connected         15 fully connected layer
 8   ''   ReLU                    ReLU
 9   ''   Fully Connected         2 fully connected layer
10   ''   Softmax                 softmax
11   ''   Classification Output   cross-entropy
```
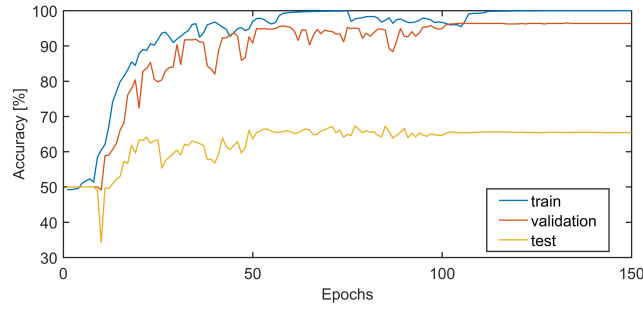
Figure A.2.: CNN architecture.

Figure A.3.: Training accuracies (mini-batch).

Other measures against overfitting include the use of dropout layers or simplifying the model. Both methods were explored, with the conclusion that a shallow structure without dropout layers leads to a good training and simultaneously prevents overfitting. The best results were achieved with the architecture defined in Figure A.2. Two 2-d convolutional layers are employed using 10/20 filters of size 3 x 3 and a stride (step size for roaming the input) of 1. Also included is a zero padding, which implies the padding of the borders to enforce a preservation of the input size. Further, one maxpooling layer with a 2 x 2 pooling region and a stride of 2 was installed. It operates by breaking down the input into rectangular sectors and returning each maximal value. The architecture concludes with two fully-connected layers and the application of a softmax-function to the output. Finally, the classification layer computes the cross entropy loss.

Regarding the process of training, 95% of the 14.000 simulated samples were employed as training data whereas the remaining 5% were used for validation purposes. An initial learning rate of 0.1 with a gradual decay every 25 epochs proved to be suitable. The training iterations were conducted using a number of 256 mini-batches and was continued until the mini-batch loss dropped to a value of 0.0001. The development of the mini-batch accuracies throughout the training can be observed in Figure A.3.

Random Forest For reasons of comparability, the proceedings and settings regarding the training of the random forest classifier correspond to those described in Chapter 5.

Results

Table A.1 shows the classification results attained by the three different classifiers, whereas corresponding performance measures are listed in Table A.2. For definitions of the performance measures see Section 2.2.2. Since the test classes are perfectly balanced, ACC is a valid measure in this case and hence can be used as evaluation criterion. The classification results show a good performance for both random forest and SVM, with 76.8% and 76.1% ACC respectively. Considering the limits of the selected set of texture features with regard to a separability of the two classes (perceptible in Figure 6.10) this is a satisfactory result. Since both classifiers were fed with a feature set that contains matching relevant features, the similar results seem conclusive.

The CNN approach achieved an ACC of 67.7%, which is rather poor in comparison. Considering the impressive performance of CNNs in other fields of application this result initially is quite unexpected. However, the power of a CNN stems from learning the entirety of a target, including its form and borders/surroundings.

Table A.1.: Confusion matrices regarding classification results of test data (D=Debris, V=Vegetation).

		Random Forest		SVM		CNN		
		D	V	D	V	D	V	$\sum$
Test	Debris	967	33	935	65	483	517	1000
	Vegetation	432	568	414	586	130	870	1000

Table A.2.: Classifier performance (debris=true).

Classifier	**ACC** [%]	TPR [%]	PPV [%]
Random Forest	**76.8**	96.7	69.1
SVM	**76.1**	93.5	69.3
CNN	**67.7**	48.3	78.8

Bearing this in mind, the action of limiting the input to 11 x 11 pixel samples containing exclusively debris texture, limits the CNNs feature extraction capacity severely. This is assumed to be the main reason for the rather poor results of the CNN approach. Note that this performance analysis is based on the pixel-wise classification, hence the resulting classification rates are rather conservative. It stands to reason that a component-wise (incidence-wise) classification would result in distinctly better classification rates. However, since the main aspect here is to establish a comparison to alternative classifiers, a pixel-wise classification was considered solid.

Appendix B.

Feature stability for phenological changes

Motivated by the question of stability concerning the introduced texture features, an analysis was conducted regarding a potential sensitivity towards phenological changes in the SAR signature of high vegetation [38, 47].

For this, two locations in Germany were investigated based on two HS TerraSAR-X amplitude image stacks, which combined cover a complete phenological year. The first image stack is located near Greding, Germany and consists of 16 HS TerraSAR-X images spread over half a year in late 2008 with an incidence angle of 48.5 degrees. The second image stack is near Stuttgart, Germany and contains 15 HS TerraSAR-X images acquired over a whole year in 2014 at an incidence angle of 22.7 degrees. Both locations were chosen as representatives for a Central European vegetation zone. As depicted in Figure B.1, six forest test areas were chosen in total, all representing homogeneous areas of deciduous forest. Furthermore, for both data sets, some auxiliary data, including optical images and weather data, were used for reference purposes only.

Prior to the analysis, the SAR images were subjected to several pre-processing steps, firstly a co-registration of the entire image stack. To ensure comparability to the damage detection algorithm, the remaining pre-processing and feature extraction steps were imitated. Merely the window size for feature extraction was changed to 21 x 21 pixels in order to have more stability and thus permit an interpretation of the changes.

Several of the features were found to be sensitive to phenological changes and reveal an observable trend over the year. Figure B.2 shows the seasonal development for three of these features promoting a distinct phenological trend. Note that, since the two employed data sets have quite different incidence angles, the backscattering coefficients are noticeably different. Hence, the results for the two data sets were plotted in separate figures with different scaling ranges if necessary. The four test areas in the Stuttgart data set as well as the two test areas in the Greding data set are in good agreement, showing very similar temporal behaviors. There was made a point of considering only test areas without noticeable slopes, since this has great impact on the backscattering intensities. Still, a minor offset between the plots of some of the test areas can be explained by a slight inclination of the test areas. When comparing the two data sets, the overlapping parts of the temporal runs confirm a mutual phenological change. Since the correlation amongst the texture features is rather high, a similar but less distinct trend can be observed for several of the remaining features. Further,
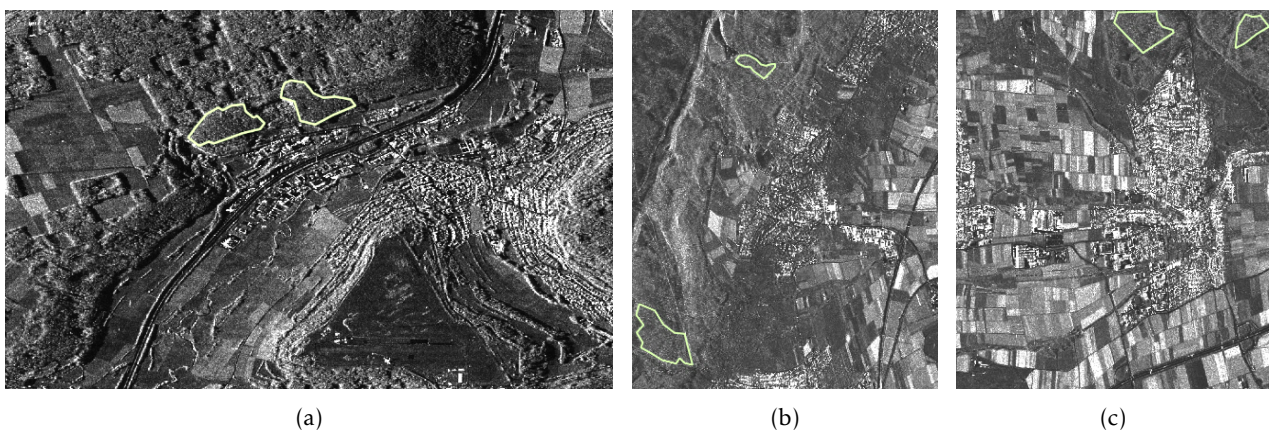

| (a) | (b) | (c) |

Figure B.1.: Six forest test areas in TerraSAR-X images of a) Greding, Germany and b), c) Stuttgart, Germany.
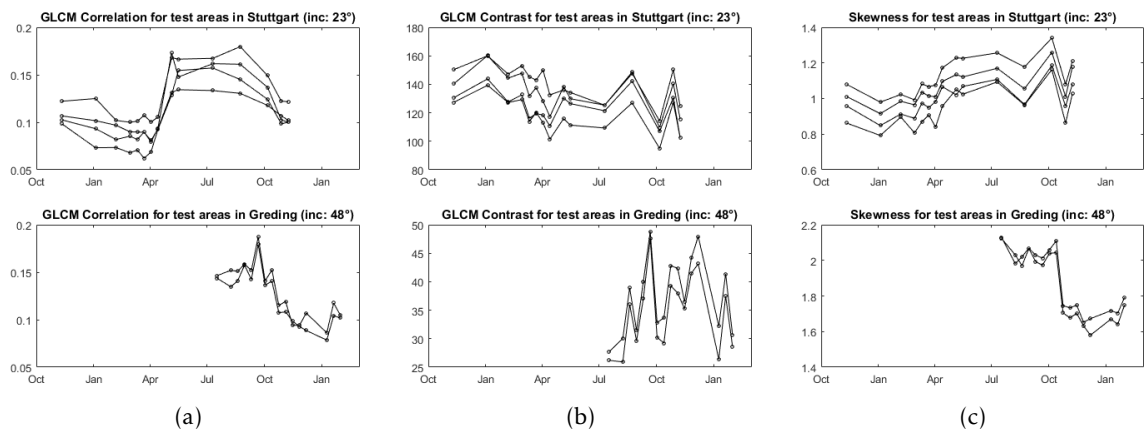
Figure B.2.: Phenological trend of three exemplary texture features (see Section 2.2.1) throughout a seasonal year a) f_3, b) f_2 and c) γ (upper row: the four test areas located near Stuttgart, lower row: the two test areas located near Greding).

there are features showing minimal to no seasonal variation. Regarding the use of these texture features for the separation of debris from vegetation, these findings are of immediate concern. It remains to be seen how much of an impact these phenological trends have on the detection performance.

Nomenclature

ACC .... Accuracy
AoI .... Area of Interest
ASI .... Italian Space Agency
ASM .... Angular Second Moment
BRDF .... Bidirectional Reflectance Distribution Function
CNN .... Convolutional Neural Network
CohRaS ...... Coherent Raytracing Simulator
CSA .... Canadian Space Agency
DLR .... Deutsches Zentrum für Luft- und Raumfahrt
DTM .... Digital Terrain Model
EM .... Electromagnetic
ESA .... European Space Agency
FM .... Frequency Modulation
GLCM .... Gray-Level Co-occurrence Matrix
GO .... Geometrical Optics
HR .... High Resolution
HS .... High resolution Spotlight
IDM .... Inverse Difference Moment
IR .... Infrared
JAXA .... Japanese Aerospace EXploration Agency
LBP .... Local Binary Pattern
LoD .... Level of Detail
LTE .... Laws Texture Energy
NESZ .... Noise Equivalent Sigma Zero
OOB .... Out-Of-Bag
PDF .... Probability Density Function
PO .... Physical Optics
PPV .... Positive Predictive Value
PTD .... Physical Theory of Diffraction
RADAR ...... Radiofrequency Detection and Ranging
RBF .... Radial Basis Function
RCM .... Range Cell Migration
RCS .... Radar Cross Section
ReLU .... Rectified Linear Unit
SAR .... Synthetic Aperture Radar
SBR .... Shooting and Bouncing Rays
SLC .... Single Look Complex
SNR .... Signal-to-Noise Ratio
SVM .... Support Vector Machine
TPR .... True Positive Rate
UAV .... Unmanned Aerial Vehicle
VHR .... Very High Resolution

Bibliography

[1] Airbus Defence & Space. Radiometric calibration of TerraSAR-X data to beta nought and sigma nought. https://www.intelligence-airbusds.com/files/standard/public/p9315_6a5ebe517eed66bee4d cdca7fc59df4dradiometric-calibration-of-terrasar-x-data.pdf, last visited: 2020-03-15, 2014.

[2] Amanatides, J., and Woo, A. A fast voxel traversal algorithm for ray tracing. *Proceedings of EUROGRAPHICS 87* (1987), 3–10.

[3] Anglberger, H., Suess, H., and Hager, M. Application of SAR simulation for signature analysis and identification of complex targets on TerraSAR-X data. *TerraSAR-X Science Team Meeting* (2011).

[4] Arciniegas, G., Bijker, W., Kerle, N., and Tolpekin, V. Coherence- and amplitude-based analysis of seismogenic damage in Bam, Iran, using ENVISAT ASAR data. *IEEE Transactions on Geoscience and Remote Sensing 45* (2007), 1571–1581.

[5] Auer, S. *3D synthetic aperture radar simulation for interpreting complex urban reflection scenarios*. PhD thesis, Technical University of Munich (TUM), 2011.

[6] Balz, T., and Liao, M. Building damage detection using post-seismic high-resolution SAR satellite data. *International Journal of Remote Sensing 31* (2010), 3369–3391.

[7] Balz, T., and Stilla, U. Hybrid GPU based single- and double-bounce SAR simulation. *IEEE Transactions on Geoscience and Remote Sensing 47* (2009), 3519–3529.

[8] Breiman, L. Random forests. *Journal Machine Learning 45*, 1 (2001), 5–32.

[9] Brett, P., and Guida, R. Earthquake damage detection in urban areas using curvilinear features. *IEEE Transactions on Geoscience and Remote Sensing 51* (2013), 4877–4884.

[10] Brown, C., Milke, M., and Seville, E. Disaster waste management: A review article. *Waste Management 31*, 6 (2011), 1085–1098.

[11] Brunner, D., Lemoine, G., and Bruzzone, L. Earthquake damage assessment of buildings using VHR optical and SAR imagery. *IEEE Transactions on Geoscience and Remote Sensing 48* (2010), 2403–2420.

[12] Brunner, D., Schulz, K., and Brehm, T. Building damage assessment in decimeter resolution SAR imagery: A future perspective. *Joint Urban Remote Sensing Event* (2011), 217–220.

[13] Brzev, S., Greene, M., Arnold, C., Blondet, M., Cherr, S., Comartin, C., D'Ayala, D., Farsi, M., Jain, S., Naeim, F., Pantelic, J., Samant, L., and Sassu, M. The web-based world housing encyclopedia: Housing construction in high seismic risk areas of the world. *13th World Conference on Earthquake Engineering (WCEE)* (2004), 1–14.

[14] Chini, M., Anniballe, R., Bignami, C., Pierdicca, N., Mori, S., and Stramondo, S. Identification of building double-bounces feature in very high resolution SAR data for earthquake damage mapping. *International Geoscience and Remote Sensing Symposium (IGARSS)* (2015), 1144–1147.

[15] Chini, M., Bignami, C., Stramondo, S., and Pierdicca, N. Uplift and subsidence due to the 26 december 2004 Indonesian earthquake detected by SAR data. *International Journal of Remote Sensing 29* (2008), 3891–3910.

[16] Clausi, D. A., and Jernigan, M. E. A fast method to determine co-occurrence texture features. *IEEE Transactions on Geoscience and Remote Sensing 36*, 1 (1998), 298–300.

[17] Cubrinovski, M., Winkley, A., Haskell, J., Palermo, A., Wotherspoon, L., Robinson, K., Bradley, B., Brabhaharan, P., and Hughes, M. Spreading-induced damage to short-span bridges in Christchurch, New Zealand. *Earthquake Spectra 30*, 1 (2014), 57–83.

[18] Cumming, I. G., and Wong, F. H. *Digital Processing of Synthetic Aperture Radar Data: Algorithms and Implementation*. Artech House, Boston, U.S.A., 2005.

[19] Dell'Acqua, F., and Polli, D. Post-event only VHR radar satellite data for automated damage assessment. *Photogrammetric Engineering & Remote Sensing 77* (2011), 1037–1043.

[20] Dong, L., and Shan, J. A comprehensive review of earthquake-induced building damage detection with remote sensing techniques. *ISPRS Journal of Photogrammetry and Remote Sensing 84* (2013), 85–99.

[21] Duda, R. O., Hart, P. E., and Stork, D. G. *Pattern Classification*, 2nd ed. John Wiley and Sons, New York, U.S.A., 2001.

[22] Eineder, M., and Fritz, T. TerraSAR-X ground segment, basic product specification document (TX-GS-DD-3302), Release 1.9, October 14, 2013.

[23] Gamba, P., Dell'Acqua, F., and Odasso, L. Object-oriented building damage analysis in VHR optical satellite images of the 2004 Tsunami over Kalutara, Sri Lanka. *Urban Remote Sensing Joint Event* (2007), 1–5.

[24] Gerke, M., and Kerle, N. Automatic structural seismic damage assessment with airborne oblique pictometry© imagery. *Photogrammetric Engineering and Remote Sensing 77* (2011), 885–898.

[25] Gong, L., Wang, C., Wu, F., Zhang, J., Zhang, H., and Li, Q. Earthquake-induced building damage detection with post-event sub-meter VHR TerraSAR-X staring spotlight imagery. *Remote Sensing 8*, 11 (2016), 887.

[26] Gröger, G., and Plümer, L. CityGML - interoperable semantic 3D city models. *ISPRS Journal of Photogrammetry and Remote Sensing 71* (2012), 12–33.

[27] Grünthal, G. European macroseismic scale 1998 (EMS-98). *Cahiers du Centre Européen de Géodynamique et de Séismologie 15* (1998).

[28] Guida, R., Iodice, A., and Riccio, D. Monitoring of collapsed built-up areas with high resolution SAR images. *International Geoscience and Remote Sensing Symposium (IGARSS)* (2010), 2422–2425.

[29] Hammer, H., Kuny, S., and Schulz, K. Preparing a new data set for earthquake damage detection in SAR imagery: the Christchurch example II. *Proceedings of SPIE, SAR Image Analysis, Modeling, and Techniques XIV 9243* (2014), 34–41.

[30] Hammer, H., and Schulz, K. Coherent simulation of SAR images. *Proceedings of SPIE, Image and Signal Processing for Remote Sensing XV 7477* (2009), 406–414.

[31] Hammer, H., and Schulz, K. Dedicated SAR simulation tools for ATR and scene analysis. *Proceedings of SPIE, SAR Image Analysis, Modeling, and Techniques XI 8179* (2011), 188–196.

[32] Haralick, R. M., Shanmugam, K., and Dinstein, I. Textural features for image classification. *IEEE Transactions on Systems, Man, and Cybernetics 3*, 6 (1973), 610–621.

[33] Hastie, T., Tibshirani, R., and Friedman, J. *The Elements of Statistical Learning: data mining, inference, and prediction*, 2nd ed. Springer Series in Statistics, New York, U.S.A., 2009.

[34] Henderson, F. M., and Lewis, A. J. *Principles and Applications of Imaging Radar. Manual of Remote Sensing*, 3rd ed., vol. 2. John Wiley and Sons, New York, U.S.A., 1998.

[35] Ho, T. K. The random subspace method for constructing decision forests. *IEEE Transactions on Pattern Analysis and Machine Intelligence 20*, 8 (1998), 832–844.

[36] Hoffmann, J. Mapping damage during the Bam (Iran) earthquake using interferometric coherence. *International Journal of Remote Sensing 28* (2007), 1199–1216.

[37] Hong, H., Pan, S., and Zheng, L. A fast calculation method for gray-level co-occurrence matrix base on GPU. *2nd International Conference on Image, Vision and Computing (ICIVC) 36*, 1 (2017), 1063–1067.

[38] Ihrig, R., Kuny, S., Thiele, A., and Hinz, S. Analysis of phenological changes of high vegetation in amplitude images of SAR time series. *Proceedings of SPIE, Earth Resources and Environmental Remote Sensing/GIS Applications VIII 10428* (2017).

[39] JEU. Joint environmental unit disaster waste management guidelines - final draft ed. https://www.humanitarianlibrary.org/sites/default/files/2014/02/JEUDWMPFinalDraftfordistribution.pdf, last visited: 2020-03-15, 2010.

[40] Klausing, H., and Holpp, W. *Radar mit realer und synthetischer Apertur: Konzeption und Realisierung*. Oldenbourg Verlag, München, Germany, 2000.

[41] Koch, B. Status and future of laser scanning, synthetic aperture radar and hyperspectral remote sensing data for forest biomass assessment. *ISPRS Journal of Photogrammetry and Remote Sensing 65*, 6 (2010), 581–590.

[42] Koyama, C., Gokon, H., Jimbo, M., Koshimura, S., and Sato, M. Disaster debris estimation using high-resolution polarimetric stereo-SAR. *ISPRS Journal of Photogrammetry and Remote Sensing 120* (2016), 84–98.

[43] Kuny, S., Hammer, H., and Schulz, K. Preparing a new data set for earthquake damage detection in SAR imagery: the Christchurch example I. *Proceedings of SPIE - SAR Image Analysis, Modeling, and Techniques XIV 9243* (2014), 255–262.

[44] Kuny, S., Hammer, H., and Schulz, K. Discriminating between the SAR signatures of debris and high vegetation. *International Geoscience and Remote Sensing Symposium (IGARSS)* (2015), 473–476.

[45] Kuny, S., Hammer, H., and Schulz, K. Assessing the suitability of simulated SAR signatures of debris for the usage in damage detection. *ISPRS - International Archives of the Photogrammetry, Remote Sensing and Spatial Information Sciences* (2016), 877–881.

[46] Kuny, S., Hammer, H., Schulz, K., and Hinz, S. Towards a reliable detection of debris in high resolution SAR images of urban areas. *11th European Conference on Synthetic Aperture Radar, EUSAR* (2016), 1015–1018.

[47] Kuny, S., Ihrig, R., Boldt, M., and Thiele, A. Study on phenological changes in TerraSAR-X time series. *12th European Conference on Synthetic Aperture Radar, EUSAR* (2018), 55–58.

[48] Kuny, S., and Schulz, K. Debris detection in SAR imagery using statistics of simulated texture. *8th IAPR Workshop on Pattern Recognition in Remote Sensing, PRRS* (2014), 1–4.

[49] Kuny, S., Schulz, K., and Hammer, H. Signature analysis of destroyed buildings in simulated high resolution SAR data. *International Geoscience and Remote Sensing Symposium (IGARSS)* (2013), 903–906.

[50] Kuny, S., Schulz, K., and Hammer, H. Simulation based texture analysis of heaps of debris for damage assessment in high resolution SAR data. *Proceedings of 6th International Conference on Recent Advances in Space Technologies (RAST)* (2013), 1169–1172.

[51] Land Information New Zealand. Earth's data platform. https://data.linz.govt.nz/layer/51937-christchurch-post-earthquake-01m-urban-aerial-photos-index-tiles-24-february-2011/, last visited: 2020-03-15.

[52] Laws, K. I. Rapid texture identification. *Proceedings of SPIE, Image Processing for Missile Guidance 238* (1980), 376–380.

[53] Mäkynen, M., and Karvonen, J. Incidence angle dependence of first-year sea ice backscattering coefficient in Sentinel-1 SAR imagery over the Kara Sea. *IEEE Transactions on Geoscience and Remote Sensing 55*, 11 (2017), 6170–6181.

[54] Marin, C., Bovolo, F., and Bruzzone, L. Building change detection in multitemporal very high resolution SAR images. *IEEE Transactions on Geoscience and Remote Sensing 53* (2015), 2664–2682.

[55] Matsuoka, M., and Yamazaki, F. Use of satellite SAR intensity imagery for detecting building areas damaged due to earthquakes. *Earthquake Spectra 20* (2004).

[56] Meyer, F. J., Ajadi, O. A., and Hoppe, E. Network-scale pavement roughness mapping using spaceborne high-resolution X-band SAR data. *IEEE International Geoscience and Remote Sensing Symposium (IGARSS)* (2017), 1558–1561.

[57] Meyer-Hilberg, J. PIRDIS: a new versatile tool for SAR/MTI systems simulation. *6th European Conference on Synthetic Aperture Radar, EUSAR* (2006).

[58] Middelmann, W., Ebert, A., and Thönnessen, U. Assessment of a novel decision and reject method for multi-class problems in a target classification framework for SAR scenarios. *Proceedings of SPIE, Algorithms for Synthetic Aperture Radar Imagery XIII 6237* (2006), 200–208.

[59] Milisavljevic, N., Closson, D., Holecz, F., Collivignarelli, F., and Pasquali, P. An approach for detecting changes related to natural disasters using synthetic aperture radar data. *ISPRS - International Archives of the Photogrammetry, Remote Sensing and Spatial Information Sciences XL-7/W3* (2015), 819–826.

[60] Miura, H., Midorikawa, S., and Matsuoka, M. Building damage assessment using high-resolution satellite SAR images of the 2010 Haiti earthquake. *Earthquake Spectra 32* (2016), 591–610.

[61] Moya Huallpa, L., Yamazaki, F., Liu, W., and Yamada, M. Detection of collapsed buildings from lidar data due to the 2016 kumamoto earthquake in japan. *Natural Hazards and Earth System Sciences 18* (2018), 65–78.

[62] Ojala, T., Pietikäinen, M., and Harwood, D. A comparative study of texture measures with classification based on feature distributions. *Pattern Recognition 29* (1996), 51–59.

[63] Okada, S., and Takai, N. Classifications of structural types and damage patterns of buildings for earthquake field investigation. *Journal of Structural and Construction Engineering, AIJ 524* (2000), 65–72.

[64] Peng, H., Long, F., and Ding, C. Feature selection based on mutual information: criteria of max-dependency, max-relevance, and min-redundancy. *IEEE Transactions on Pattern Analysis and Machine Intelligence 27*, 8 (2005), 1226–1238.

[65] Phong, B. T. Illumination for computer generated pictures. *Communications of the ACM 18*, 6 (1975), 311–317.

[66] Polli, D., Dell'Acqua, F., Gamba, P., and Lisini, G. Earthquake damage assessment from post-event only radar satellite data. *8th International Workshop of Remote Sensing for Disaster Response* (2020).

[67] Powers, D. M. Evaluation: From precision, recall and f-measure to roc., informedness, markedness and correlation. *Machine Learning Technologies 2*, 1 (2011), 37–63.

[68] Rathje, E., Woo, K.-S., Crawford, M., and Neuenschwander, A. Earthquake damage identification using multi-temporal high-resolution optical satellite imagery. *Proceedings of IEEE International Geoscience and Remote Sensing Symposium (IGARSS)* (2005), 5045–5048.

[69] Rehor, M. Classification of building damages based on laser scanning data. *The Photogrammetric Journal of Finland 20*, 2 (2007), 54–63.

[70] Saha, S., Bovolo, F., and Bruzzone, L. Destroyed-buildings detection from VHR SAR images using deep features. *Proceedings of SPIE, Image and Signal Processing for Remote Sensing XXIV 10789* (2018).

[71] Sammon, J. W. A nonlinear mapping for data structure analysis. *IEEE Transactions on Computers 18*, 5 (1969), 401–409.

[72] Schmitt, A. *Änderungserkennung in multitemporalen und multipolarisierten Radaraufnahmen*. PhD thesis, Karlsruhe Institute of Technology (KIT), 2012.

[73] Schweier, C., and Markus, M. Assessment of the search and rescue demand for individual buildings. *Proceedings of the 13th World Conference on Earthquake Engineering* (2004).

[74] Sonka, M., Hlavac, V., and Boyle, R. *Image Processing, Analysis, and Machine Vision*, 3rd ed. Thomson Engineering, Toronto, Canada, 2008.

[75] Tao, J., and Auer, S. Simulation-based building change detection from multiangle SAR images and digital surface models. *IEEE Journal of Selected Topics in Applied Earth Observations and Remote Sensing 9* (2016), 3777–3791.

[76] Tao, J., Auer, S., and Reinartz, P. Detecting changes between a DSM and a high resolution SAR image with the support of simulation based separation of urban scenes. *9th European Conference on Synthetic Aperture Radar, EUSAR* (2012), 95–98.

[77] Tomowski, D., Klonus, S., Ehlers, M., Michel, U., and Reinartz, P. Change visualization through a texture-based analysis approach for disaster applications. *ISPRS - International Archives of the Photogrammetry, Remote Sensing and Spatial Information Sciences 38* (2010), 263–268.

[78] Tonkin & Taylor, Earthquake Commission (EQC). Canterbury earthquakes 2010 and 2011: Land report as at 29 February 2012. https://www.eqc.govt.nz/canterbury-earthquakes/land-claims/land-reports/stage-3-land-report, last visited: 2020-03-15, 2013.

[79] Ulaby, F. T., Moore, R. K., and Fung, A. K. *Microwave Remote Sensing, Active and Passive, Volume 1: Microwave Remote Sensing Fundamentals and Radiometry.* Addison-Wesley Publishing Company, Reading, U.S.A., 1981.

[80] Ulaby, F. T., Moore, R. K., and Fung, A. K. *Microwave Remote Sensing, Active and Passive, Volume 2: Radar Remote Sensing and Surface Scattering and Emission Theory.* Addison-Wesley Publishing Company, Reading, U.S.A., 1982.

[81] Uprety, P., Yamazaki, F., and Dell'Acqua, F. Damage detection using high-resolution SAR imagery in the 2009 L'Aquila, Italy, earthquake. *Earthquake Spectra 29* (2013), 1521–1535.

[82] Vapnik, V. N. *Statistical Learning Theory.* John Wiley and Sons, New York, U.S.A., 1998.

[83] Wagner, W., Lemoine, G., and Borgeaud, M. A study of vegetation cover effects on ERS scatterometer data. *IEEE Transactions on Geoscience and Remote Sensing 37*, 2 (1999), 938–948.

[84] Wang, T., and Jin, Y.-Q. Postearthquake building damage assessment using multi-mutual information from pre-event optical image and postevent SAR image. *IEEE Geoscience and Remote Sensing Letters 9* (2012), 452–456.

[85] Welte, A., Hammer, H., Thiele, A., and Hinz, S. Simulation of TanDEM-X interferograms for urban change detection. *Proceedings of SPIE, Earth Resources and Environmental Remote Sensing/GIS Applications VIII 10428* (2017), 22–32.

[86] Yamazaki, F., Vu, T. T., and Matsuoka, M. Context-based detection of post-disaster damaged buildings in urban areas from satellite images. *Urban Remote Sensing Joint Event* (2007), 1–5.

[87] Yonezawa, C., Tomiyama, N., and Takeuchi, S. Urban damage detection using decorrelation of SAR interferometric data. *IEEE International Geoscience and Remote Sensing Symposium (IGARSS) 4* (2002), 2051–2053.

Danksagung

Ein Rückblick auf die aufregende Entstehungszeit meiner Promotionsarbeit lässt mich insbesondere festhalten: Es sind nicht wenige, die über die letzten Jahre auf verschiedenste Weise zum Gelingen der Arbeit beigetragen haben und die einen besonderen Dank verdienen.

Zuallererst möchte ich mich herzlich bei meinem Doktorvater Prof. Stefan Hinz bedanken, der mir das Promotionsvorhaben ermöglicht und mich fachlich kompetent auf meinem Weg betreut hat. Des Weiteren bedanke ich mich bei meinem Zweitgutachter Prof. Peter Reinartz für sein Mitwirken in der Endphase.

Mein besonderer Dank gilt Horst Hammer, der mein Vorhaben mit konstruktiven fachlichen Diskussionen und (nicht minder wichtig) beständiger Motivationsarbeit begleitet hat; und Antje Thiele, deren organisatorische Unterstützung maßgeblich zum Umsetzen meines Vorhabens beigetragen hat. Dank gebührt auch meinem Abteilungsleiter Karsten Schulz für den wissenschaftlichen (und auch den zeitlichen) Freiraum, den er mir ermöglicht hat, sowie meinen wunderbaren Kollegen für ihre Hilfsbereitschaft in den unterschiedlichsten Lagen.

Zum Schluss möchte ich mich bei meinem Freundes- und Familienkreis bedanken, ohne deren mentale Unterstützung mir ein solches Vorhaben nicht möglich gewesen wäre.